New search for the Neutron Electric Dipole Moment using Ultracold Neutrons at the Spallation Neutron Source

Thesis by

Riccardo Schmid

In Partial Fulfillment of the Requirements

for the Degree of

Doctor of Philosophy

California Institute of Technology

Pasadena, California

2014

(Defended October 24, 2013)

alla mia nonna Luciana

Acknowledgements

I am grateful for the support that I have received from a number of people during my long academic career at Caltech. Firstly, I would like to thank my research adviser, Dr. Bradley Filippone, for giving me the opportunity to work in his research group and experience the ultracool Physics of ultracold neutrons. I admire Brad's extensive knowledge and appreciate him sharing it with me through insightful conversations over the years.

I owe thanks to the post-docs and personnel in Kellogg Radiation Laboratory for their support and disponibility during my many years of research. I would like to especially thank Dr. Brad Plaster for helping me get started during the first couple of years of my graduate studies.

Many thanks go to Dr. Takeyasu Ito who supervised me during my visits to Los Alamos National Laboratory. I enjoyed the conversations, ranging from superfluid Helium to hot espresso, as well as the company during my time there. I have learned a lot from my visits to LANL, thanks to Takeyasu and the other fine people working at the laboratory.

I would like to acknowledge Dr. Jim Eisenstein and Dr. Lisa Tracy for the use of their laboratory and their assistance in low temperature resistivity measurements. I would like to thank Dr. George Seidel for his time and insight on the difficult topic of electrical breakdown during my visit to Brown University.

During my graduate career I met many graduate students whose friendships I cherish and will remember for years to come. My graduate Physics classmates, "il gruppo di Italiani", the Caltech bowlers and surfers, to name a few, have had a great impact on my life.

Finally, I would like to thank the people closest to me, even from far away, for their constant support of my education. My parents Walter and Chiara without whom I would not be here. My sister Silvia, for keeping it lively. My grandmother Luciana for believing I could do this. Last, but not least, I would like to thank my girlfriend Zaynah for always being there for me.

Abstract

This document introduces the planned new search for the neutron Electric Dipole Moment at the Spallation Neutron Source at the Oak Ridge National Laboratory. A spin precession measurement is to be carried out using Ultracold neutrons diluted in a superfluid Helium bath at $T \simeq 0.5$ K, where spin polarized ^{3}He atoms act as detectors of the neutron spin polarization. The planned sensitivity of the new measurement is $d_{\mathrm{n}} \approx 5 \times 10^{-28}\,\mathrm{e\dot{c}m}$. This manuscript describes some of the key aspects of the planned experiment with the contributions from Caltech to the development of the project.

Techniques used in the design of magnet coils for Nuclear Magnetic Resonance were adapted to the geometry of the experiment. Described is an initial design approach using a pair of coils tuned to shield outer conductive elements from resistive heat loads, while inducing an oscillating field in the measurement volume. A small prototype was constructed to test the model of the field at room temperature.

A large scale test of the high voltage system was carried out in a collaborative effort at the Los Alamos National Laboratory. The application and amplification of high voltage to polished steel electrodes immersed in a superfluid Helium bath was studied, as well as the electrical breakdown properties of the electrodes at low temperatures.

A suite of Monte Carlo simulation software tools to model the interaction of neutrons, ^{3}He atoms, and their spins with the experimental magnetic and electric fields was developed and implemented to further the study of expected systematic effects of the measurement, with particular focus on the false Electric Dipole Moment induced by a Geometric Phase akin to Berry's phase.

An analysis framework was developed and implemented using unbinned likelihood to fit the time modulated signal expected from the measurement data. A collaborative Monte Carlo data set was used to test the analysis methods.

Contents

Chapter 1

Introduction

The search for Electric Dipole Moments of elementary particles has been of special interest since the experimental evidence that fundamental discrete symmetries are not conserved in weak interactions. The symmetries of *Parity inversion* (P), *Charge conjugation* (C) and *Time reversal* (T) have all been put into question theoretically, and experimental evidence of breaking of the individual symmetries of P and C, as well as combined (i.e. CP) is apparent. On the other hand, the combined symmetry of CPT is still considered an unbroken symmetry.

Purcell and Ramsey first proposed [1] in 1950 that experimental evidence augmenting the already available observation was needed to exclude particle EDMs. They set out to measure the EDM of the neutron [2] as the only viable neutral particle for which an experiment could be easily constructed.

1.1 Parity violation

The experimental evidence leading to the discovery that Parity is not conserved in the weak interaction came from the experimental observation of the decay of the $K^{\pm}$ into two final states of different parities [3,4]. Lee and Yang in 1956 [5] first proposed that the effect could be explained by lack of Parity as a fundamental symmetry. Before this result, little thought was given to the possibility that a discrete symmetry such as Parity would be violated in any of the physical interactions. The confirmation of the violation was observed in the decay of polarized ^{60}Co by Wu in 1957 [6]. In this experiment, a preferred direction of β decay of the nucleus was observed to coincide with the direction of spin polarization of the nucleus. This is shown to violate Parity conservation by noticing that under reversal of

space coordinates, the decay direction preference would be inverted, while the axial vector representing the spin would not, resulting in a different system which is not observed.

The violation of P symmetry is included in the weak sector of the Standard Model by restricting the interaction only to left handed particles. On the other hand, only right handed anti-particles participate in the weak interaction, resulting in different behavior and a violation of C invariance. These violations of symmetry result in the conservation of the combined CP invariance.

The presence of a permanent EDM $\boldsymbol{d}$ of an elementary particle would also be in violation of invariance under a Parity transformation. The EDM would need to be aligned with the orientation of the particle spin $\boldsymbol{\sigma}$, since that is the only quantum number that describes the particle internal state. Under an inversion of coordinates, the axial vector representing the spin orientation $\boldsymbol{\sigma}$ of the particle would be invariant, while the charge distribution would appear inverted, resulting in a different alignment of $\boldsymbol{d}$ with respect to $\boldsymbol{\sigma}$. The normal and inverted system would have different energy levels when exposed to the same electric and magnetic field configurations, resulting in a violation of the mirror symmetry.

1.2 Time reversal violation

Of great interest is the violation of Time reversal T symmetry that a permanent EDM would imply. Landau [7] noted that a permanent EDM would not be invariant under a T reversal. In this case, a spatial charge distribution would be left unchanged, while a rotation would change direction resulting in the reversal of the spin vector. Time symmetry violation has not been directly observed in stable systems, but evidence of this violation has been seen as a consequence of the CP violation observed in the decay of the neutral Kaon system [8, 9]. In addition, there has been an explicit observation of time reversal violation in the B meson system at $BaBaR$ [10]. The violation of CP symmetry is included in the Standard Model as a complex phase in the Cabibbo-Kobayashi-Maskawa (CKM) quark flavor mixing matrix [11].

1.3 Baryon asymmetry motivation

The symmetry violation that would be expected from the existence of a permanent EDM would help explain some of the features of the observed Universe, and in particular, the baryon asymmetry that must have ensued during its early stages. In fact, the lack of observational evidence of anti-matter galaxies far away from our own has suggested that there must be a local asymmetry in the physical processes, that during baryogenesis [12], led to the quasi-stable state of matter today. The concept of baryogenesis assumes that the processes by which the baryons came to exist must be the same as particle interactions today. Since the baryon number is conserved in the processes that involve baryons in the Standard Model, the processes that can create baryons must create an equal amount of anti-baryons. Annihilation does not change the baryon number, but reduces the total quantity of massive particles. The presence of baryons and anti-baryons in equal numbers during the initial formation would lead to the annihilation of all possible matter until the number density would vanish. For this reason it would be expected to observe anti-matter in equal quantities from astronomical data if, for instance, matter and anti-matter clusters separated early on and survived annihilation. An extensive study of the abundance of matter in the universe and the consequences on the symmetrical assumptions of the solutions to the physical laws is done by [13].

In 1967 Sakharov [14] proposed that baryon asymmetry could be explained if interactions in the Standard Model include some asymmetry that favors matter over anti-matter. Sakharov concluded that a basic set of conditions would be necessary for this to happen, known as the Sakharov conditions. Firstly, the baryon number must not be conserved. In addition, there must be some preference for processes that result in abundance of, what is considered, matter. Lastly, there must have been an initial environment with a significant deviation from thermal equilibrium. The EDMs are interesting for the second condition, which implies that the violation of CP invariance can be used to justify the preference of processes that leave an excess of matter over anti-matter. As of right now the amount of CP violation in the Standard Model is limited by the few known violating weak decays [15]. So far, the amount of CP violation included in the Standard Model is not enough to be responsible for baryogenesis [16–18], so the possibility of new sources of CP violations would validate this idea. Theories that go beyond the Standard Model can attribute CP violating

processes to interactions with Super-Symmetric particles [19] and permanent EDMs offer a sensitive sensitive probe of new sources of CP violation [20, 21].

1.4 Electric Dipole Moments

The search for electric dipole moments has been carried out on several elementary particles and atoms. Free electrons and other charged particles can be studied, but because of their charge, the Lorentz force makes it hard to distinguish effects that can be attributed to an EDM. Atomic electrons have been studied, using for example the Cesium atom [22] and Thallium atom [23, 24]. In these measurements, an atomic permanent EDM would be dominated by contribution of the unpaired electron EDM d_e. Heavy molecules that have an unpaired electron can also be used to study the EDM due an unpaired electron. The best limit on the electron EDM is given by the study of the molecule YbF [25, 26]

$$|d_e| < 10.5 \times 10^{-28}\,\mathrm{e}\cdot\mathrm{cm} \qquad 90\%\,\mathrm{C.L.}\,. \tag{1.1}$$

It is important to note that only permanent EDMs that violate the dicrete symmetries are of interest. For instance, there are molecules that have large electric dipoles that are easily measurable, such as H_2O, or NH_3. These dipoles do not represent a violation of discrete symmetries because, in general, the composite structure of the molecules allows degeneracy, so that both normal and P inverted molecules are found in Nature, and the violation is lifted.

Nuclear EDMs can be studied in neutral atoms but their effect will be reduced [27] by the interaction of the electron cloud with the E field, partially shielding the field at the nucleus. The best limits for nuclear EDM are offered by measurement of massive atoms, such as ^{199}Hg [28], with a limit

$$\left|d(^{199}\mathrm{Hg})\right| < 3.1 \times 10^{-29}\,\mathrm{e}\cdot\mathrm{cm} \qquad 95\%\,\mathrm{C.L.}\,. \tag{1.2}$$

This limit can be used to estimate the EDM of the neutron, and it results in a similar sensitivity as the current best direct measurement of the neutron EDM [28].

The neutron EDM has also been experimentally sought. The only quantum number describing the neutron is its spin and no degenerate states exist, so only a permanent EDM

can be measured, aligned or anti-aligned with the neutron's spin. The neutron seems to offer the best qualities for a measurement due to its neutrality, but because the neutron is not a stable particle, it is hard to collect a large statistical sample for long periods of time. At first, neutron beams were used [2] which can only interact with the E field for a short period of time. The introduction of ultracold neutrons [29,30] which can be trapped, has shifted the search to longer measurement times, but with a significant loss of statistical availability. In addition, the higher sensitivity of the experimental apparatus has opened the door to systematic effects that confuse the measurement of an EDM (e.g. [31]).

The current best limit for the neutron EDM is offered by the ILL measurement using ultracold neutrons [32,33] which sets a limit of

$$|d_n| < 2.9 \times 10^{-26}\,\mathrm{e\,cm} \qquad 90\%\,\mathrm{C.L.}\,. \tag{1.3}$$

This is about 6-7 orders of magnitude improvement in sensitivity with respect to the first experimental results of the 1950's [1,2].

The proposed *nEDM* measurement [34] is discussed in this work. The new measurement should offer a significantly higher sensitivity to the neutron EDM than the previous experiments.

Chapter 2

nEDM experiment at SNS

A new technique to search for the neutron Electric Dipole Moment using ultracold neutrons has been discussed by Golub and Lamoreaux [34] which uses ^{3}He as a co-magnetometer. A collaborative effort is underway to implement the experimental technique in the *nEDM* measurement using the Spallation Neutron Source (SNS) at the Oak Ridge National Laboratory (ORNL) [35]. The experiment aims to measure a shift in Larmor precession frequency of the neutron under the influence of a large electric field. The planned sensitivity of the new measurement is expected to be ~ 100 better than the existing limit.

2.1 Ultracold neutrons

If the neutron energy is sufficiently low, its De Broglie wavelength becomes larger than the spacing of atoms in matter, so that interactions with a material can result in coherent scattering where all the nuclei respond to the incoming neutron wave and the neutron sees an effective potential instead of the individual nuclei. The effective potential was first predicted and observed by Fermi [36] on slow neutrons. A neutron that interacts with a surface can then be expected to reflect with some probability from the potential, depending on the incident momentum. This led to the development and application of cold neutron guides, where reflection from shallow angles allows beams of neutrons to be directed to experimental areas.

Neutrons with extremely low energies $E \lesssim 335$ nev or velocities $v \lesssim 8\,\mathrm{m}\cdot\mathrm{s}^{-1}$ are classified as Ultracold Neutrons (UCN). Their kinetic energy is lower than the Fermi potential of certain materials, as defined below, and the neutrons would predominantly be reflected by the material surface. This led to the idealization and development of traps that could

store UCN for long periods of time [29]. A trap for UCN can be built if all the walls are made of a material with sufficiently high Fermi potential. The Fermi potential depends on the coherent scattering length a of the isotope composition of the material. It can be expressed [30] as

$$V_{\mathrm{F}} = \frac{2\,\pi\,\hbar^2}{M_n}\,N\,a\,, \tag{2.1}$$

where N is the number density of the isotope in the material, and M_n the neutron mass. The coherent scattering lenght depends on the depth and range of the attractive potential of a nucleus [30] in such a way that most isotopes have $a > 0$, a requirement for the establishment of a positive Fermi potential, with the largest potential offered by ^{58}Ni ($V_F \simeq 335$ neV) [30].

Because of their ability to be contained, ultracold neutrons offer advantages in the measurement of nuclear properties. Up to careful inspection, the UCN seem to behave like an ideal gas of extremely low temperature, so they can be moved around the laboratory using guides. For instance, they can be removed from the area where they are produced which is very active with spallation neutrons and directed to measurement areas which expect a low background rate. This is the case for the *UCNA* measurement of the neutron βdecay asymmetry, carried out at the Los Alamos National Laboratory [37].

2.1.1 Superthermal UCN production

The methods of UCN production have evolved over several decades and are described in [30] in detail. In general neutrons are first produced by means of nuclear fission in a nuclear reactor, or as products of spallation of neutron-rich materials from accelerated proton beams. One aspect to consider is that a thermal distribution of neutron speeds has a peak at the maximum UCN velocity $v_{max} \approx 8\,\mathrm{m}\cdot\mathrm{s}^{-1}$ for a temperature $T \approx 4$ mK, so that typical temperatures associated with neutron sources, as well as neutron moderators, produce a very small fractional density of UCN. It is possible to increase the UCN density by slowing down neutrons using processes that are not in thermal equilibrium and are not perfectly time-reversible. This includes very clever methods using mechanical objects, such as turbines [38], to slow the neutrons down.

The *nEDM* experiment proposes to use in-situ production of UCN in superfluid Helium [30, 34, 39] using downscattering of a mono-energetic cold neutron beam. In principle, the cold neutrons can interact with the superfluid Helium by releasing a single phonon. Because

of energy and momentum conservation, the interaction is limited by the region in which the dispersion curves for phonons in ^{4}He and for free neutrons meet. Because of this, the only energy that the phonon can carry away is given by the energy of the incoming cold neutron, resulting in a complete stop of the neutron, hence a conversion to UCN. The energy of the incoming cold neutrons is fixed to be $\lambda \approx 8.9\,\text{Å}$ or $E \approx 1meV$ for maximum yield of UCN. The reverse process of phonon absorption is also possible, but greatly reduced if the temperature of the bath is low so that the density of phonons of that energy is low.

2.2 Measurement of the neutron EDM

The permanent EDM of the neutron can be measured as a change in Larmor precession frequency of polarized neutrons in the presence of an electric field E. Polarized UCN are allowed to precess freely about a reference magnetic field $B_0 \approx 30$ mG which is uniform over the volume of the trap. An electric field $E \approx 75\,\text{kV}\cdot\text{cm}^{-1}$ parallel to B_0 is also applied to the cell. The Hamiltonian of a neutron with spin vector $\boldsymbol{J}/J$ in the external $B+E$ fields is [40] expressed as

$$H = -\mu_n \frac{\boldsymbol{J}}{J}\cdot\boldsymbol{B} - d_n \frac{\boldsymbol{J}}{J}\cdot\boldsymbol{E}\,, \tag{2.2}$$

d_n represents a permanent EDM and $\mu_n \simeq -1.9130427(5)\,\mu_N$ is the magnetic moment [15] of the neutron expressed in terms of the nuclear magneton μ_N. The neutron spin precesses about the fields with a Larmor frequency

$$\omega = -\frac{2}{\hbar}\left(\mu_n B \pm d_n E\right)\,, \tag{2.3}$$

where the positive sign represents a configuration of E and B fields aligned, and the negative sign anti-aligned. The gyromagnetic ratio can be defined as

$$\gamma_n = \frac{\omega}{B_0} \simeq \left(-1.913\times\mu_N\right)\,\frac{2}{\hbar} \simeq -1.8324\times10^4\,\text{rad}\cdot\text{s}^{-1}\,\text{G}^{-1}\,. \tag{2.4}$$

The Larmor spin precession is not an observable quantity and it must be extracted from the measurement of the accumulated phase of an ensamble of spins after a period of precession in the magnetic field. The phase measurement technique for the *nEDM* experiment is described below.

2.3 Measurement with ^{3}He

The role of ^{3}He in the measurement of the neutron EDM is fundamental for the proposed *nEDM* experiment and represents one of the major technical advances in the increased sensitivity. This section describes how the measurement of the spin precession of the neutrons is performed using ^{3}He atoms, and how the same atoms can be used as co-magnetometer to measure the effective magnetic field in the measurement cells.

2.3.1 ^{3}He as polarization detector

In the *nEDM* experiment the neutron precession frequency will be measured using spin polarized ^{3}He atoms in-situ, as detailed in [34]. A neutron can capture onto a ^{3}He nucleus through the reaction

$$n + {}^3\mathrm{He} \rightarrow {}^3\mathrm{H} + {}^1\mathrm{H} \qquad 764\,\mathrm{keV}\,, \tag{2.5}$$

which depends highly on the alignment of the spins of the incoming particles and is greatly suppressed if the spins are aligned, so a spin polarized ensemble of ^{3}He atoms can be used to measure the relative polarization of the neutrons by measuring the scintillation light produced by ionization of the liquid ·He

The ^{3}He has a nuclear magnetic moment similar to that of the neutron

$$\gamma_3 \simeq 1.11\,\gamma_n \simeq -2.037947093 \times 10^4\,\mathrm{rad}\cdot\mathrm{s}^{-1}\,\mathrm{G}^{-1}\,, \tag{2.6}$$

and its spin will also be precessing about the same magnetic field in the cell during the measurement. Since the polarized ^{3}He atoms co-exist in the same measurement cell as the neutrons, the *nEDM* experiment implements a continuous measurement of the neutron phase with respect to the ^{3}He spin polarization. This is different, for example, from the previous neutron EDM measurement at ILL [32, 33], where the projection of the phase is only measured at a fixed point in time. The resulting capture signal will be modulated at a beat frequency $\omega_s \simeq (\gamma_n - \gamma_3)\,B_0$, which is about 11.1 Hz for a field of 30 mG. A permanent EDM of the neutron would result in an increase or decrease of the scintillation beat frequency, depending on the orientation of the E field with respect to the B_0 field

The electric dipole moment of the ^{3}He atom, which would confuse the measurement of a neutron EDM, is expected to have a small contribution due to the Schiff effect [27] which

applies to most atomic EDM's. This effect is due to the shielding of an external electric field at the nucleus, effected by the electron cloud. The result is an equilibrium condition in which the field is partially canceled at the nucleus so that the effective ^{3}He EDM is greatly reduced. The atomic EDM of ^{3}He is calculated to be orders of magnitude smaller than the current limit of the neutron EDM [41].

2.3.2 Co-magnetometer

In addition to being the detector for the neutron phase in the *nEDM* experiment, the ^{3}He atoms will be also used as a co-magnetometer to measure the magnitude of the magnetic field in the cell. As seen in other precision measurements of the precession frequency [33], any fluctuation in the reference magnetic field B_0 will result in a fluctuation in the precession frequency and lowered sensitivity to a real EDM signal.

The *nEDM* measurement uses two measurement cells that are exposed to the same magnetic field but have opposite E field directions. A difference in precession frequency measured between the two cells would be indicative of an EDM signal. In principle, because the measurement is carried out in two separate cells which share the same magnetic field, a fluctuation in the magnitude of the field would affect the precession frequency equally in both cells, and since the EDM signal comes from the difference in frequencies between the two cells, the measurement is already less susceptible to changes in field. If the field does not vary by the same amount in the two cells, then it will affect the EDM measurement.

In addition, the fact that the detector is polarized ^{3}He precessing about the same magnetic field greatly reduces the influence of magnetic field fluctuations. This is because the gyromagnetic ratios of the two spin species are similar (equation 2.6), so the measurement of the neutron phase by means of n-^{3}He capture gives a shift from the predicted phase of

$$\Delta\phi = \left[(\gamma_n - \gamma_3)\, \Delta B + \frac{d_n}{\hbar/2}\, E \right] \tag{2.7}$$

where ΔB represents a systematic fluctuation in the reference magnetic field, and the second term in the sum is the contribution in phase from the EDM of the neutron d_n under the influence of an electric field E. The sensitivity to fluctuations ΔB is then reduced by a factor of $\gamma_n/(\gamma_n - \gamma_3) \simeq 8.7$ compared to a measurement of the phase done in the fixed lab reference frame.

The proposed *nEDM* experiment takes advantage of two different techniques [34, 35] using the same apparatus to measure the effective precession frequency of the ^{3}He spin precession in order to lower the influence of magnetic field uncertainties on the measurement even further. The two methods have different experimental configurations, representing two semi-independent measurements of the neutron EDM. The two techniques used are introduced below. A third technique aimed to measure the ^{3}He precession frequency is introduced in section 2.3.2.3 and discussed further in section 5.7.1, which could be implemented in the *nEDM* experiment without significant modifications of the apparatus.

2.3.2.1 SQUID Measurement

The measurement using SQUIDs is an additional feature of the free-precession measurement with ^{3}He and the role of ^{3}He as a co-magnetometer. During a measurement, the density and spin polarization of ^{3}He atoms is large enough to produce a time-varying magnetic field that is measurable using SQUIDs [34]. This magnetic field, being in the direction of polarization, will rotate as the ^{3}He spins precess, so that the field magnitude will be measured to oscillate at a frequency $\omega_{\mathrm{SQUID}} = \gamma_3 B$, from which a value for the reference field can be calculated. This measurement is continuous over the measurement period T, so gross changes in the field that happen on a time scale shorter than T could be seen from the SQUID signal and incorporated into the analysis of the capture signal.

2.3.2.2 Dressed Spin Technique

The magnetic field fluctuations would not affect the measurement of a neutron EDM if the gyromagnetic ratios of the ^{3}He and neutron spins were equal. In this case, any phase accumulated during a measurement would be due primarily to the neutron EDM in the electric field.

It is possible to effectively alter the gyromagnetic precession frequency by exciting the spins using a large, non-resonant high-frequency oscillatory magnetic field, transverse to the reference field B_0. The technique is called "spin-dressing" and has been studied in detail for the neutron spin in [42] and for the application in the search for a neutron EDM in [34].

Since the RF field is large with respect to the reference field $B_{\mathrm{rf}} \gg B_0$, and the oscillating frequency is large with respect to the Larmor frequency $\omega_{\mathrm{rf}} \gg \omega_0$, the spin polarization will

precess much faster about the dressing field than the reference field. In this case, the B_0 field can be seen as a small perturbation to the larger dressing field.

The dressing field is perpendicular to B_0 and can be expressed as

$$B_{\rm rf}(t) = B_{\rm rf}\, \cos\left(\omega_{\rm rf}\, t\right) \hat{y}\,, \tag{2.8}$$

with B_0 pointing in the $\hat{x}$ direction. For times that are short compared to the Larmor frequency about B_0, the spin precesses about the large dressing field while keeping the angle with respect to it approximately constant. The normalized spin vector

$$\boldsymbol{\sigma} = \frac{\boldsymbol{J}}{J} \tag{2.9}$$

is being used to represent the direction of spin. The component of spin aligned with $\hat{y}$ should stay approximately constant

$$\Delta\sigma_y \approx 0 \qquad \text{for } \Delta t \ll \frac{2\pi}{\omega_0}\,. \tag{2.10}$$

In this limit σ_y can be used as a well defined quantity for the projection of the spin on the $y-z$ precession plane. The fast precession of the spin about the dressing field is given by integrating the Larmor frequency over time

$$\phi_y = \int_0^t {\rm d}t' \left(-\gamma_s\right) B_{\rm rf}\, \cos\left(\omega_{\rm rf}\, t'\right) \tag{2.11}$$

$$= -\frac{\gamma_s\, B_{\rm rf}}{\omega_{\rm rf}}\, \sin(\omega_{\rm rf}\, t)\,, \tag{2.12}$$

where γ_s is the gyromagnetic ratio for one species of spin s and ϕ_y represents the phase about $\hat{y}$, the axis of the dressing field. This shows that the phase ϕ_y will not accumulate over time but will rather oscillate at the dressing frequency. The spin component σ_z will oscillate in value as

$$\sigma_z(t) = \sigma_z(0)\, \cos(\phi_y(t)) + \sigma_x(0)\, \sin(\phi_y(t))\,, \tag{2.13}$$

with initial spin values at time $t = 0$. Over the period of one dressing field oscillation

$T = 2\pi/\omega_{\rm rf}$, the average component of the spin is given by

$$\langle \sigma_z \rangle = \sigma_z(0)\ \langle \cos\phi_y \rangle = \frac{1}{T}\int_0^T \mathrm{d}t\ \cos\left[\frac{\gamma_s\, B_{\rm rf}}{\omega_{\rm rf}}\ \sin(\omega_{\rm rf}\, t)\right]\ \sigma_z(0) \tag{2.14}$$

$$= J_0\left(\frac{\gamma_s\, B_{\rm rf}}{\omega_{\rm rf}}\right)\ \sigma_z(0)\,, \tag{2.15}$$

where $J_0(x)$ is the Bessel function of the first kind of order 0 and only the non-vanishing cosine integral was included. This approximation is valid if the period T of oscillation is in the limit of equation 2.10 which can be expressed as the ratio

$$Y = \left|\frac{\gamma_s\, B_0}{\omega_{\rm rf}}\right| \ll 1\,. \tag{2.16}$$

An additional precession about the smaller B_0 field aligned with the $\hat{x}$ direction would change the spin component aligned with $\hat{y}$

$$\mathrm{d}\sigma_y \simeq -\langle \sigma_z \rangle\ \omega_0\, \mathrm{d}t \tag{2.17}$$

$$= -J_0\left(\frac{\gamma_s\, B_{\rm rf}}{\omega_{\rm rf}}\right)\ \sigma_z(0)\, \omega_0\, \mathrm{d}t\,, \tag{2.18}$$

with ω_0 representing the bare precession frequency about the B_0 field, and where the time average value of the σ_z component is used for times short with respect to ω_0 but long compared to the period of dressing field oscillation. This results in the effective frequency of precession about B_0 being scaled by the Bessel function, and the spin can be referred as *dressed* with respect to B_0. It is possible to introduce an effective gyromagnetic ratio

$$\gamma_s^{eff} = \gamma_s\, J_0(X_s)\,, \tag{2.19}$$

with the dressing parameter X_s defined to be

$$X_s = \frac{\gamma_s\, B_{\rm rf}}{\omega_{\rm rf}}\,, \tag{2.20}$$

in terms of gyromagnetic ratio of the spin species s. Figure 2.1 shows how the effective gyromagnetic ratios of neutrons and ^{3}He spins change with the dressing parameter $X = X_n$, specified for the gyromagnetic ratio of the neutron.

The dressed spin technique can be used to match the gyromagnetic ratios of the two

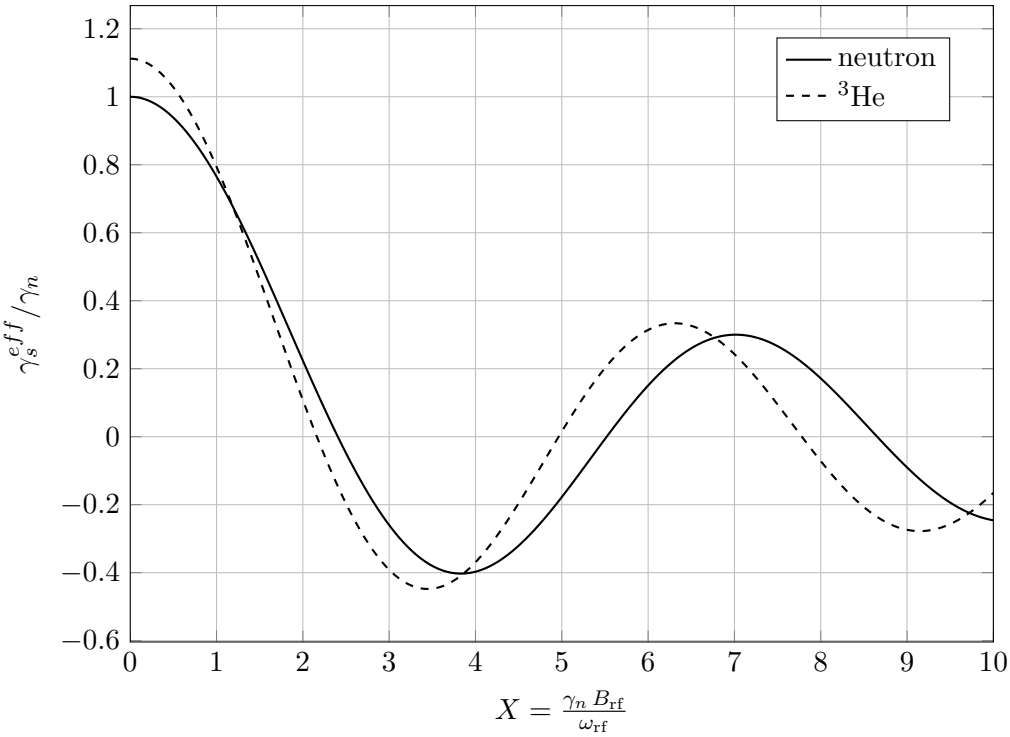

Figure 2.1: Plot of the Bessel functions that determine the effective gyromagnetic ratios of neutrons and ^{3}He atoms as a function of dressing parameter $X = \frac{\gamma_n B_{\rm rf}}{\omega_{\rm rf}}$. The values of the gyromagnetic ratios are expressed in terms of the neutron gyromagnetic ratio γ_n. When the two curves cross each other, the effective gyromagnetic ratios of the two spin species are matched and the spins will precess at the same frequency about B_0.

spin species. This can be done by picking a critical value of the dressing parameter that would satisfy

$$J_0(X_c) = \alpha\, J_0(\alpha\, X_c) \tag{2.21}$$

with $\alpha = \gamma_3/\gamma_n \simeq 1.11$. Table 2.1 lists the first few solutions to equation 2.21.

2.3.2.3 Ramsey technique

In addition to the two modes of operation described above, it might be possible to incorporate the Ramsey technique of separated oscillatory fields [43] into a *nEDM* measurement, in order to measure the ^{3}He phase at the very end of an EDM measurement run. The Ramsey technique relies on the coherence between the frequency of Larmor precession of a spin in a constant magnetic field, with that of a clock in the form of a oscillating magnetic field, resonating at the Larmor frequency in order to induce transitions in the spin system. Two pulses of the oscillating field are separated in time, or equivalently in space for particles

X_c	γ^{eff}/γ_n	γ^{eff}/γ_3
1.189	0.677	0.752
3.861	−0.403	−0.448
6.773	0.291	0.324

Table 2.1: Critical dressing parameters for which the effective gyromagnetic ratios γ^{eff} of neutron and ^{3}He spins are matched. The effective gyromagnetic ratio is expressed in terms of the bare values for both species of spin.

moving in a definite direction, with a period of free precession in between, where the phase accumulates. The second pulse can induce transitions in the spin most effectively if the phase accumulated during the period of free precession matches the phase of the oscillatory field. This method has been used in precision measurements of the gyromagnetic ratios of spin species. The method has been applied to the measurement of the neutron EDM, as it is in the case for the first search for a neutron EDM [2]. It is also the technique used in the recent ILL measurement [32, 33] to measure the phase of the UCN after precession in the $B + E$ fields. Alternatively, a precision measurement of the static magnetic field can be performed if the gyromagnetic ratio of the precessing spin is well known.

The density of ^{3}He in the cells is large enough so that near the end of the measurement period T, when a relatively small number of UCN are still in the cell, it is almost unchanged. The coherence of the ^{3}He spin ensemble with the $\pi/2$ oscillatory field that was used to rotate both species of spins into the precession plane, can be used to measure the phase of the ^{3}He spin.

At the end of the run, it could be possible to pulse the $\pi/2$ oscillatory field again to rotate the ^{3}He spin ensemble back to its original orientation along $\hat{x}$ before the start of the EDM measurement. The cold neutron beam can then be allowed into the measurement cells, with the neutron polarization also aligned with $\hat{x}$. If the two spin polarizations are not well aligned, the capture of polarized neutrons on ^{3}He would produce a strong scintillation signal.

The parameters that allow the $\pi/2$ pulse to rotate both neutron and ^{3}He spins into the precession plane, $\omega_{\pi/2}$, $B_{\pi/2}$ and $\tau_{\pi/2}$, are chosen to minimize the out of plane spin component of both species, as will be explained in section 5.7. Some freedom exists in choosing these parameters, and the frequency can be chosen away from the resonant ^{3}He Larmor frequency. Together with the measurement period T of free precession, a suitable

set of parameters can be chosen so that the resolution of the ^{3}He phase measurement is highest, that is, so that the measured phase is away from resonance by $\sim \pi/2$.

The average holding field could be calibrated using a few phase measurements, varying the period of free precession T between runs, and analyzing the change in capture. Once the magnetic field is known the phase information can be used to measure frequency shifts in the ^{3}He precession during actual EDM runs. If the precession in the two cells differs due to systematic geometric phase effects due to the motional $v \times E$ field, a measurement of the phase difference can be used to estimate the effect. This method is discussed more thoroughly in section 5.7.1, where a Monte Carlo simulation is used to analyze the response of the spin system to the second oscillatory pulse.

2.4 Sensitivity

The sensitivity of the new *nEDM* measurement is proposed to be

$$\sigma_{\mathrm{EDM}} \approx 5 \times 10^{-28}\,\mathrm{e}\cdot\mathrm{cm} \qquad 90\%\,\mathrm{C.L.}\,, \tag{2.22}$$

a couple of orders of magnitude better than the current limit [33] set by ILL. Using the proposed design parameters [34,35] the sensitivity can be computed following the approach of Chibane [44], using the minimization of a χ^2 statistic, for an oscillating signal subject to statistical noise. In principle, the frequency shift due to introduction of an electric field E is the quantity measured to extract an EDM, but the observable is in fact the projection of the phase of the neutron spin, by means of capture onto ^{3}He nucleus, which is a quantum measurement and is subject to statistical noise. In addition, the β decay of the neutron provides a large source of background.

The oscillating signal decays in time as neutrons are either captured onto ^{3}He or undergo β decay. In order to get an estimate of the sensitivity, the formalism of [44] can be adapted for the case of a decaying signal if the average signal over a measurement time T_m is computed. The variance in frequency is given by

$$\Delta\nu^2 = \frac{6}{\pi^2}\,\frac{1}{T_m^3}\,\left(\frac{\bar{I}}{\bar{A}^2}\right)\,, \tag{2.23}$$

where I represents the expected background and A the amplitude of the oscillating signal.

The background and the frequency signal do depend on many experimental parameters, such as the initial polarizations of the spins, the spin relaxation and the efficiency in detecting the signals. A numerical estimate of the variance for one measurement period of T_m, with some constrained experimental parameters as per [35], and the major contributors to the uncertainty left free, is given by

$$\Delta\nu \simeq \frac{1.4 - 1.8}{T_m \sqrt{N_0}\, P_n\, P_3}\,\mathrm{Hz}\,, \tag{2.24}$$

where N_0 represents the number of neutrons in the cell at the start of the measurement, while P_n and P_3 represent the initial polarizations of neutrons and ^{3}He spins. The assumption has been made that the measurement time is comparable to the effective lifetime of neutrons in the cell. With a time $T_m \simeq 1000$ s, an initial neutron population of $N_0 \simeq 3.5 \times 10^5$ and initial polarizations no less than 95%, the frequency variance becomes

$$\Delta\nu \simeq (2.6 - 3.4) \times 10^{-6}\,\mathrm{Hz}\,, \tag{2.25}$$

per cell per run. The sensitivity to a neutron EDM depends on the applied electric field $E \simeq 74\,\mathrm{kV \cdot cm^{-1}}$, so that running for a full day and assuming a $\sim 50\%$ live time due to cleaning and filling the cells this becomes

$$\Delta d_n \simeq \frac{1}{9}\,\frac{h}{2}\,\frac{\Delta\nu}{E} \simeq (8 - 10) \times 10^{-27}\,\mathrm{e \cdot cm}\,, \tag{2.26}$$

where the factor of 1/9 represents the contribution from both cells and 40.5 runs in a day. In order to reach the planned measurement sensitivity, a runtime of about one year of measurement days is necessary.

Several improvements to the measurement techniques should be noted when comparing the new *nEDM* planned experiment to the recent ILL measurement [33] of the neutron EDM. An obvious sensitivity increase comes from the electric field strength being increased by a factor ~ 7 due to the possibility of using liquid Helium as a dielectric. Some considerations regarding the production and sustainability of the large electric field are discussed in chapter 4. A statistical advantage comes from the increase of the statistical sample in the cells by a factor of ~ 10 per cell, together with a continuous measurement of the neutron-^{3}He capture signal. The increase in UCN production is offset by a much longer fill time of

the apparatus (1000 s vs. 20 s), but the measurement time is also increased by a factor of $5-6$.

The systematic limitations to the sensitivity to the neutron EDM come from the possible variations of the magnetic field during and between measurement cycles. Systematic effects that result in a false EDM signal also are of concern for a reliable measurement. Some systematic considerations for the planned measurement are addressed in chapter 5.

2.5 Overview of selected problems

This manuscript addresses a limited set of issues that have been brought forward in the planning of the experiment, which are related to the participation of Caltech in the *nEDM* collaboration.

Because of the enhanced sensitivity of the planned experiment, the uniformity of the magnetic fields is of major concern. The design, prototyping and testing of magnetic coils planned for the measurement is one of the major responsibilities that Caltech carries out. A half-scale prototype of the coils used to produce the reference B_0 field is actively being tested at Caltech. This work introduces some of the general concepts that have been used in the design and modeling of magnetic coils in chapter 3. In particular, the focus of this work is on the design of magnetic coils for the dressed spin measurement.

Chapter 4 describes one phase of the effort undertook for the collaboration at Los Alamos National Laboratory in the establishment of a large electric field in liquid Helium, necessary for the planned sensitivity. The measurement on the early high voltage prototype discussed in this work did not conclusively demonstrate the capabilities of the system. Some design issues were to blame that were extraneous to the physical limitations that were being tested. A new effort to test the capabilities of an improved system are being carried out again at LANL and the results are very promising.

The study of a selected set of systematic effects that are of concern to the planned measurement are discussed in chapter 5. The issues are a concern because the enhanced sensitivity of the measurement has reached the level where some effects that mimic an electric dipole moment dominate. The studies are related to the uniformity of the magnetic fields and so have been a partial responsibility of Caltech. A suite of Monte Carlo simulations has been developed to study issues specifically for the geometry of the *nEDM* experiment.

The results of the simulations have been consistent with other studies of the same effects.

An analysis framework was sought in preparation for the *nEDM* measurement data collection. The purpose of the effort was to familiarize the collaboration with the expected data and provide a few independent methods of extraction of an EDM signal. For this purpose, a large set of Monte Carlo data was created within the collaboration to test the different fitting methods. One such method is discussed in chapter 6, which uses an unbinned likelihood.

Chapter 3

Modeling of the magnetic coils and design considerations

The measurement of the neutron Electric Dipole Moment relies on techniques which effectively compare the energy states of the neutron in magnetic and electric fields. For this reason, uniform magnetic fields play important roles in the experiment, and part of the development of the *nEDM* experiment is focused on the design and construction of magnetic coils.

3.1 Transverse coils

The geometry of the experiment favors the use of cylindrical coils, open at each end for access, with magnetic fields transverse to their axes. The $\cos\theta$ coil, is an example of a coil that can be used to generate a uniform field. For instance, a solution can be found for the case of an infinitely long cylindrical shell of radius R with a surface current, for which a transverse magnetic field inside the cylinder is perfectly uniform. The solution is for a current density parallel to the cylinder's axis that follows a sinusoidal so that, in cylindrical coordinates,

$$J_z \propto \frac{1}{R}\cos\theta\ \delta(\rho - R) \qquad\qquad \theta \in [-\pi,\, \pi)\ , \tag{3.1}$$

where the radial $\delta(\rho)$ function constrains the current to the surface of the cylinder and is implied for the remainder of the chapter. This can be derived by computing the magnetic vector potential $\boldsymbol{A}$ for a field that is uniform within a cylinder of radius R, so that $\boldsymbol{B}_{inner} = B_0\,\hat{y}$, and solving for the cylindrically constrained current. In the inner region no currents

are present and the boundary conditions set by a uniform field B_0 pointing in the $\hat{y}$ direction are

$$\begin{pmatrix} B_\rho \\ B_\phi \\ B_z \end{pmatrix} = B_0 \begin{pmatrix} \sin\phi \\ \cos\phi \\ 0 \end{pmatrix} \qquad \text{for } \rho < R\,, \tag{3.2}$$

resulting in conditions on the vector potential of

$$\frac{1}{\rho}\frac{\partial A_z}{\partial \phi} = B_0\, \sin\phi \tag{3.3}$$

$$-\frac{\partial A_z}{\partial \rho} = B_0\, \cos\phi\,, \tag{3.4}$$

where only the z component of $\boldsymbol{A}$ contributes to the field. Viable solutions to the Poisson equation for the current free regions yield

$$A_z = \begin{cases} -\rho\, B_0\, \cos\phi & \text{for } \rho < R \\ -\frac{B_0\, R^2}{\rho}\, \cos\phi & \text{for } \rho > R \end{cases}\,. \tag{3.5}$$

The current distribution at $\rho = R$ is then found to be

$$J_z|_{\rho=R} = -\frac{1}{\mu_0}\,\nabla^2\, A_z = \frac{2B_0}{\mu_0}\frac{1}{R}\cos\phi \tag{3.6}$$

where μ_0 is the magnetic constant.

For a real-world coil, the $\cos\theta$ current distribution can be approximated by a finite number of discrete wires as shown in Figure 3.1. The pairs of opposite current wires are evenly spaced on a diameter of the circle to reproduce the $\cos\theta$ distribution. The length of the cylinder must be finite as well, so the wires need to be connected to their returns in order to form a loop, at the end-caps of the cylinder, wrapping over the circular profile in order to leave the sides open for access, forming a *saddle coil*. Figure 3.2 shows a three dimensional model of a $\cos\theta$ coil.

The angles that specify the location of coil loops to discretize a $\cos\theta$ current distribution are given by equidistant intervals of the integrated current distribution, so that these occur at equidistant points on one of the diameters of the coil, so that for N coil loops, the angles

$\psi_i \in [0,\, \pi]$ for $i \in \{1,\, 2,\, \ldots,\, N\}$ can be expressed by

$$\psi_i = \cos^{-1}\left[\frac{N+1-2\,i}{N}\right] . \tag{3.7}$$

An interesting feature of discretizing a continuous surface current distribution into wires carrying equal current is that some of the locations of the wires for N loops coincide with the locations of a $N/(2\,m+1)$ loops coil. That is, if the number of loops in a coil is divisible by an odd integer, then a smaller coil can be constructed using a subset of loops whose number is given by the quotient. For example, if a frame is built for a 30 loop $\cos\theta$ coil, with the wire positions precisely machined as grooves at the correct locations, then, a set of smaller coils of $N' \in \{10,\, 6,\, 2\}$ loops can be wound on the same frame.

In the infinitely long example, increasing the number of discrete wires improves the uniformity of the field because a better approximation to the $\cos\theta$ distribution is achieved. On the other hand, since the real coil is finite in length, it is not necessarily true that increasing the number of discrete wires improves the uniformity. This is because the end caps, which are at a finite distance from the center of the cylinder, do contribute to the magnetic field, making the optimal number of loops depend on the ratio of length to radius.

3.2 Numerical modeling

The coils designed to produce the magnetic fields for the experiment have been modeled to study the uniformity of the fields in regions of interest and to aid the design of appropriate correction coils. The calculation of the field has been carried out using the Biot-Savart law computed for straight segments of current. Following Griffiths [45], the field at position $\boldsymbol{r}$ produced from a wire segment stretched between points $\boldsymbol{p_1}$ and $\boldsymbol{p_2}$ can be expressed as

$$\boldsymbol{B}(\boldsymbol{r}) = \frac{\mu_0\, I}{4\pi}\, \frac{\hat{\boldsymbol{I}} \times \boldsymbol{s}}{|\boldsymbol{s}|^2}\, |s1 - s2| \ , \tag{3.8}$$

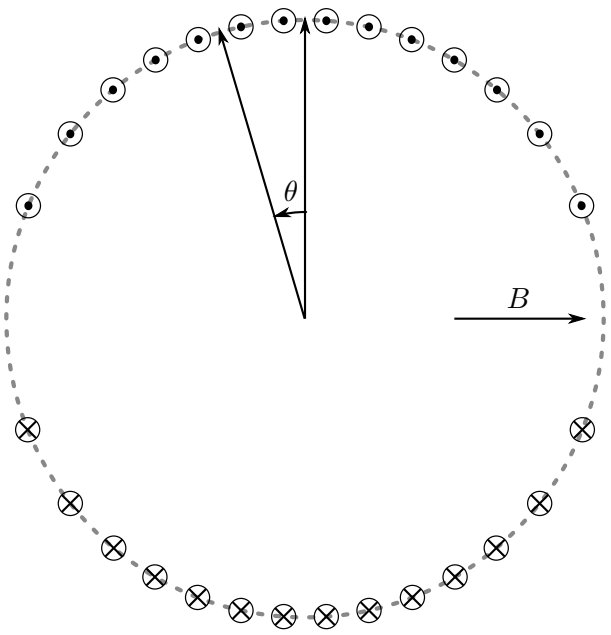

Figure 3.1: Example of discretization of a $\cos\theta$ current distribution over the surface of a cylinder into $N = 14$ saddle coils. Each wire in the upper portion of the circular profile is paired with a return wire in the lower portion and directly underneath it, with the end connections wrapping around the circle on either the left or right side of the circle. This coil produces a uniform field transverse to the axis of the cylinder.

where $\hat{\boldsymbol{I}} = \boldsymbol{I}/I$ is the normalized direction of the current, which is aligned with the segment and flows from $\boldsymbol{p_1}$ to $\boldsymbol{p_2}$. The intermediate quantities in the equation are given by

$$\boldsymbol{s} = \left(\hat{\boldsymbol{I}} \cdot \boldsymbol{d_1}\right) \hat{\boldsymbol{I}} - \boldsymbol{d_1} \tag{3.9}$$

$$\boldsymbol{d_1} = \boldsymbol{p_1} - \boldsymbol{r} \tag{3.10}$$

$$\boldsymbol{d_2} = \boldsymbol{p_2} - \boldsymbol{r} \tag{3.11}$$

$$s1 = \frac{\hat{\boldsymbol{I}} \cdot \boldsymbol{d_1}}{|\boldsymbol{d_1}|} \tag{3.12}$$

$$s2 = \frac{\hat{\boldsymbol{I}} \cdot \boldsymbol{d_1}}{|\boldsymbol{d_2}|}\,. \tag{3.13}$$

The total field is a superposition of the contributions from all the segments of current, so that

$$\boldsymbol{B}_{total}(\boldsymbol{r}) = \sum_{i=1}^{N} \boldsymbol{B}_i^{seg}(\boldsymbol{r})\,. \tag{3.14}$$

If the summation of the segments is done over a closed loop of joined segments, the divergence of the current is forced to vanish, so that the divergence of the field computed also

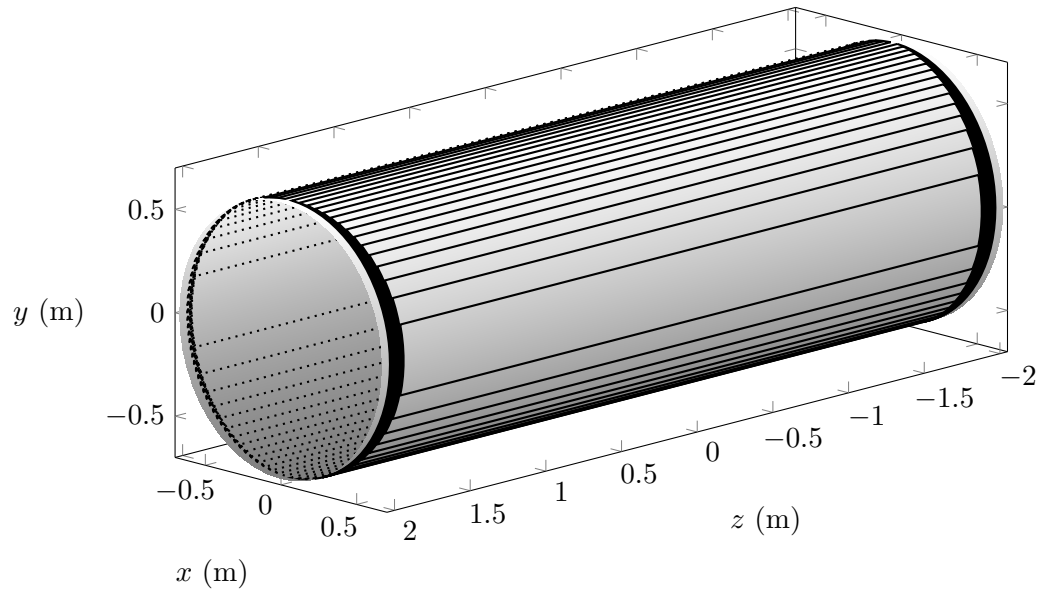

Figure 3.2: Isometric model of a $\cos\theta$ coil of $N = 30$ saddle loops wound on a cylindrical shell of radius $R = 67\,\text{cm}$. The orientation of the magnetic field is transverse to the cylinder's axis and is pointing along the x direction in the figure. The current in the straight wires along the length of the cylinder flows in the positive z direction in the upper portion of the figure ($y > 0$) and returns in the opposite direction on the lower side. At the ends of the cylinder the straight segments of wire turn into arcs and run along the circumference of the cylinder to meet their respective return wire. Two disjoint sets of saddles, for $x > 0$ and $x < 0$, are then distinguishable and their arcs of wire "bunch up" at the ends of the cylinder on opposite sides.

vanishes, which satisfies Maxwell's equations.

Sections of wire that are not straight are approximated by sub-dividing the wire's curved path into small straight segments using a divide-and-conquer method. Given a curved path between two points, a segment stretched between the two points is used as an approximation of the path. Iteratively, vertices are added along the curved path to split the segmented one into smaller segments in order to correct the "worst offending" point of the path, until the distance from the original path to the approximated segmentation is less than the desired tolerance $\delta \sim 100\,\mu$m at all points on the path.

A piece of software used to numerically compute the magnetic fields was written in `C++` and interfaced with Python for simplified use. The abstraction of the coil in the program is a simple collection of closed current loops, where each loop is comprised of a doubly-linked list of straight segments. To respect Maxwell's equations using the Biot-Savart equation for segments of wire, each loop is checked to be continuous by iterating through its segments making sure that pairwise neighboring segments share a vertex. This also ensures that each loop is closed.

Several coil geometries, primarily concerned with the modeling of cylindrical coils, were developed in Python and linked to the compiled code. With this system, all the geometrical considerations that determine the position of short segments of wire, including coordinate transformations, are handled outside the compiled code. The field calculations, which, for any point in space require summing the B field contributions from all coil segments, are handled by the optimized compiled code. This allowed great flexibility in the development of coil geometries together with the availability of software tools [46] which visualize results with ease.

3.3 Dressing Fields

The dressed spin measurement technique described in Section 2.3.2.2 relies on the use of a magnetic field applied transversely to the reference field B_0 and oscillating at a relatively high frequency ($\sim$ 3 kHz) in order to effectively modify the precession frequency of the particles in the cells. This dressing field could easily be produced by a replica of the B_0 reference field coil, as a $\cos\theta$ coil coaxial to B_0 and rotated by 90 degrees with respect to it. Unfortunately, the situation is complicated by the fact that the frequency of oscillation

of the dressing field and its magnitude ($B_{\rm rf} \simeq 1\,\mathrm{G}$) are large enough to induce sizable eddy currents in nearby electrical conductors.

A primary concern regarding induced currents for the experiment is the possibility of large resistive heating that could be dissipated by conducting materials into the lowest temperature components, resulting in ineffective or excessively expensive cooling methods. In addition, the induced currents can produce field distortions near the conductors that could affect the field uniformity in the measurement cells.

Of particular concern, is the presence of a large ferromagnetic cylindrical shell just outside the B_0 coil which is designed to shield from external magnetic fields and increase the homogeneity of the field inside the measurement cells. The ferromagnetic shield is electrically conductive and it would be heated by the oscillating dressing field. The schematic section of the magnetic package in figure 3.3 shows the location of the ferromagnetic shield with respect to the dressing coils. Table 3.1 summarizes their dimensions.

The resistive heating power generated from a dressing coil design can be estimated by computing the average B field magnitude at points on the inner surface of the ferromagnetic shield, adapting the formalism in Jackson [47] for a conducting material in the presence of an alternating field of frequency $\omega_{\rm rf}$. The eddy currents induced inside the material in turn produce a magnetic field that partially cancels the external field, so that the field inside the material decreases with depth z into the material as

$$H(z) \approx H(0)\, e^{-z/\delta} \tag{3.15}$$

with a characteristic length or *skin depth*

$$\delta = \sqrt{\frac{2}{\mu\,\sigma\,\omega_{\rm rf}}} \tag{3.16}$$

determined by the oscillation frequency $\omega_{\rm rf}$ of the applied field, the material's conductivity σ and its magnetic permeability μ.

The resistive power density dissipated into the material from induced eddy currents is given by

$$\frac{P_r}{\Delta V} = \frac{1}{2}\,\mu\,\omega_{\rm rf}\,H^2\,e^{-2z/\delta}. \tag{3.17}$$

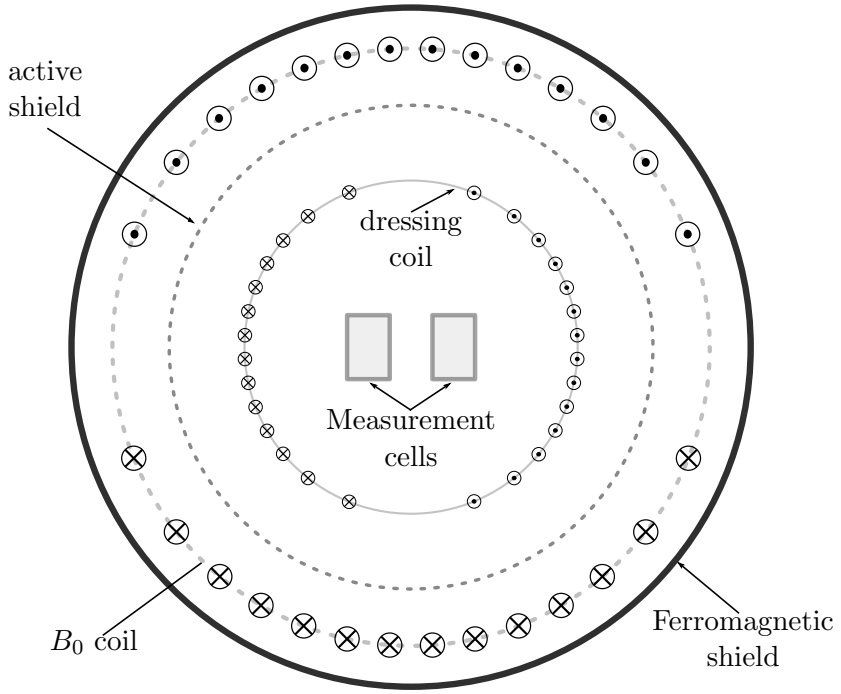

Figure 3.3: Not-to-scale schematic section of the inner magnetic package for the *nEDM* experiment. All coils and shields are cylindrical shells coaxial to each other. The reference magnetic field B_0 is produced by the outermost $\cos\theta$ coil. The combination of dressing and active shield coils produce the oscillating dressing field, transverse to B_0. The magnetic package is enclosed in a ferromagnetic shield which improves the uniformity of the reference field, while providing shielding from external fields. Not shown are several other larger cylindrical shells of superconducting material that provide additional shielding from external fields. Table 3.1 summarizes the physical dimensions of the inner magnet package.

Magnet	R (cm)	L (m)
B_0 coil ($\cos\theta$ coil)	65	4
FM shield	67.3	4.27
inner dressing coil ($\cos\theta$ coil)	50	3
active shield	59	4

Table 3.1: Dimension specifications of the magnet package for the *nEDM* measurement.

Integrating over the thickness t of the material yields a power density over its surface of

$$\frac{P_r}{\Delta A} = \frac{1}{4}\,\mu\,\omega_{\rm rf}\,\delta\,\left(1 - e^{-2t/\delta}\right)\,H^2 \tag{3.18}$$

$$\simeq \frac{1}{4}\,\sqrt{\frac{2\,\mu\,\omega_{\rm rf}}{\sigma}}\,H^2 \qquad \text{for } \frac{t}{\delta} \gg 1 \tag{3.19}$$

$$\simeq \frac{1}{2}\,\mu\,\omega_{\rm rf}\,t\,H^2 \qquad \text{for } \frac{t}{\delta} \ll 1\,. \tag{3.20}$$

A worst case estimate for the resistive heat dissipation into the ferromagnetic shield can be calculated by assuming that the magnetic field B generated by the dressing coil at the surface of the shield is not reduced by the currents induced on the shield itself. The magnitude of the magnetic field is calculated for points on the inner surface of a thick $t \gg \delta$ cylindrical shield to obtain

$$P_r = \frac{1}{4\,\mu_0^2}\,\sqrt{\frac{2\,\mu\,\omega_{\rm rf}}{\sigma}}\,\int {\rm d}A\;|B(\boldsymbol{x})|^2 \tag{3.21}$$

where the relation $\boldsymbol{B} = \mu_0\,\boldsymbol{H}$ has been used for the field just outside the ferromagnet. The magnetic permeability of the ferromagnet μ has been assumed to be constant in this frequency regime. In general, the heat dissipated from the induced eddy currents in the shield can be reduced if the average field RMS at the shield is reduced.

For the *nEDM* measurement, thin ($\simeq 20\,\mu$m) layers of Metglas have been chosen for the ferromagnetic shield. The DC magnetic permeability of Metglas 2705M is reported [48, 49] to be $\mu \sim 3 - 5 \times 10^5\,\mu_0$ and its resistivity $\rho \simeq 1.36\,\mu\Omega\cdot$m. A measurement of the resistivity was performed on a sample of Metglas cooled to liquid Helium temperature to determine if a substantial change in resistivity would be noticed. The measurement was done at the Eisenstein laboratory at Caltech [50]. The resistivity was measured to be consistent with the specifications and there was no significant change when brought to 4 K. The permeability of the Metglas is expected to be lower when exposed to the rapidly oscillating dressing field. Assuming a reduced permeability $\mu/\mu_0 \sim 10^3 - 10^4$, the resulting skin depth of Metglas is $\delta \simeq 200 - 600\,\mu{\rm m}/\sqrt{\nu[{\rm kHz}]}$. Since the shield would consist of $3 - 4$ layers of Metglas the resulting thickness $t \simeq 80\,\mu$m would be less than the skin depth and equation 3.20 can be used to estimate the heating. If the root mean square of the oscillating field is of order 1 Gauss over the surface of the ferromagnetic shield, then the power per unit area dissipated in the form of eddy current resistive heating is on the order

$P_r/\Delta A \simeq 5 - 30\,\mathrm{W} \cdot \sqrt{1/\mathrm{kHz}} \cdot \mathrm{m}^{-2} \cdot \mathrm{G}^{-2}$, for a frequency of $\omega_{\mathrm{rf}} = 2\,\pi \times 3\,\mathrm{kHz}$. The shield area is $A \simeq 18\,\mathrm{m}^2$, yielding a power dissipation on the order of $P_r \approx 100\,\mathrm{W}$. If the field at the center of the full scale dressing coil is $B(0) \simeq 1\,\mathrm{G}$, then the average square magnitude of the unperturbed field over the surface of the ferromagnetic shield has been computed to be approximately $\sqrt{\langle B^2 \rangle} \simeq 0.5\,\mathrm{G}$, for coils of dimensions specified in table 3.1. This estimate of the power dissipated can be $\sim 10 - 100$ times larger than the actual value, depending on the AC permeability of the ferromagnetic material and on the field reduction expected from the response of the ferromagnetic shield. Nonetheless, the value is large compared to what a cryogenic budget usually allows, especially if the components need to be cooled near liquid Helium temperatures. The next sections describe a possible solution to reduce the impact of resistive heating, with the goal of reducing the heat dissipation to values below a Watt.

3.3.1 Active Shielding

In order to reduce the impact of the oscillating dressing field on the ferromagnetic shield, a set of coils can be designed to refocus the magnetic field into the measurement region and away from the shield. A concept introduced by [51] is implemented by [52] where a special *active shield* coil screens the field produced by a $\cos\theta$ coil for application in NMR magnet design.

A pair of coaxial cylindrical coils of different radii $a < b$ can be designed so that the magnetic field produced by the inner coil is effectively reduced for $\rho > b$. In this scenario, the ferromagnetic shield, which is a cylindrical shell coaxial to the coils, would be at a radius $r_{\mathrm{FM}} > b$ in the region of lower field. The oscillating currents driving the two coils need not be the same, but they should be in phase with each other and their ratio fixed to minimize the field at the shield. In general, the current in the outer dressing coil would run in the opposite direction of the current in the inner coil to obtain cancellation.

Since the outer active shield is effectively fighting the establishment of a field by the inner coil, the field in the measurement volume would be reduced, so that in order to restore its desired strength, the current in both inner and outer coils must be increased. In the limit where the two coils are on cylindrical shells at radii not too far apart (i.e. $b = a + \delta r$), the current in the coils needed to establish a finite field in the center of the coil would be divergent as $\delta r \to 0$.

By idealizing a thin, infinitely long cylindrical shell of superconducting material at radius b, coaxial to the inner cylindrical coil at radius a, the condition for the magnetic field to vanish for $\rho > b$ is met as the induced currents on the surface of the superconducting shell cancel the field perfectly in a manifestation of the Meissner effect. If the surface current distribution on the idealized superconducting shell can be computed, the shell can be replaced by a real actively driven coil at the same radius that mimics the current distribution of the superconductor.

Following [52] and [53], the magnetic field due to a current constrained to the surface of a cylinder of radius r can be computed, in cylindrical coordinates $(\rho,\, \phi,\, z)$, for regions inside and outside of the cylinder using a Fourier transform of the current density $\boldsymbol{J}$ expressed as

$$F_z^m(k) = \frac{1}{2\,\pi} \int_{-\pi}^{\pi} \mathrm{d}\phi\, e^{-i\,m\,\phi} \int_{-\infty}^{\infty} \mathrm{d}z\, e^{-i\,k\,z}\, J_z(\phi,\, z), \tag{3.22}$$

where only the component in z of the current density has been used because of the lack of current in the radial direction and the divergence-less of the current density $\nabla \cdot J = 0$, resulting in the condition on the other Fourier component

$$F_\phi^m(k) = -\frac{k\,s}{m}\, F_z^m(k)\,, \tag{3.23}$$

where s is the radius of the cylindrical shell of current. The magnetic field induced by a current constrained to a cylindrical shell of radius s can be expressed at any point $(\rho,\, \phi,\, z)$

as

$$\begin{pmatrix} B_\rho \\ B_\phi \\ B_z \end{pmatrix} = \frac{\mu_0}{2\,\pi} \sum_{m=-\infty}^{\infty} e^{i\,m\,\phi} \int_{-\infty}^{\infty} \mathrm{d}k\, e^{i\,k\,z}\, k\, s^2\, F_z^m(k) \times$$

$$\times \begin{cases} K'_m(k\,s) \begin{pmatrix} \frac{k}{i\,m}\, I'_m(k\,\rho) \\ \frac{1}{\rho}\, I_m(k\,\rho) \\ \frac{k}{m}\, I_m(k\,\rho) \end{pmatrix} & \text{for } \rho < s \\ \\ I'_m(k\,s) \begin{pmatrix} \frac{k}{i\,m}\, K'_m(k\,\rho) \\ \frac{1}{\rho}\, K_m(k\,\rho) \\ \frac{k}{m}\, K_m(k\,\rho) \end{pmatrix} & \text{for } \rho > s \end{cases}, \tag{3.24}$$

where the modified Bessel functions of the first kind and second kind, I_m and K_m respectively, have been used, together with their first derivatives I'_m and K'_m. The evaluation is assumed to keep only the real component of K_m. These equations are valid for surface currents constrained on cylindrical shells that are co-axial to each other. In fact, this can also be used to compute the expected induced current on the surface of a superconducting outer shell at radius b, if the condition of total reflection of the field is met, or, equivalently if no field outside the superconductor exists, which for the case of cylindrical geometry is satisfied by

$$B_\rho = 0 \quad \text{for } \rho > b\,. \tag{3.25}$$

Using Equation 3.24 to compute the radial component of the field due to the contribution of the Fourier transforms of the inner coil current distribution $\boldsymbol{J}(\phi,\, z) \rightarrow F_z^m(k)$ at radius a and the unknown distribution $f_z^m(k)$ of the superconducting shell at radius b, the condition of Equation 3.25 is respected if

$$f_z^m(k) = -\frac{a^2\, I'_m(k\,a)}{b^2\, I'_m(k\,b)}\, F_z^m(k). \tag{3.26}$$

The actual current density on the superconducting shell can be computed from the inverse Fourier transform of 3.26. The dressing coil pair would then be comprised of the original inner coil at radius a and a coil at radius b with a current distribution similar to the one

found from the idealized superconducting shell.

3.3.1.1 Application to saddle coils

If the inner dressing coil is taken to be a $\cos\theta$ coil of radius a and length L, and with N saddle coils placed at angles ψ_i carrying a current I, its current density can be expressed as

$$J_z(\phi,\, z) = \sum_{i=1}^{N} \frac{I}{a}\, [H(z + L/2) - H(z - L/2)] \times [\delta(\phi - \psi_i) - \delta(\phi + \psi_i)] \tag{3.27}$$

$$\begin{aligned} J_\phi(\phi,\, z) =& \sum_{i=1}^{N} I\, [\delta(z - L/2) - \delta(z + L/2)] \times \\ & \times \begin{cases} -H(\phi + \psi_i) + H(\phi - \psi_i) & \text{if } \psi_i \le \pi/2 \\ H(\phi - \psi_i) - H(\phi + \psi_i - 2\pi) & \text{if } \psi_i > \pi/2 \end{cases} , \end{aligned} \tag{3.28}$$

where the Dirac delta function $\delta(x)$ and the Heaviside step function $H(x)$ have been used to specify the discrete current carrying wires. The Fourier transform of one of the components is then

$$\begin{aligned} F_z^m(k) =& \frac{I}{2\pi\, a} \sum_{i=1}^{N} \left(e^{-\mathring{\imath}\, m\, \psi_i} - e^{+\mathring{\imath}\, m\, \psi_i} \right) \int_{-L/2}^{L/2} \mathrm{d}z\, e^{-\mathring{\imath}\, k\, z} \\ =& -\frac{2I\, \mathring{\imath}}{\pi\, a\, k}\, \sin(k\, L/2) \sum_{i=1}^{N} \sin(m\, \psi_i)\,. \end{aligned} \tag{3.29}$$

Equation 3.26 can then be used to find the transform of the surface current distribution of the active shield on the cylindrical shell at radius b

$$f_z^m(k) = \frac{2\, a\, \mathring{\imath}\, I\, I'_m(k\, a)}{\pi\, b^2\, k\, I'_m(k\, b)} \sin(k\, L/2) \sum_{i=1}^{N} \sin(m\, \psi_i). \tag{3.30}$$

Inverting the transformation would give the actual surface current distribution $\boldsymbol{J}(\phi,\, z)$, which is a continuous function of ϕ and z.

The active shield would be constructed as a coil comprised of discrete current carrying wires that approximate the perfect shielding condition of equation 3.30, to obtain instead partial cancellation. A useful construction that is also appropriately used in [52] relies on the divergence-less of the current constrained to the surface of the cylindrical shell to

describe the surface current in terms of a vector potential such as

$$\boldsymbol{J}(\phi,\, z) = \boldsymbol{\nabla} \times \boldsymbol{\Psi}\,, \tag{3.31}$$

where only one component, called the *stream function* $\Psi(\phi,\, z) = \Psi_\rho$ is needed to fully describe the surface current. The components of the surface current on a cylinder of radius r can be defined in terms of

$$J_\phi(\phi,\, z) = \frac{\partial \Psi}{\partial z} \qquad \text{and} \qquad J_z(\phi,\, z) = -\frac{1}{s}\frac{\partial \Psi}{\partial \phi}\,. \tag{3.32}$$

The stream function can be computed by integrating one of the current components, and directly from inverting the Fourier component, so that

$$\begin{aligned} \Psi_s(\phi,\, z) &= -\,s \int \mathrm{d}\phi\, J_z(\phi,\, z) && (3.33)\\ &= -\,s \int \mathrm{d}\phi\, \frac{1}{2\pi} \sum_{m=-\infty}^{\infty} e^{\mathring{\imath}\, m\, \phi} \int_\infty^\infty \mathrm{d}k\, e^{\mathring{\imath}\, k\, z}\, F_z^m(k) \\ &= \frac{\mathring{\imath}\, s}{2\pi} \sum_{m=-\infty}^{\infty} \frac{e^{\mathring{\imath}\, m\, \phi}}{m} \int_\infty^\infty \mathrm{d}k\, e^{\mathring{\imath}\, k\, z}\, F_z^m(k)\,. && (3.34) \end{aligned}$$

Because of the definition of the stream function as an integral of the surface current, iso-contours of the stream function represent paths of closed loops of current, so that in order to discretize the continuous current distribution expected from equation 3.30 into a discrete number of wires, each carrying the same current, it is possible to place the wires on contours for equidistant values of the stream function Ψ.

The stream function for the active shield of equation 3.30 is then calculated using equation 3.34 for radius b to be

$$\begin{aligned} \Psi_b(\phi,\, z) &= -\,\frac{a\, I}{b\, \pi^2} \sum_{i=1}^{N} \sum_{m=-\infty}^{\infty} \frac{e^{\mathring{\imath}\, m\, \phi}}{m} \sin(m\, \psi_i) \int_{-\infty}^{\infty} \mathrm{d}k\, \frac{e^{\mathring{\imath}\, k\, z}}{k}\, \frac{I'_m(k\, a)}{I'_m(k\, b)} \sin(k\, L/2) && (3.35)\\ &= -\,\frac{4a\, I}{b\, \pi^2} \sum_{i=1}^{N} \sum_{m=0}^{\infty} \frac{\cos(m\, \phi) \sin(m\, \psi_i)}{m} \int_0^{\infty} \mathrm{d}k\, \frac{\cos(k\, z) \sin(k\, L/2)}{k}\, \frac{I'_m(k\, a)}{I'_m(k\, b)}\,. && (3.36) \end{aligned}$$

Figure 3.4 shows an example of the shape of an active shield coil computed from the stream function of equation 3.35 for a given inner $\cos\theta$ coil. Equidistant contours of the stream functions determine the locations of wires for both inner and outer dressing coils.

Each pattern shown is mapped to a cylindrical surface, where symmetry is implied for $z < 0$ and $\phi > \pi/2$. Figure 3.5 shows a three dimensional model of the active shield coil, with wire locations determined by the stream function.

The expected reduction in heat dissipated into the ferromagnetic shield is shown in figure 3.6 as a function of the ratio between the active shield coil and inner $\cos\theta$ coil current ratio I_2/I_1. The current distribution that provides perfect shielding to the magnetic field created by the inner coil is a continuous distribution, so the effective shielding is finite if the shielding coil is instead constructed with discrete current wires.

3.3.1.2 Solution for a current distribution

It is also possible to compute the shielding current for a finite length but continuous $\cos\theta$ inner current distribution. In this case, the components of the surface current would have a form

$$J_z(\phi,\, z) = \frac{I}{a}\,\cos\phi\,\left[H(z + L/2) - H(z - L/2)\right] \tag{3.37}$$

$$J_\phi(\phi,\, z) = I\,\sin\phi\,\left[\delta(z - L/2) - \delta(z + L/2)\right] \tag{3.38}$$

with return currents on either end-cap at $z = \pm L/2$. The Fourier transform of one of its components

$$F_z^m(k) = \frac{I}{a}\frac{\sin(k\,L/2)}{k}\,\left(\delta_{m,1} + \delta_{m,-1}\right) \tag{3.39}$$

can then be applied to equation 3.26 and 3.34 to compute the stream function

$$\Psi_b(\phi,\, z) = \frac{I\,a}{\pi\,b}\,\sin\phi\int_{-\infty}^{\infty}\mathrm{d}k\,e^{i\,k\,z}\,\frac{\sin(k\,L/2)}{k}\,\frac{I_1'(k\,a)}{I_1'(k\,b)} \tag{3.40}$$

$$= \frac{2I\,a}{\pi\,b}\,\sin\phi\int_{0}^{\infty}\mathrm{d}k\,\frac{\cos(k\,z)\,\sin(k\,L/2)}{k}\,\frac{I_1'(k\,a)}{I_1'(k\,b)}\,. \tag{3.41}$$

This form can be generally computed numerically faster than equation 3.35 for the discrete $\cos\theta$ distribution. In this case, the active shield solution does not depend on the discretization of the inner coil.

Figure 3.7 shows the different shielding effectiveness of an active shield optimized for a continuous $\cos\theta$ current distribution using equation 3.40 as a function of the number of coils

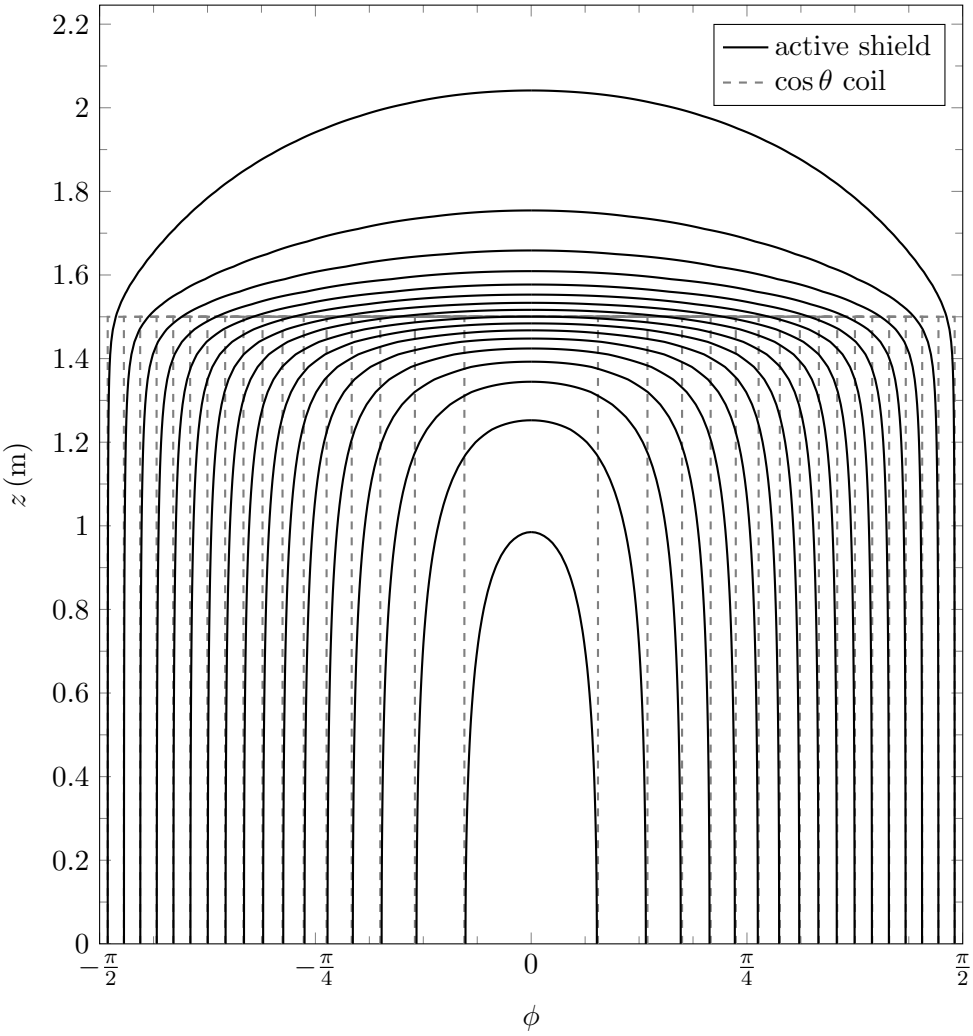

Figure 3.4: Contour plots of a portion of the stream functions $\Psi(\phi\,, z)$ for a $N = 34$ loop $\cos\theta$ inner coil of radius $a = 50\,\text{cm}$ and length $L = 3\,\text{m}$, and an active shield outer coil at radius $b = 59\,\text{cm}$ designed to shield the field produced by the inner coil. The discretization of the active shield current distribution has been chosen to match the number of loops in the inner $\cos\theta$ coil. The contours of the stream function correspond to paths where wires would be wound on a cylindrical surface in order to approximate the desired current distribution. The current in the active shield should run in the opposite direction to the current in the inner coil. Note that the maximum length of the combination of coils is $\sim 25\%$ larger than the original inner coil.

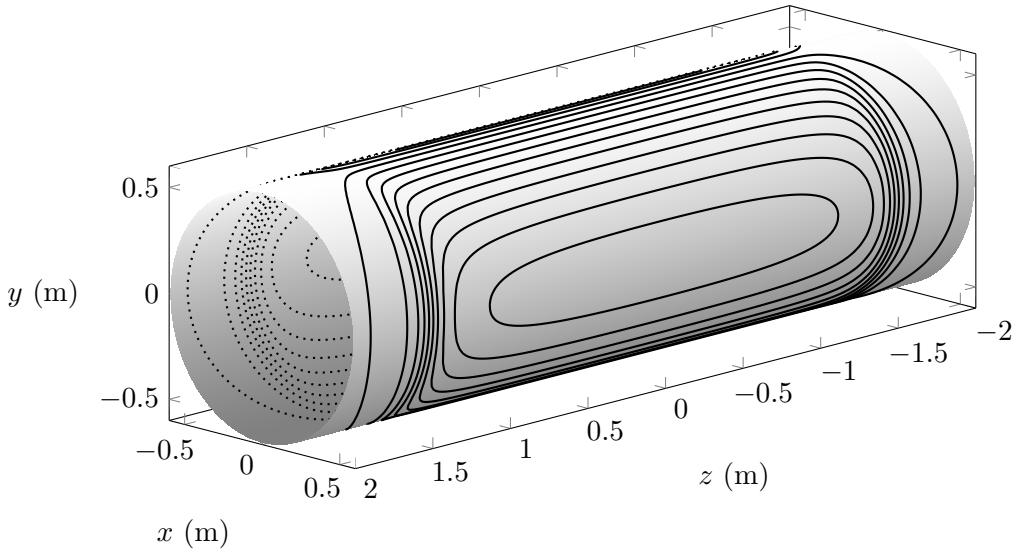

Figure 3.5: Isometric model of an active shield coil constructed on a cylindrical shell of radius $R_2 = 59\,\text{cm}$. The active shield consists of $M = 20$ saddle loops of wire designed to shield the magnetic field flux produced by a inner $\cos\theta$ coil (not shown) of radius $R_1 = 50\,\text{cm}$ and length $L_1 = 3\,\text{m}$. In the figure, the coil is oriented so that the magnetic field points along the x direction.

used to discretize the current distributions of the coils. For comparison, an optimization for a discretized inner coil is also shown. If the active shield current distribution is computed against the continuous $\cos\theta$ distribution of equation 3.37, both discretizations of the number of loops in the inner and outer coil, N and M respectively, will affect the shielding. On the other hand, if the active shield distribution is computed against an already discrete inner coil current distribution for N saddle loops in a $\cos\theta$ arrangement, as in equation 3.27, then only the discretization of the outer active shield current in M coils will affect the shielding. This is also apparent from figure 3.7 where the active shield designed for the discrete inner coil outperforms all other approximations in shielding.

3.3.2 Shielding the active shield

The approach of actively shielding a magnetic coil can introduce gross distortions in the B field. For this reason, it might be sought to use a third active coil to correct the distortions produced by the active shield. It is possible to use the method described above of applying the boundary conditions of a superconducting cylindrical shell to compute the current distribution necessary to correct the field. Furthermore, it is possible to compute the two active coils at the same time for optimal shielding.

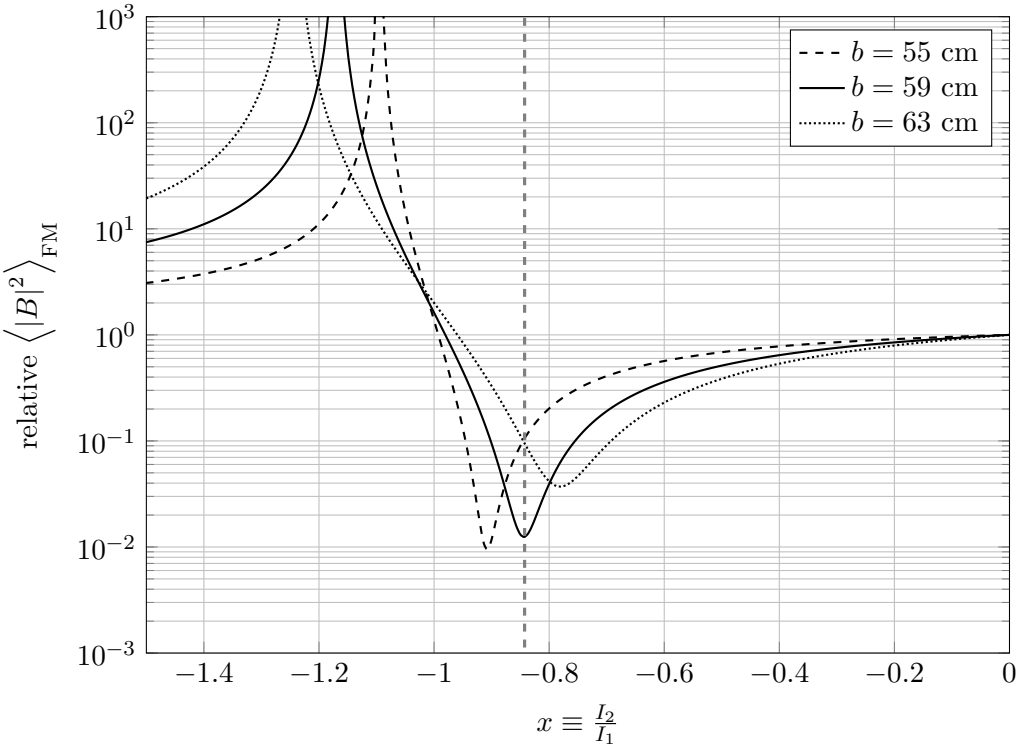

Figure 3.6: Effect of active shielding on the mean magnitude squared of the magnetic field, evaluated on the ferromagnetic (FM) shield surface as a function of the ratio between inner and outer coil currents. The nominal field at the center of the coils is kept constant and the data plotted are relative to the bare $\cos\theta$ value for $x = 0$ (i.e. no active shielding). The model of the coils was constructed with $N = M = 34$ current loops for both the inner coil and the active shield, following the specification of table 3.1. For comparison, shielding for different radii b of the outer active shield are shown. For the geometry of the magnet package ($b = 59$ cm), the best shielding factor (≈ 80) occurs for $x \simeq -0.843$, as shown in dashed gray line. Better shielding factors can be obtained by increasing the number of loops in the active shield, as shown in figure 3.7. The resonances near $x = -1.2$ correspond to ratios of currents that would effectively cancel the field at the center of the coils, resulting in diverging currents to keep the nominal field finite.

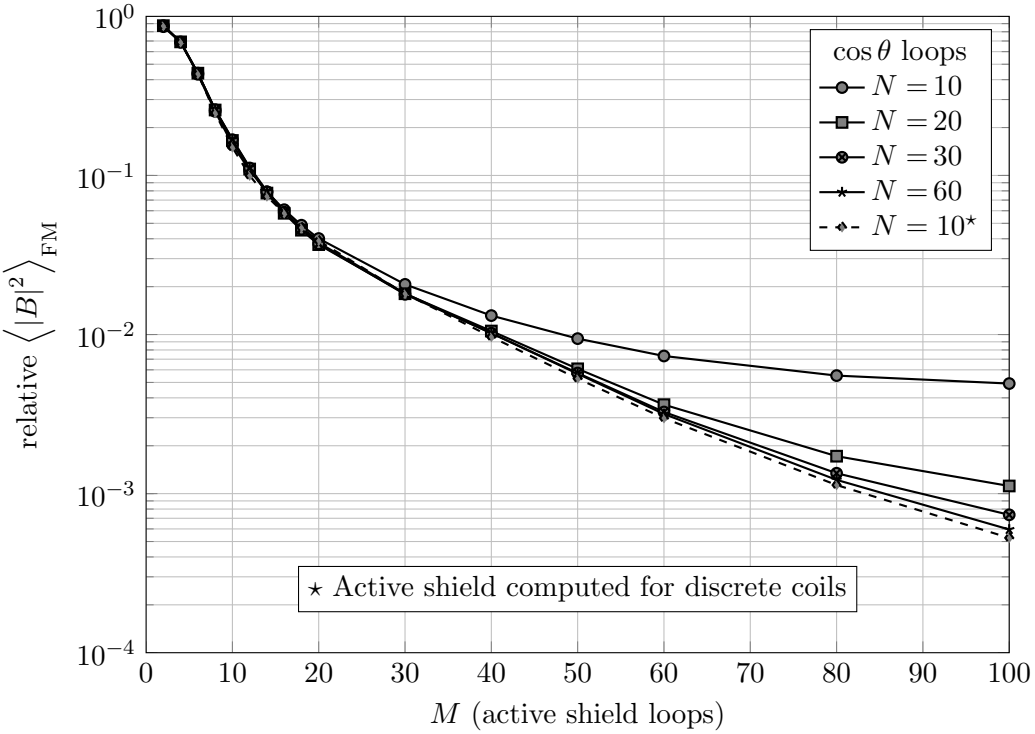

Figure 3.7: Reduction in expected resistive heating as integrated RMS of the B field as a function of the number of active shield loops M. The effective shielding increases as the number of loops M used to approximate the perfect shielding current distribution increases. Different discretizations of the $\cos\theta$ current distribution for the inner coil are also compared, with better shielding for increasing number of loops N in the inner coil. Perfect shielding conditions would apply for $N \to \infty$ and $M \to \infty$. Also shown in dashed line is the shielding effectiveness of an active shield optimized using equation 3.35, as solution for a discrete inner $\cos\theta$ coil.

In an approach described by [54] of *double active shielding*, the field from an active shield can itself be shielded so as to not affect the field in the inner regions of the coils. The boundary condition of equation 3.25 can be adapted to construct an additional shield at radius $c < b$ which would cancel the field produced by the active shield at b for regions $\rho < c$, so that the combined conditions on the radial fields from the three coils at radii a, b and c are

$$B_\rho^{(a+b+c)} = 0 \qquad \text{for } \rho > b \tag{3.42}$$

$$B_\rho^{(b+c)} = 0 \qquad \text{for } \rho < c\,, \tag{3.43}$$

where the field contribution from the shields $(b+c)$ but not from the inner coil is screened at $r = c$. Nothing prohibits the coil c to be built at the same radius as the inner dressing coil so that $c = a$. The inner coil distribution can then itself be redesigned to account for the superposition of two current distributions.

The computation of the current distribution of the two double active shields can be done by solving for the two boundary conditions

$$a^2\, F_a^m(k)\, I'_m(k\,a) + b^2\, f_b^m(k)\, I'_m(k\,b) + c^2\, f_c^m(k)\, I'_m(k\,c) \;= 0 \qquad (\text{for } \rho = b) \tag{3.44}$$

$$b^2\, f_b^m(k)\, K'_m(k\,b) + c^2\, f_c^m(k)\, K'_m(k\,c) \;= 0 \qquad (\text{for } \rho = c)\,, \tag{3.45}$$

where the z component is implied for the Fourier terms of the three coils F_a, f_b and f_c. Given the transformed expression of the inner coil, the resulting transforms of the current distributions on the active shields are

$$f_b^m(k) = -\frac{a^2}{b^2}\left[\frac{I'_m(k\,b)}{I'_m(k\,a)} - \frac{I'_m(k\,c)}{I'_m(k\,a)}\,\frac{K'_m(k\,b)}{K'_m(k\,c)}\right]^{-1} F_a^m(k) \tag{3.46}$$

$$f_c^m(k) = \frac{a^2}{c^2}\left[\frac{I'_m(k\,b)}{I'_m(k\,a)}\,\frac{K'_m(k\,c)}{K'_m(k\,b)} - \frac{I'_m(k\,c)}{I'_m(k\,a)}\right]^{-1} F_a^m(k)\,. \tag{3.47}$$

Ratios of the modified Bessel functions have been used for convenience in equations 3.46 and 3.47 so that the computation can be done using available numerical software libraries which provide an exponentially scaled result [55], so that the exponential scale partially factor out.

The inner coil at radius a can be modeled to be a $\cos\theta$ coil with current distribution

given by 3.37, and the additional active shield can be built at the same radius so that $c = a$. The combination of the three coils can then be built compactly on two cylindrical shells. Moreover, using the stream function method, the current distributions of two coils wound on the same surface can be combined and discretized once, resulting in a total of two coils being constructed. The stream functions in this case can be computed numerically from

$$\Psi_a(\phi,\, z) = -\, I\, \sin\phi\, [H(z + L/2) - H(z - L/2)] \tag{3.48}$$

$$\Psi_b(\phi,\, z) = \frac{2I\, a}{\pi\, b}\, \sin\phi \int_0^\infty \mathrm{d}k\, \frac{\cos(k\, z)\, \sin(k\, L/2)}{k}\, \frac{I'_m(k\, a)\, K'_m(k\, c)}{I'_m(k\, b)\, K'_m(k\, c) - I'_m(k\, c)\, K'_m(k\, b)} \tag{3.49}$$

$$\Psi_c(\phi,\, z) = \frac{2I\, a}{\pi\, c}\, \sin\phi \int_0^\infty \mathrm{d}k\, \frac{\cos(k\, z)\, \sin(k\, L/2)}{k}\, \frac{I'_m(k\, a)\, K'_m(k\, b)}{I'_m(k\, b)\, K'_m(k\, c) - I'_m(k\, c)\, K'_m(k\, b)} \tag{3.50}$$

The modeling of an double active shield for the dressing coil in the *nEDM* experiment has been attempted. Figure 3.8 shows the current distribution of double active shields computed for a test inner $\cos\theta$ coil of length $L = 3\,\mathrm{m}$. The resulting coil package becomes more than twice the length of the original coil, posing problems for the geometry requirements of the dressing coils. Figure 3.9 shows how the addition of the second active shield restores the field uniformity.

It becomes questionable whether the method of double shielding is effective for this geometry: the uniformity of the field will have increased, but the length of the coil will have grown so much that it might be better to use a single active shield computed against a longer inner coil. In the end, it turns out that it is easier to construct a dressing coil with a single active shield to which a small number of shim coils are added to improve the uniformity. The shim coils do not necessarily need to be shielded, if the correction field is small.

3.3.3 Field correction

A small correction coil can be used to improve the uniformity of the dressing field generated by a dressing coil and an active shield combination. The uniformity is important because it impacts the spin relaxation for ^{3}He atoms during a spin dressing measurement. The

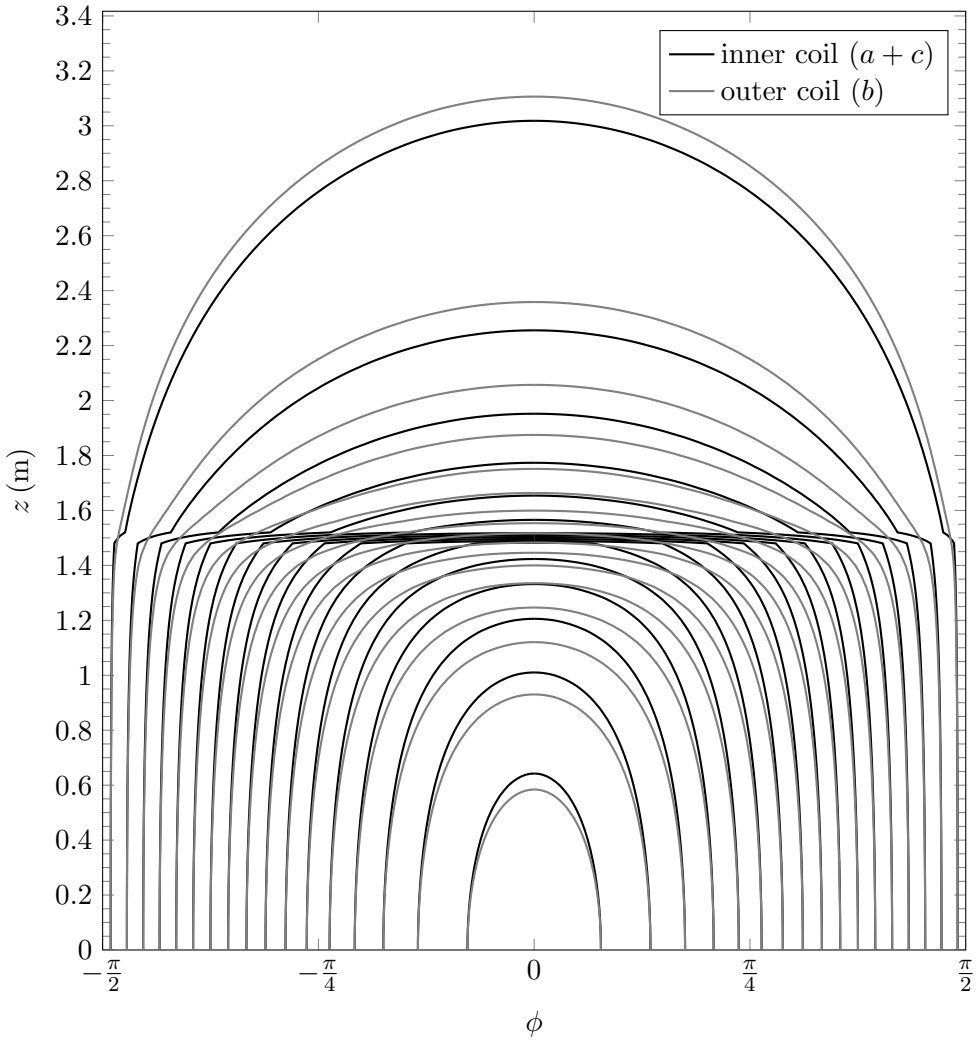

Figure 3.8: Contour plots of a portion of the stream functions $\Psi(\phi, z)$ for a set of double active dressing coils at radii $a = c = 50\,\text{cm}$ and $b = 59\,\text{cm}$. The current distributions the outer and inner shields is computed for a $\cos\theta$ inner coil of length $L = 3\,\text{m}$. The current distribution shown for the inner coil is a superposition of the continuous currents of the inner coil and inner shield discretized together. Note that the length of the double active shielded coils increases to more than twice the length of the original $\cos\theta$ coil.

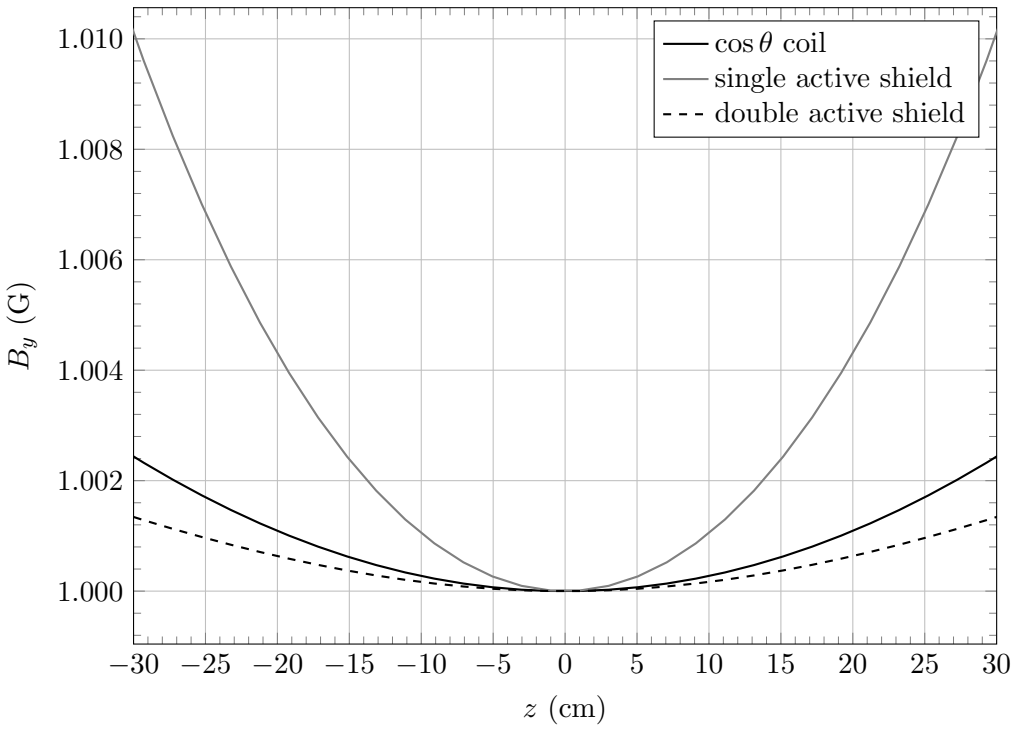

Figure 3.9: Magnetic field profiles in the axial direction for actively shielded and unshielded dressing coils. The currents in the coils have been adjusted so that a normalization of $B_y(0) = 1\,\mathrm{G}$ is obtained. A single active shield changes the profile of the magnetic field of the original $\cos\theta$ worsening the uniformity of the field in the z direction. The double active shield design restores some of the uniformity of the field profile.

relaxation rate follows

$$\frac{1}{T_2} \propto \langle \Delta B^2 \rangle \tag{3.51}$$

as seen in equation 5.50 and adapted in section 5.8. Figure 3.9 shows that there is a large variance of the field along the axis of the coils, which is along the longer side of the measurement cell $L_z = 40$ cm, and the implementation of the active shield increases the field deviation.

A permanent shim coil would be wound on the cylinder that holds the inner dressing coil and connected so that current would flow in series to it. The windings of the shim coil would represent a small contribution to the field compared to the more numerous windings of the inner coil justifying not having to modify the active shield to account for the small change in magnetic field. A random search for the specifications of the shim coil was performed, constrained by a few symmetrical arguments that produce a quadratic field profile. The shims were modeled to be small rectangular saddle coils on the curved surface of the cylinder, where one of the sides is parallel to the axis of the cylinder and the other side runs along a circle on the cylinder. A generalization of the parameters was done so that a shim is specified by a pair of coordinates (ϕ, z) of the diagonal of the rectangle on the surface of the cylinder, with a chosen convention of the current direction specified by the sign of the slope of the diagonal. Without loss of generality, the parametrization assumes that the diagonal of the shim is entirely in one octant of the cylinder surface with $\phi \in [0, \pi/2]$ and $z \in [0, z_{max}]$. To preserve symmetry, the single rectangular shim pattern is reproduced on all octants of the cylindrical surface. The pattern is symmetric about about ϕ and z, as well as the direction of the field. Figure 3.10 shows an example of the symmetric construction of a shim coil over the surface of the cylinder. This parametrization allows for special cases of coils where one or two pairs of rectangular patterns come into contact at the edge of the octant (i.e. $\phi = 0$ or $z = 0$ or both), with currents canceling out on the sides that are touching, so that they can be joined to form a larger loop that spans multiple octants. The saddle coil pairs used in the $\cos\theta$ coil can be defined in this construction as special case coils where one of the points of the rectangular pattern lies on the origin ($\phi = z = 0$).

The parameter space for rectangular shim coils is large as it is possible to add multiple shims to correct the profile. A random search was performed with a cost function designed

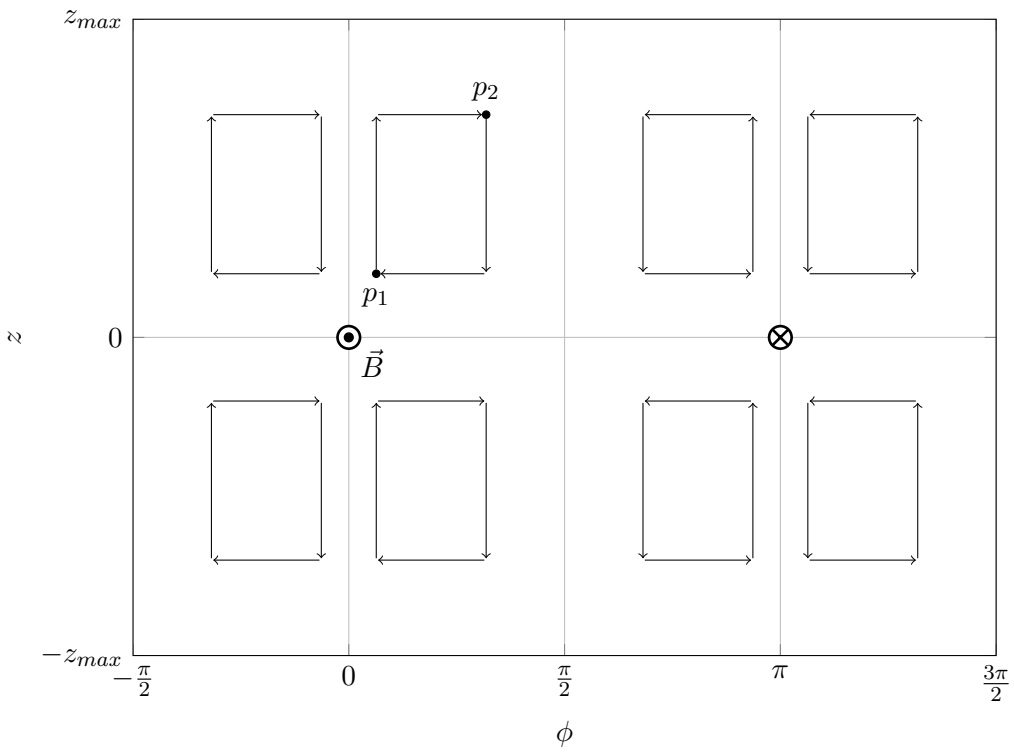

Figure 3.10: Symmetric construction of coils on a cylindrical shell. The axis and direction of the B field is specified and is transverse to the axis of the cylinder. A rectangular pattern is specified by two points p_1 and p_2 in one octant and the pattern is repeated to be symmetric in ϕ and z as well as on the other side of the coil where $\phi > \pi/2$. The special cases where p_1 reaches either the $z = 0$ or the $\phi = 0$ axes result in coalescing of pairs of rectangle loops, with the currents of the segments that are touching canceling. The $\cos\theta$ coil is constructed with coils of this type with $p_1 = (0, 0)$, resulting in saddle pairs.

to improve the $\partial B/\partial z$ profile without significant worsening of the active shielding using a single shim coil constructed as described above. Although the results do not converge to a single design, a well suited example of the shim coil, designed for an inner $\cos\theta$ coil of 30 loops, is specified by resulting in a total of 4 current loops. Pairs of loops are separated by

	ϕ (rad)	z (cm)
p_1	0	42.7
p_2	0.164	74.6

~ 80 cm and are located within the largest gap between coil windings of the $\cos\theta$ coil, on both sides of the coil. The current in the loop runs in the opposite sense as the $\cos\theta$ coil.

3.3.4 Active shield optimization

The results obtained for the specifications of the active shield coils have been verified using the numerical modeling software outlined in 3.2. The resistive heat dissipation has been estimated by computing the total field produced by the inner dressing and outer active shield coils at points on the inner surface of the ferromagnetic shield. The total field can be expressed as

$$\begin{aligned} \boldsymbol{B}_{dress}(\boldsymbol{r}) &= \boldsymbol{B}_{inner}(\boldsymbol{r}) + \boldsymbol{B}_{outer}(\boldsymbol{r}) && (3.52) \\ &= I_{inner}\ \left[\boldsymbol{b}_{inner}(\boldsymbol{r}) + x\,\boldsymbol{b}_{outer}(\boldsymbol{r})\right]\ , && (3.53) \end{aligned}$$

where the geometrical contributions to the field per unit current $\boldsymbol{b}$ are used and the ratio x between outer and inner currents is left variable. The quantity of interest for the estimate has been $\left\langle |\boldsymbol{B}|^2 \right\rangle$ integrated over the surface of the cylindrical shell. Separating the contributions from the two competing sets of coils, and allowing the current ratios to be variable x this becomes

$$\left\langle |\boldsymbol{B}|^2 \right\rangle = I_{inner}^2\ \left[\left\langle |\boldsymbol{b}_{inner}|^2 \right\rangle + x^2\ \left\langle |\boldsymbol{b}_{outer}|^2 \right\rangle + 2\,x\ \langle \boldsymbol{b}_{inner} \cdot \boldsymbol{b}_{outer} \rangle\right]\ . \tag{3.54}$$

To optimize the shielding it is possible to extract the current ratio x from minimization. A constraint on the current is given by the desired field in the region of interest (e.g. $\boldsymbol{r} = 0$) where the field strength is given by

$$B_{dress}(0) = I_{inner}\ \left[b_{inner}(0) + x\,b_{outer}(0)\right]\ , \tag{3.55}$$

where an assumption has been made that, because of symmetry, the directions of the fields produced by the two sets of coils are parallel at the geometric center. The condition on one of the currents is then

$$I_{inner} = \frac{B_{dress}(0)}{b_{inner}(0) + x\,b_{outer}(0)} \tag{3.56}$$

and the minimization of equation 3.54 yields the optimal current ratio

$$x_{opt} = \frac{b_{outer}(0)\left\langle |\boldsymbol{b}_{inner}|^2 \right\rangle - b_{inner}(0)\,\langle \boldsymbol{b}_{inner} \cdot \boldsymbol{b}_{outer} \rangle}{b_{inner}(0)\left\langle |\boldsymbol{b}_{outer}|^2 \right\rangle - b_{outer}(0)\,\langle \boldsymbol{b}_{inner} \cdot \boldsymbol{b}_{outer} \rangle}\,. \tag{3.57}$$

3.3.5 Small scale prototype

A small scale prototype was built to demonstrate the principles of active shielding. The frame of an existing small scale $\cos\theta$ coil, built on a hollow Aluminum cylinder of radius $R_1 = 8.75\,\text{cm}$ and length $56.3\,\text{cm}$, was used as the inner coil. The coil frame accommodates 40 loops of wire, each in a machined groove cut on the outer surface of the cylinder along its length to approximate the $\cos\theta$ current distribution. Each groove has a pair of matching pins sticking out at either end of the cylinder where the wire can be secured. While preserving the $\cos\theta$ current distribution, only $N = 8$ loops were wound on the coil frame for this test, in addition, the length of the loops was reduced to $L_1 = 49.6\,\text{cm}$.

A larger thin Aluminum shell of radius $R_2 = 9.69\,\text{cm}$ was used to support the active shield. The active shield shape was calculated using the stream function of equation 3.35 for the specific angles and lengths of the inner coil's loops and for the given radius of the thin shell. The computed shape of the active shield is qualitatively similar to the shape shown in figures 3.4 and 3.5.

The active shield was constructed by gluing small Copper wires on a piece of poster paper that was tightly wrapped around the Aluminum cylindrical shell. The positions of the wires at all points on the surface of the cylinder were printed on the poster paper by the Caltech Graphic Resources using a wide printer for poster presentations. The specifications were stored in a PDF file with the dimensions adjusted so that the printed output would match the real dimensions of the active shield. The printer method was calibrated by iteratively sending reference geometries via PDF and measuring the output dimensions, adjusting to make sure that the scaling matched.

Figure 3.11 shows a close-up photograph of the finalized coil, wrapped on its supporting cylinder, with $M = 10$ loops of wire wound according to the specified pattern. Figure 3.12 shows the prototype placed inside the small-scale magnetic field mapper.

The final active shield coil consisted of $M = 10$ loops wound as a single continuous coil in such a way that that the short segments of wire bringing currents into and out of each loop were paired up and twisted with each other to partially cancel the field produced by them.

A constant field mapping test of the prototype coils was performed using a single-axis magnetometer mounted on a x-y-z mapper built at the Caltech Kellogg Radiation

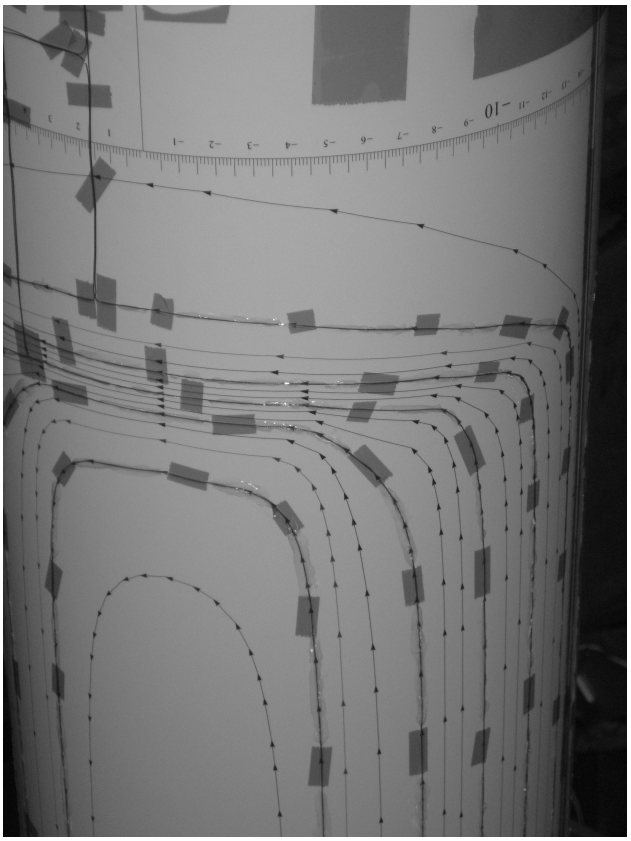

Figure 3.11: Detail photograph of the active shield prototype. The wiring pattern is printed on poster paper according to the optimal solution for a smaller $\cos\theta$ coil (not shown). The printout is cropped ($\sim 60 \times 64\,\mathrm{cm}^2$) and wrapped around an Al cylindrical shell for support. The wires are then glued in position following the pattern. The wires carrying current into the coil (upper left corner) are paired up closely, in order to partially cancel their induced magnetic field.

Laboratory for the mapping of small cylindrical coil prototypes [56]. The inner $\cos\theta$ coil and the outer shield were placed at the center of the mapper with their axes aligned vertically. The coils were connected to two independent power supplies. The current in the inner coil was fixed to $I_1 = 1.5$ A, while the current in the outer shield was varied. Table 3.2 provides a summary of the different current setting of the measurement.

The mapper was programmed to move to different locations inside and outside the coils to measure the principal component of the field, in this case B_y in a coordinate system where z lies along the axes of the coils. At each point, after a settling wait time of a few seconds, the background field B_b was measured with the currents in both coils turned off. The total field was then measured after applying currents to the coils. The mapping routine was repeated following the same pattern of points for several (~ 5) cycles at each

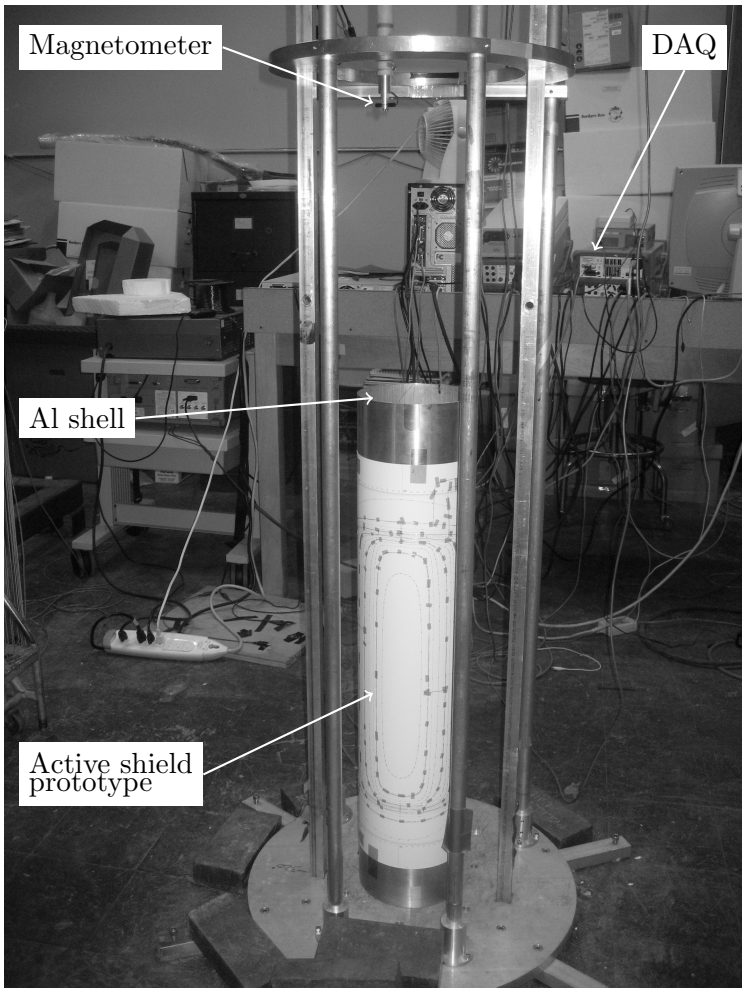

Figure 3.12: Photograph of the active shield prototype installed on its aluminum shell support and placed inside the small-scale field mapper. Not shown is the inner $\cos\theta$ coil which is centered inside the Al shell on a support to raise it, so that the centers of the two coils coincide.

coil current setting.

A numerical model of the dressing coil prototype was used to compare the measured data. Table 3.2 shows the general agreement of the raw data with the model at a single point in the center of the coils, using the nominal currents specified in the measurement in the model. A refined numerical model was also used where a normalization of the currents in the model was allowed so to better match the measured data. A selection of the measurements of the field inside the coil are summarized in figure 3.13, where the principal component of the field B_y is plotted against position along the axes of the coils. The magnetic field uniformity along this axis is dramatically worsened by the operation of the active shield.

I_1 (A)	I_2 (A)	I_2/I_1	$B_y^{meas.}$ (G)	B_y^{model} (G)
1.5	0.0	0.00	$4.551 \cdot 10^{-1}$	$4.575 \cdot 10^{-1}$
1.5	−0.1	−0.07	$4.205 \cdot 10^{-1}$	$4.227 \cdot 10^{-1}$
1.5	−0.2	−0.13	$3.860 \cdot 10^{-1}$	$3.880 \cdot 10^{-1}$
1.5	−0.3	−0.20	$3.515 \cdot 10^{-1}$	$3.532 \cdot 10^{-1}$
1.5	−0.4	−0.27	$3.170 \cdot 10^{-1}$	$3.185 \cdot 10^{-1}$
1.5	−0.6	−0.40	$2.479 \cdot 10^{-1}$	$2.490 \cdot 10^{-1}$
1.5	−0.7	−0.47	$2.133 \cdot 10^{-1}$	$2.143 \cdot 10^{-1}$
1.5	−0.8	−0.53	$1.788 \cdot 10^{-1}$	$1.795 \cdot 10^{-1}$
1.5	−0.9	−0.60	$1.442 \cdot 10^{-1}$	$1.448 \cdot 10^{-1}$
1.5	−1.0	−0.67	$1.097 \cdot 10^{-1}$	$1.100 \cdot 10^{-1}$
1.5	−1.1	−0.73	$7.510 \cdot 10^{-2}$	$7.529 \cdot 10^{-2}$
1.5	−1.2	−0.80	$4.064 \cdot 10^{-2}$	$4.055 \cdot 10^{-2}$
1.5	−1.3	−0.87	$6.014 \cdot 10^{-3}$	$5.805 \cdot 10^{-3}$
1.5	−1.4	−0.93	$-2.845 \cdot 10^{-2}$	$-2.894 \cdot 10^{-2}$

Table 3.2: Summary of mapping data measurements for a prototype of dressing coil with active shield. The values of the measured magnetic field at the center of the coils are compared to the values expected from a numerical model of the coil combination. As the current in the outer active shield coil, I_2, increases in magnitude, magnetic field cancellation occurs. The field at the center vanishes for a current ratio $I_2/I_1 \simeq .878$, and beyond that point the field direction reverses as the outer coil provides more of the field.

Outside the coils, the magnetic field was measured for a sample of points over the surface of an imaginary cylindrical shell of radius $R_{out} = 13$ cm and length $L_{out} = 60$ cm, representing the location of the ferromagnetic shield. The effectiveness of the active shield prototype in reducing the magnetic field was computed from the root mean square measurement of the field outside the coils. The results are shown in figure 3.14 as a function of the ratio I_2/I_1 of outer and inner currents.

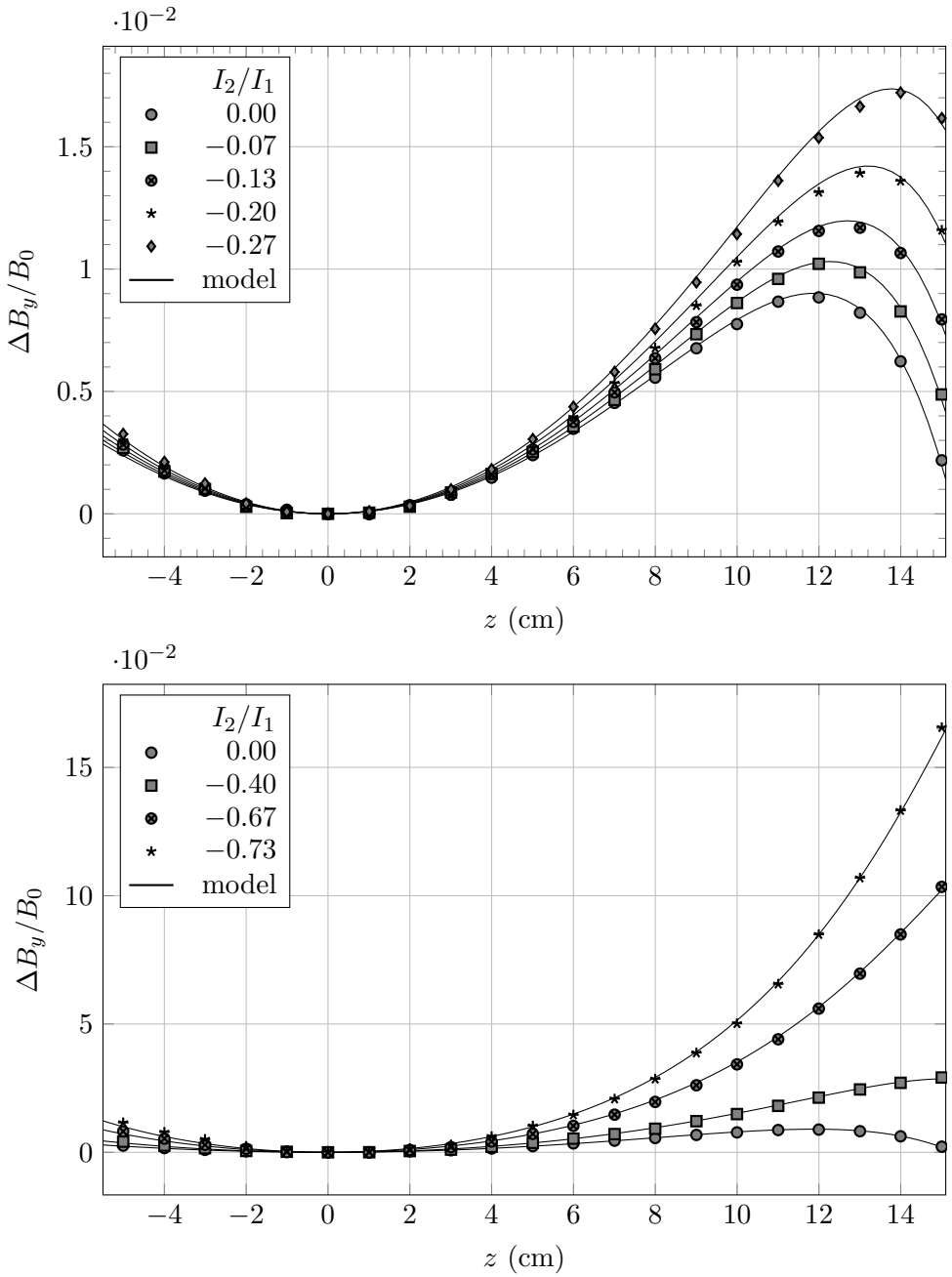

Figure 3.13: Normalized magnetic field profiles of a dressing coil prototype as a function of position along the axes of the coils for different current settings. The data points represent measurements of the principal component of the field, scaled by the value measured at $z = 0$. The model curves are numerical calculations, where a normalization factor in the current was introduced. The magnetic field gradient along the z direction is smallest for the $I_2 = 0$ case for which only the inner $\cos\theta$ coil is active. In the lower figure, the field profile for a current ratio near perfect shielding ($I_2/I_1 \simeq -0.73$) is shown to produce large gradients.

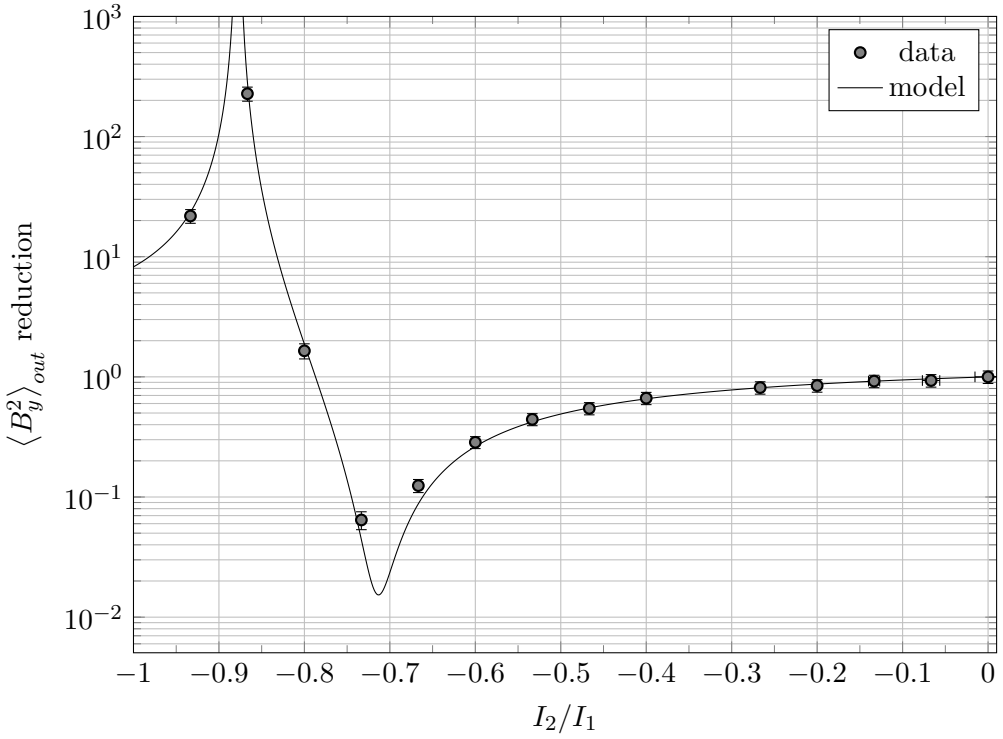

Figure 3.14: Reduction of the magnetic field induced outside the dressing and active shield prototype coils as a function of the ratio of currents in the coils. The data points represent averaging of a sample of measurements of B_y over a cylindrical surface of radius $R_{out} = 13$ cm and length $L_{out} = 60$ cm.

Chapter 4

Establishment of a large Electric field in superfluid Helium

A large electric field is essential for the measurement of the neutron Electric Dipole Moment as it is in the *nEDM* experiment, where the observable shift in precession frequency due to the presence of an EDM would be linear in the applied electric field. For a permanent EDM to be measured with such method, it is necessary to compare the frequency shift of two separate measurements with different field configurations. In one measurement the magnetic and electric fields will be aligned and in the other anti-aligned.

In the *nEDM* experiment two symmetric and opposite electric fields are applied simultaneously to two separate measurement cells. The two cells are sandwiched between three electrodes of rounded rectangular shapes where the outer electrodes are effectively electrically grounded. A voltage difference is established between the middle electrode and the outer electrodes to create the opposing electric fields. The direction of both fields can be inverted by changing the polarity of the voltage of the middle electrode.

4.1 Electrode design for the *nEDM* experiment

4.1.1 Voltage multiplication

The requirements for the *nEDM* measurement define a nominal field $E = 74\,\mathrm{kV}\cdot\mathrm{cm}^{-1}$ [35]. With a gap across a cell $\Delta x = 7.6\,\mathrm{cm}$ and taking into account $\sim 2.5\,\mathrm{cm}$ of cell wall thickness, the required voltage drop across the electrode is expected to be in excess of $700\,\mathrm{kV}$.

The high voltage electrode is contained within a super-fluid He cryostat and it would be very difficult to deliver the high voltage directly to it from outside the cryostat. The high

voltage is instead created inside the cryostat by means of voltage multiplication consisting of a variable parallel plate capacitor. A lower initial voltage $V < 100\,\mathrm{kV}$ can be supplied to the voltage multiplier inside the cryostat via a single commercially-available feed-through. Figure 4.1 shows the schematic drawing of the voltage multiplying apparatus.

The variable capacitor is constructed from two round large parallel plates with diameter no less than 40 cm. The gap between the two plates can be adjusted by moving one plate relative to the other, therefore, controlling the capacitance of the plates. For simplicity, the movable plate is grounded, while the other plate is fixed and electrically connected to the high voltage electrode between the two cells.

The high voltage electrode is electrically insulated from the rest of the conductors so that its voltage can be floating above or below ground voltage. A charging electrode can be physically brought into electrical contact with the high voltage electrode in order to establish an initial voltage. Once charged, the charging electrode can be removed and the floating high voltage conductor will maintain the accumulated charge. Since only the charging electrode is ramped-up to initial high voltage, a single high voltage feed-through path to the inner cryostat is necessary. The other electrodes, on the other hand, are effectively coupled to ground, but can be electrically insulated and grounded outside the cryostat. These require several low voltage feed-throughs which are much smaller and cheaper and are not associated with the breakdown difficulties that high voltage feed-through incur.

The variable capacitor is electrically in parallel with the capacitors consisting of the two cell electrodes. Effectively, the total capacitance of the system is then

$$C_{tot} = C_V + C_F, \tag{4.1}$$

where C_V is the variable capacitance of the movable parallel plate capacitor and C_F is the fixed capacitance of the other electrical conductors inside the cryostat, including the fixed capacitance of the cell electrodes C_{cell} and the capacitative coupling to the grounding cryostat case,

$$C_F = 2\,C_{cell} + C_{other}. \tag{4.2}$$

When the high voltage conductor is ramped up to a voltage V_0 the charge accumulated on it is given by

$$Q_0 = C_{tot}\,V_0. \tag{4.3}$$

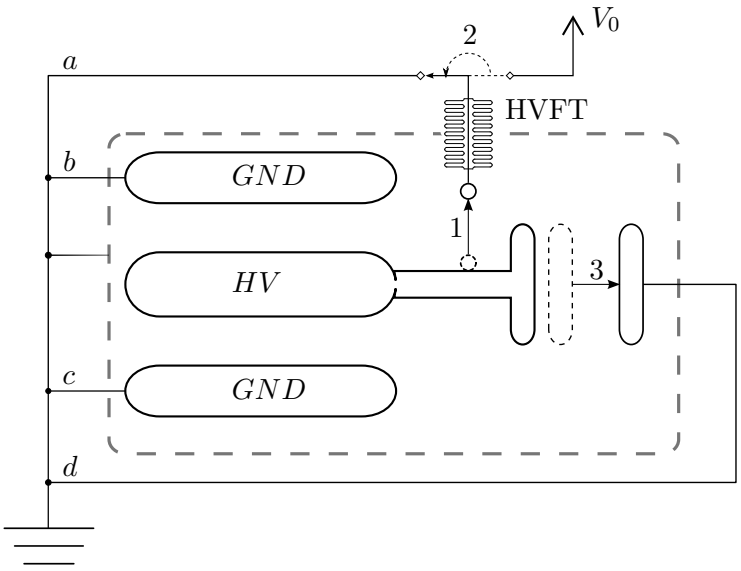

Figure 4.1: Schematic drawing of the voltage multiplying apparatus. The single high voltage feed-through (HVFT) delivers the initial voltage V_0 to the inner high voltage electrode HV through the outer vacuum shell (dashed gray). After ramping-up the voltage, 1.) The connection to HV is physically retracted so that the electrode is now floating and 2.) the high voltage power supply is disconnected from the apparatus. 3.) The variable capacitor plate is retracted to increase the voltage of the HV electrode, thus increasing the electric field between HV and GND electrodes, where the measurement cells are located. The electrical currents flowing to and from electrodes at ground can be measured at a, b, c, d and can provide diagnostic information on the inner voltage during the run.

When the ramp-up is complete, the charging electrode is physically disconnected and the initial charge Q_0 stays on the floating high voltage conductor. It is then possible to modify the voltage of the charged electrode by varying the total capacitance to ground using the variable capacitor. The final voltage will be

$$V' = \frac{Q_0}{C'_{tot}} = \frac{C_V + C_F}{C'_V + C_F} V_0 \tag{4.4}$$

where C'_V is the final capacitance of the variable capacitor. If the final capacitance is less than the initial capacitance, the voltage will have increased, effectively multiplying the initial voltage. The system can be charged when the gap between plates in the variable capacitor is at a practical minimum. After the charging electrode is removed, the variable capacitor plates can be separated to the maximum gap allowed by the geometry of the cryostat in order to get the highest voltage multiplication possible. Since the distance between the cells' electrodes is fixed, the amplification of voltage results in direct amplification of the electric field.

The voltage multiplication process can also be understood by looking at the charge on the high voltage conductor. The initial charge must be distributed on its surface and in particular shared proportionally between the three large capacitors in the system based on their initial capacitances. When the variable capacitor is retracted, the constant charge on the conductor must redistribute itself, and since less charge can be accommodated by the lowered capacitance of the separated plates, more will be distributed, by the capacitative coupling, to the electrodes around the cells, establishing a higher voltage across the cells, and therefore, a larger electric field.

4.2 Voltage Amplification Test

A large scale test of the voltage multiplication process was carried out at the Los Alamos National Laboratory. The measurement involved testing the amplification of voltage by means of in-situ capacitor plates, as well as establish a large Electric field across Stainless steel electrodes in liquid ^{4}He at superfluid temperatures. A previous measurement [57] was performed with Al electrodes using the same apparatus.

The inner cryostat is shown in a model drawing in Figure 4.3 and consists of a large

Stainless steel chamber of cylindrical shape, of diameter of 65 cm and $\sim$ 150 liters in volume, which is filled with liquid ^{4}He at superfluid temperatures. Stainless steel electrodes are located inside this large bath of liquid Helium, so that when the cryostat is full, the electrodes are completely immersed in liquid. The cryostat is, in turn, suspended inside a larger outer vacuum vessel by four Kevlar ropes, to minimize the thermal coupling to external heat sources.

The outer volume contains a thermal shielding Cu shell that surrounds the entire inner cryostat to shield it from external heat loads. During operation, the Helium shield is kept at a temperature below 30 K by actively cooling through a serpentine of Cu tubing carrying cold ^{4}He boil-off gas from an external Dewar. The inner cryostat is protected from radiative heat loads by $\sim$ 30 layers of super-insulation.

On both sides of the cylindrical inner cryostat, and co-axial to it, two sets of bellows allow the actuation of rods, inside the cryostat, that are used to control the position of two electrodes, a charger (CHG) to set up the initial charge on the high voltage (HV) electrode and a ground (GND) electrode that forms a variable capacitor with the HV electrode and is used to test the voltage amplification. The use of bellows, which are filled with liquid Helium, allows actuation of motion without a feedthrough, which would otherwise not allow a superfluid tight cryostat. In addition, the actuation bellows are paired up and the linkage with the actuator rods is done between the bellows pair so that when the electrode is actuated, one bellows contracts while the other expands, allowing the total length of the combination of bellows to be fixed by external support rods, and making it possible for the electrodes to be moved without applying pressure on the liquid and without changing the volume of the liquid Helium container.

4.2.1 Cryogenic cooling

The operation for the high voltage test includes cryogenic considerations for the system to be run while filled with liquid Helium at temperatures below the λ-point. The cooling procedure for the measurement is detailed in what follows.

Once closed, the outer vacuum chamber is evacuated using a turbo-pump. During the cool-down, the inner chamber is kept filled with ^{4}He gas at positive pressure with respect to atmospheric pressure, in order to limit the inflow of extraneous gas in the chamber. In order to check the vacuum seal between the separate inner cryostat chamber and the

outer volume, a Helium leak detector (Pfeiffer Vacuum) is set up to constantly monitor the presence of ^{4}He in the outer volume. Any significant increase of Helium leakage during the cooldown process, which cannot be explained by otherwise routine handling of liquid and gaseous Helium in the room, must be considered as a possible compromise of the inner chamber seal and investigated as such.

Liquid Nitrogen is used to pre-cool, at a controlled rate, both the inner cryostat, through a set of cooling tubing, and Cu heat shields to less than 100 K. The cooling rate is controlled by manually adjusting the flow of cryogenic fluid through the system with feedback from ~ 50 temperature sensors installed inside the cryostat. The liquid Nitrogen can then be replaced by Helium boil-off so that the temperature of the inner cryostat and shields can brought down further. Once cold (< 15 K), the whole inner cryostat chamber can be filled with liquid Helium, while the Cu shield is kept connected to the active cooling with Helium boil-off. After the initial fill, the Helium level in the inner cryostat can quickly drop due to evaporation from residual heat present in the system. The apparatus can be refilled when necessary from liquid supply Dewars.

The temperature of the liquid ^{4}He can be lowered by evaporative cooling using a vacuum booster pump connected to the exhaust of the inner cryostat. In order to lower the temperature of 150 L of liquid ^{4}He from $T \simeq 4$ K (boiling temperature at LANL pressure) to below the superfluid transition and to $T \simeq 2$ K, it is necessary to remove

$$\Delta Q \simeq (5 \times 10^3 \,\mathrm{mol}) \cdot [H(4\,\mathrm{K}) - H(2\,\mathrm{K})] \simeq 1.5 \times 10^5 \,\mathrm{J} \tag{4.5}$$

heat from the bath, with $H(T)$ representing the enthalpy of Helium [58] summarized for interesting values in table 4.1. In order to keep the inner cryostat volume filled with liquid, a constant supply of liquid ^{4}He from external supply Dewar at 4 K must replace the liquid that has evaporated during the cooling. Typically, temperatures of $T \approx 1$ Kelvin can be achieved using evaporative cooling if the external heat load is kept to a minimum.

4.2.2 Electrodes

Inside the inner cryostat, a large central high voltage electrode (HV), round in shape and of diameter $\simeq 45$ cm is suspended in the middle of the cryostat by insulating rods made of G10. This electrode is effectively insulated from the rest of the cryostat and once charged,

T (K)	H (J/mol)
4	35.1
2.17	10.7
2	6.5
1.6	1.6

Table 4.1: Liquid ^{4}He enthalpy at selected temperatures above and below the λ-point [58].

it can be left electrically floating to preserve the charge on it. Figure 4.2 shows a voltage contour of the internal electrodes.

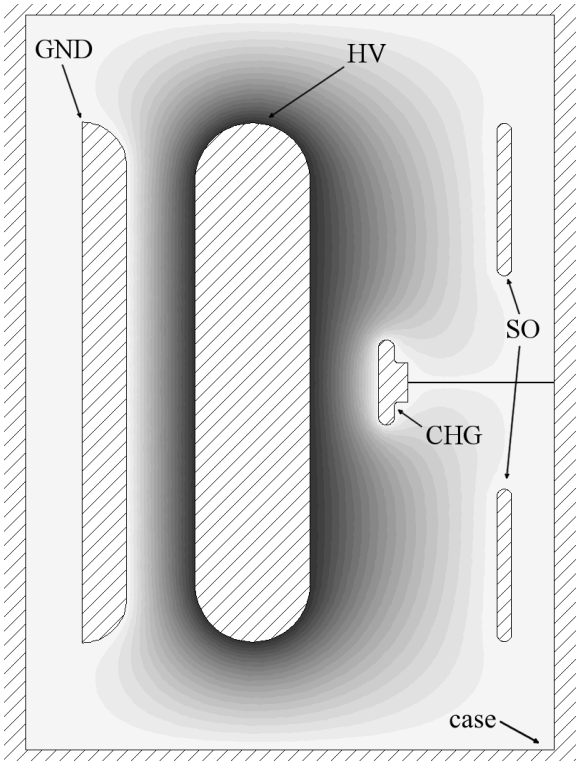

Figure 4.2: Finite element model of large high voltage test internal electrodes, labeled, enclosed in the grounded cryostat case. The contours represent equipotential lines when the *HV* electrode is charged and the *GND* electrode fully retracted.

The charge can be brought to the *HV* electrode from outside the cryostat by means of a small charger (*CHG*) electrode, which can be moved to touch the center of the *HV* electrode and can then be retracted once charged. A compact high voltage feedthrough, capable of reaching the highest voltage provided by the external high voltage power supply of 50 kV, connects the inner *CHG* electrode to the outside of the inner chamber. A second high voltage feedthrough provides the interface between the vacuum chamber and the outside

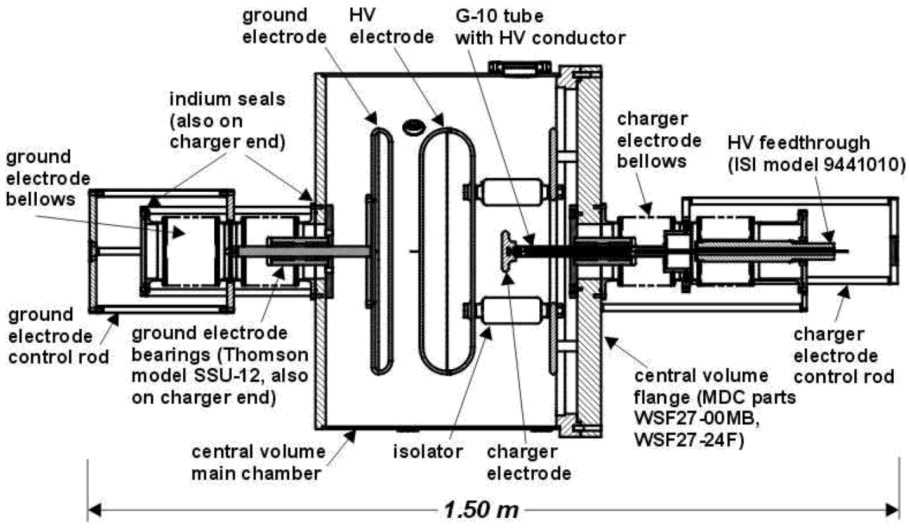

Figure 4.3: To-scale section drawing of HV test apparatus [57]. The large *HV* electrode at the center of the device is suspended by cylindrical insulating rods and is effectively electrically floating. The *GND* and *CHG* electrodes can be moved relative to the fixed *HV* electrode to test the voltage multiplication.

power supply. Once disconnected from the high voltage power supply, the *CHG* electrode can be connected to a picoammeter to measure the flow of current due to amplification.

The ground electrode (*GND*) is about as large in area to the *HV* electrode and is located on the opposite side relative to *CHG*. When the *GND* electrode is moved in close to the fixed *HV* electrode, the capacitance of the two parallel plates is maximized, and decreases as their separation increases. The maximum capacitance that can be expected from a distance between the two plates of 1 mm is on the order of 1-2 nF, while the smallest, achieved at the maximal separation of $\sim$ 6 cm, is about 25 pF.

A fourth stand-off (*SO*) electrode is at a fixed distance from *HV*, on the same side as the *CHG* electrode with *CHG* protruding from a hole in its center. This electrode provides a fixed reference capacitance to measure the effect of voltage multiplication.

4.2.3 Operation

To test the voltage multiplication the *CHG* electrode is first brought into contact with the *HV* electrode. An initial gap of $\sim$ 3 mm between the *HV* and *GND* is established to provide a large initial capacitance $C_0 \sim 400$ pF in the variable capacitor. A high voltage power

supply is then used to ramp up the system to an initial voltage of 15–40 kV, charging *HV*. Subsequently, the *CHG* is quickly retracted to its resting position (6 cm away from *HV*) and the voltage on the power supply ramped down to ground, while the isolated *HV* electrode is floating at a high voltage.

Once charged, the *HV* electrode will maintain its charge so that when the *GND* electrode is slowly retracted to its maximum distance from *HV*, and its capacitance is drastically decreased, the charge will redistribute over the surface of *HV*, shared by the rest of the capacitors in the system, resulting in an amplified voltage difference, described by Equation 4.4.

After a retraction, the *GND* electrode is brought back towards the *HV* electrode, returning to the original starting position and restoring the original capacitance. Since the charge should be conserved on the *HV* electrode, the voltage should also return to its original initial value. After a retraction-return cycle, the system is in its original configuration, allowing additional retraction measurements to be performed on the charged system.

4.2.4 Data Acquisition

The *GND*, *CHG* and *SO* electrodes are isolated from the rest of the inner chamber and effective grounding paths are established through three separate picoammeters located outside of the cryostat that can measure the currents that flow in and out of the electrodes inside the inner cryostat. The equivalent electrical circuit of the setup is shown in Figure 4.4. During voltage ramp-up, current flows from the high voltage power supply into the inner chamber through the feedthrough and out through the picoammeters connected to the *GND* and *SO* electrodes.

During the amplification process, the rearrangement of charge on the *HV* electrode inside the inner chamber can be measured by looking at displacement current flow through the picoammeters. The results of one amplification is shown in Figure 4.7. The capacitance from the *GND* electrode is greatly reduced and the electrode experiences a decrease in charge, so a negative current is measured. Inversely, the other electrodes *CHG* and *SO* experience an increase in charge and so a positive current flows towards them.

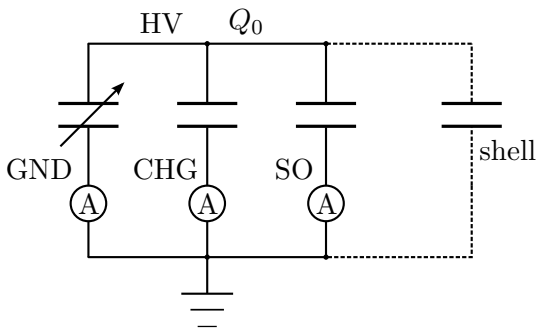

Figure 4.4: Equivalent electrical circuit for the set of internal capacitors in the large scale high voltage test. Three picoammeters measure the currents flowing in and out of the cryostat. Shown as an additional capacitor in dashed line is the effective capacitance of the *HV* electrode with respect to the inner cryostat shell which is effectively grounded, but whose current is not measured. The initial charge Q_0 on the floating *HV* electrode is coupled to the capacitance from the other conductors in the inner cryostat. When the capacitance in the variable capacitor drops, the charge on *HV* must rearrange itself on the remaining capacitors, resulting in a higher voltage.

4.2.5 Finite element model

A finite element model was used to study the expected amplification properties of the high voltage test. The software tool *FEMM* [59] offers solutions for electrostatic problems with simple 2D geometry or rotational symmetry and was used to create the model of the large scale test, as shown in Figure 4.2. From the finite element model it is possible to obtain estimates of the capacitances between electrodes. Table 4.2 summarizes the computed capacitances between the *HV* electrode and other electrodes in the system, and Figure 4.5 shows the relation between the capacitance of the *GND* electrode and the spacing.

Component	C (pF)
HV–GND	390 (3 mm)
	300 (4 mm)
HV–CHG	2.6
HV–SO	6.3
HV–case	25

Table 4.2: Finite element computation of electrode capacitances, including an estimate of the stray capacitative coupling to the conductive cryostat "case".

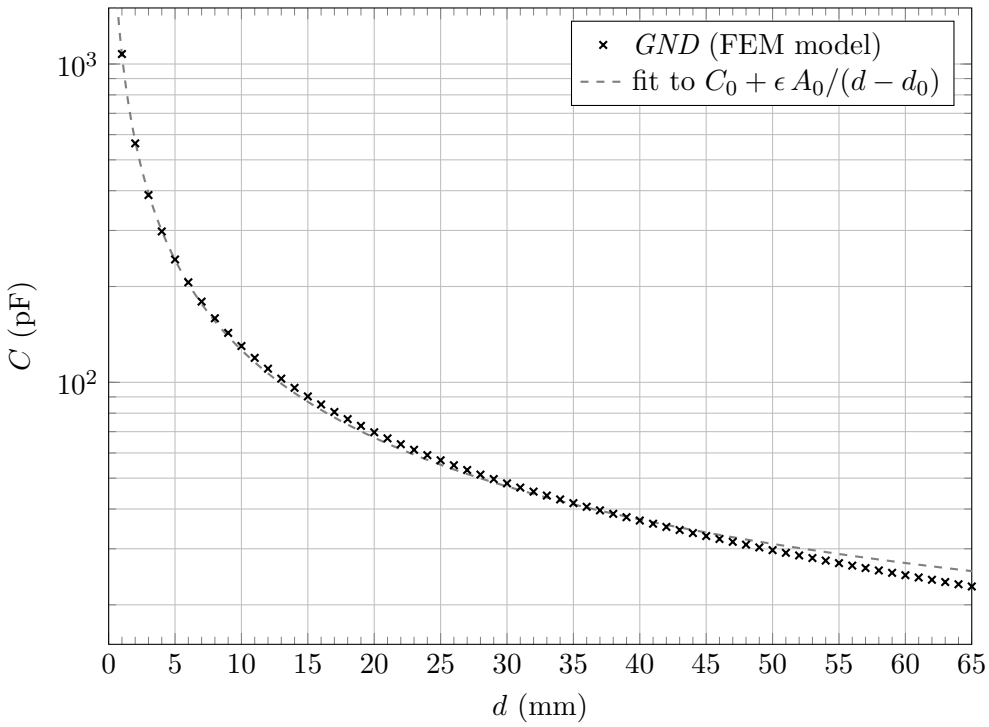

Figure 4.5: Finite element computation of the capacitance of the *GND* electrode with respect to *HV*, as a function of electrode spacing d. Fit to the function $f(d) = C_0 + \epsilon\, A_0/(d - d_0)$, with parameters $C_0 \simeq 6.9\,\text{pF}$, $A_0 \simeq 1{,}367\,\text{cm}^2$, $d_0 \simeq -0.14\,\text{mm}$, are displayed to show agreement with $1/d$ behavior for small d.

4.2.6 Calibration

In order to estimate a value for the amplified voltage, the measured change in charge can be used if one of the fixed capacitances is known. While the finite element model provides a useful comparison of what the capacitances of the system are, it is possible to estimate one of the capacitances from the current drawn during the ramp-up of voltage.

In this configuration, *CHG* is in physical contact with the *HV* electrode and high voltage is supplied to the system from the external power supply. The voltage is ramped-up slowly (< 1 kV/s) and smoothly as allowed by the manual operation of the voltage control. During the ramp-up, a small displacement current flows into the system through the high voltage feedthrough, and out through the capacitative coupling of the *GND* and *SO* electrodes.

The capacitance of the *SO* electrode with respect to *HV* is estimated from the linear relationship

$$Q_{SO}(t) \sim C_{SO}\, V(t) \tag{4.6}$$

between the applied voltage $V(t)$ and the accumulated charge $Q_{SO}(t)$ on the *SO* electrode. The charge can be roughly estimated from the integral of the current measured by the picoammeter

$$Q_{SO}(t) = \int \mathrm{d}t\, I_{SO}(t). \tag{4.7}$$

Figure 4.6 shows a sample of calibration data from the ramp-up of voltage. The capacitance of the *SO* electrode is estimated to be

$$C_{SO} \simeq 5.8(1)\,\mathrm{pF}. \tag{4.8}$$

4.2.7 Amplification

The voltage gain from the amplification process can be calculated from the current measured during the amplification. The *GND* electrode is retracted at a constant speed of $v_{GND} \simeq 1.7$ mm/s away from the *HV* electrode by use of an electric linear motion system. The speed of retraction is fixed by the rotational velocity (20 RPM) of the electric motor, connected to a screw guide of 1/5" per rotation to transform rotational to linear motion. From the velocity and time information of the current measurement, it is possible to know the distance

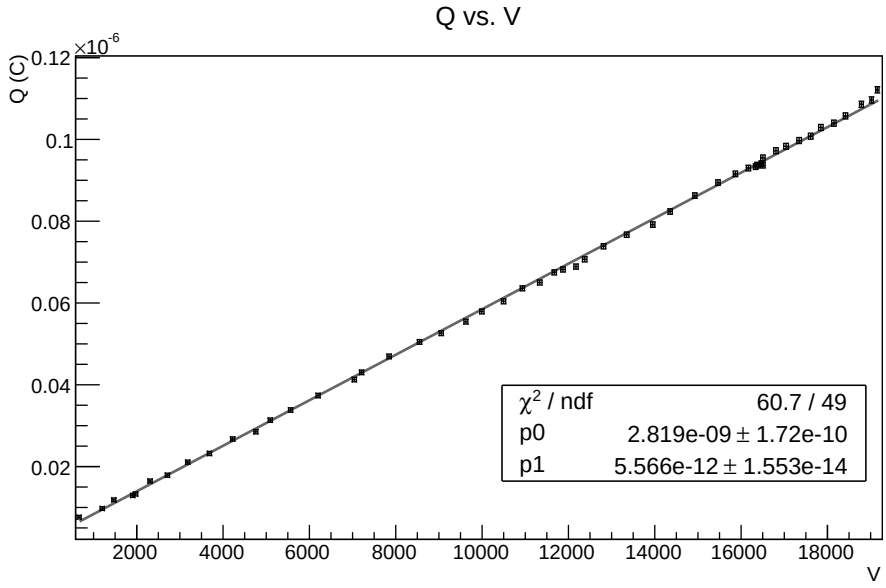

Figure 4.6: Calibration data during voltage ramp-up is used to compute the capacitance of the *SO* electrode.

between the electrodes

$$d = d_0 + v_{GND} \cdot t \tag{4.9}$$

where d_0 is the initial gap, usually of 3 mm, between *HV* and *GND* electrodes. The retraction time for a gap of $d_0 = 3$ mm is $\Delta t \simeq 34$ s.

The amplified voltage can be calculated as a function of the integrated measured current scaled by the reference *SO* electrode capacitance C_{SO}

$$V(t) = V_0 + \frac{1}{C_{SO}} \int_0^t \mathrm{d}t\, I_{SO}(t) \tag{4.10}$$

where V_0 is the initial voltage applied to the *HV* electrode from the high voltage power supply and the integral of the current is taken over the time interval from the beginning to the end of the retraction stroke. The amplified voltage can be mapped to the electrode separation so that it can be compared to the expected amplification characteristics of the system.

Figure 4.9 shows measurements of voltage amplification obtained from the measurement of displacement current during the retraction of the *GND* electrode.

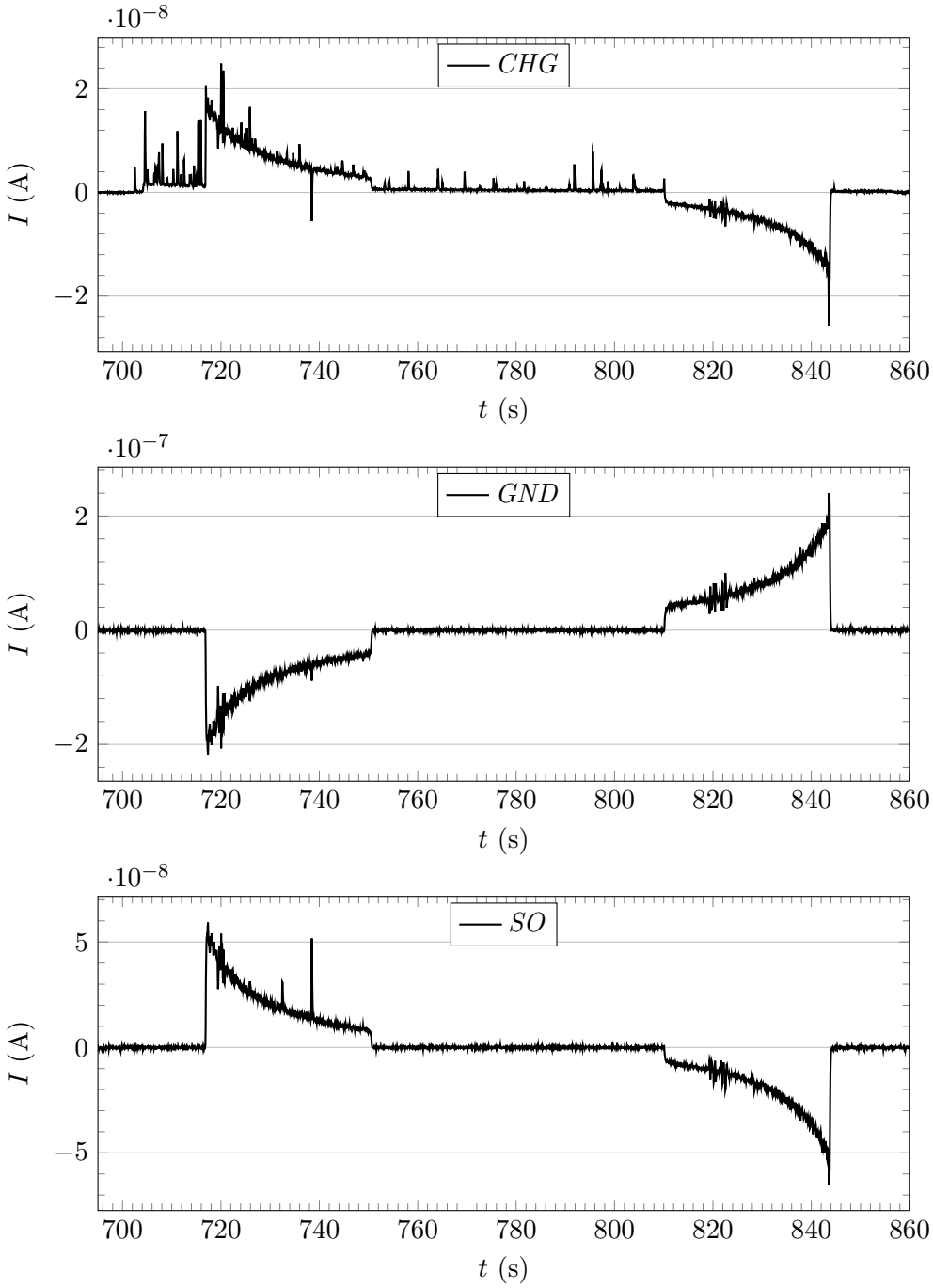

Figure 4.7: Plot of currents flowing in and out of the inner chamber during a retraction (first feature), in which the *GND* electrode is moved away from the charged *HV*, and return of the *GND* electrode to its original position (second feature). Reference time is relative to the start of the measurement, which includes voltage ramp-up of *HV* and disconnection from power supply.

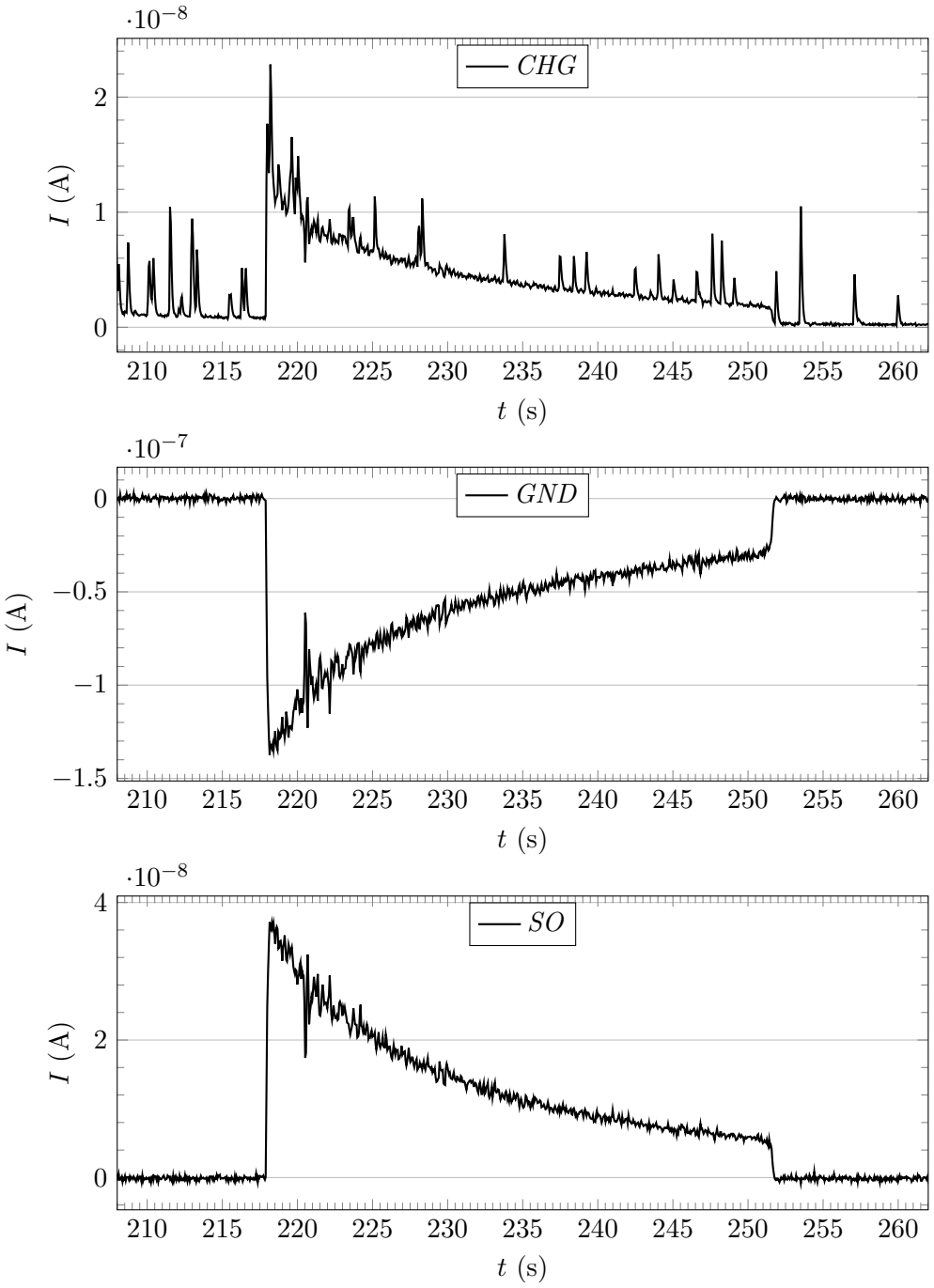

Figure 4.8: Detailed current plot during voltage amplification. The largest contribution to the current flowing in and out of the electrodes system is the current from the *GND* electrode, since its initial capacitance is the largest. An initial voltage of $V_0 \simeq 19$ kV was applied from the high voltage power supply.

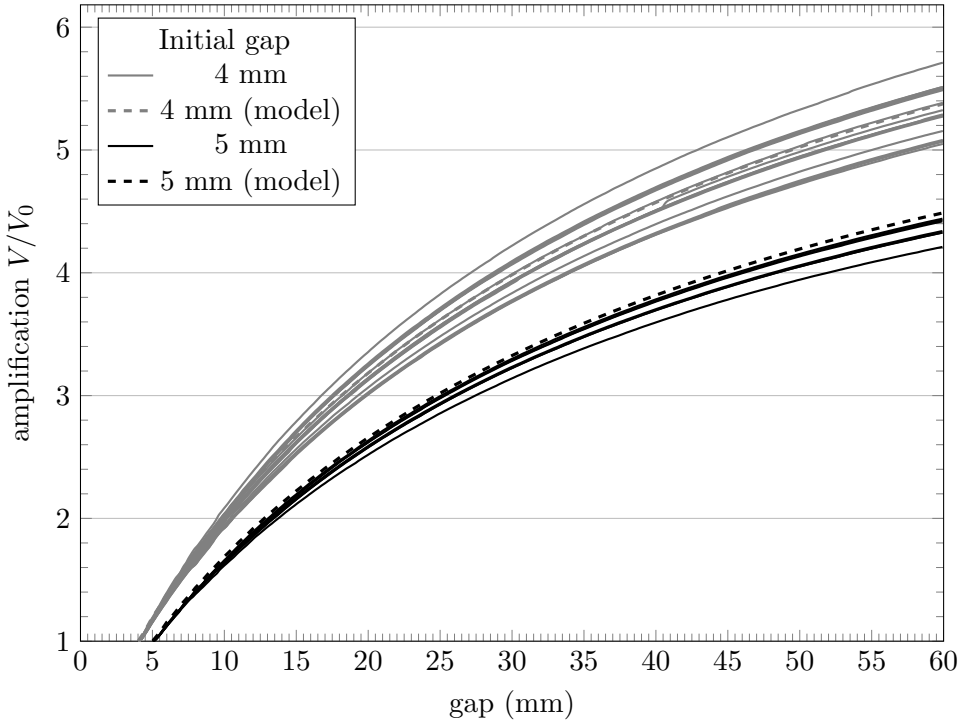

Figure 4.9: Plot of voltage amplification as measured from charge displacement during retraction of *GND* electrode. Relative multiplication factor as a function of *GND* and *HV* electrode distance d. Each solid curve represents a measurement of voltage amplification. Different initial gaps result in different achievable amplifications at the maximum gap extension. Also shown are the expected voltage amplification curves from the *FEMM* finite element model.

4.2.8 Electrical breakdown in superfluid Helium

The large scale high voltage test was carried out with the intention of measuring the breakdown voltage of the stainless steel electrodes over a large volume of superfluid Helium. The requirements of the *nEDM* experiment [35] necessitate a strict limit on the probability of a breakdown for the entire duration of the experiment. Because of this, the voltage applied to the electrodes during the measurement must be significantly lower than the maximum voltage that the dielectric can sustain. The dielectric in question is liquid ^{4}He in its superfluid state, at an operating temperature designed to be near 0.4 K. Given the geometry and complexity of the components of the high voltage system, it is expected that the field across the cells will not be the maximum electric field sustained across the liquid. For instance, the electrodes are designed to bulge out and enclose the cells in such a way that the spacing between the two electrodes is smallest outside the cells, so that for a given voltage, the field will be higher just outside the cell. Since the nominal value of the electric field in the cells is $E \simeq 74\,\mathrm{kV \cdot cm^{-1}}$, it can signify that breakdown should occur only for fields in excess of $100\,\mathrm{kV \cdot cm^{-1}}$.

Breakdown in liquids is not well understood, at least not to the level that breakdown in a gaseous medium occurs [60]. This is probably due to complications arising from phase transitions between liquid and gas, and the fact that electrical currents tend to increase the temperature due to resistive heating, leading to phase transitions for liquids, but not for gases. The study of breakdown in Helium is of interest because of its cryogenic properties and its inert chemical properties. One application is as an electrical insulator and cooling agent for superconducting coils. The study of gaseous Helium gas at low temperatures and varying pressures has been carried out extensively [61–63]. The breakdown in gaseous Helium is understood to originate from known Townsend processes in which electron and ion avalanches are sustained by the ionization of neutral atoms creating a conductive path between the electrodes. The breakdown of Helium at low densities seems to agree well with Paschen's law for sustainability of an avalanche [62], so that the breakdown voltage increases if the density is increased.

The breakdown in liquid Helium has been attributed [63–65] to the presence of bubbles in the bulk, where electrons can localize and possibly acquire enough energy from the electric field to ionize another atom and initiate an avalanche process. Due to the low heat

of vaporization of Helium ($L_{vap} \approx 80 - 90\,\mathrm{J} \cdot \mathrm{mol}^{-1}$ [58]), bubble formation is prominent in liquid Helium, while suppressed in other liquids. The study of breakdown in the liquid is then a study of the processes of nucleation of bubbles which is due to the interface between the electrode and the liquid.

One aspect that is evident in the literature [61, 66], is the fact that impurities in the Helium in gaseous form greatly affect the breakdown strength. This can be a concern for the liquid case too, where impurities can freeze out on the surface of the electrode and change the breakdown strength of the interface between liquid and conductor. This was also noticed in the large scale test conducted at LANL, where the breakdown strength in liquid Helium was significantly affected when an accidental large contamination of the inner cryogenic vessel introduced air in the system so that snow was visible from the windows.

The limited set of breakdown data collected during the runs on the large scale test at LANL is summarized in Figure 4.10 for both the normal and superfluid phases of liquid Helium [67]. The data points collected represent the maximum electric field that could be sustained without a breakdown observed in a period of time on the order of a minute. Qualitatively, the data show that in the normal phase breakdown is seriously affected by the active pumping of the Helium liquid. This can be explained from the presence of boiling in the liquid which generally decreases the density of the liquid, but also allows for paths in gas to form because of the bubbles. The transition to superfluid does not seem to adversely affect the breakdown capabilities. In the superfluid regime, the bubble formation due to boiling is suppressed due to the large heat conductivity, so pumping on the liquid Helium does not reduce the breakdown strength in a significant way. The breakdown strength seems to depend on the pressure of the liquid, but not directly on its temperature, or its phase. A single data point away from thermal equilibrium was obtained by sealing off the cryostat containing the superfluid Helium and letting the pressure build up. The increase in pressure did not change the temperature of the Helium bath significantly and the breakdown strength was noticeably improved.

The range of temperatures and pressures for which the large scale test was performed was limited by the capabilities of the system. A lot of effort was expended in reducing the heat load to the large cryostat so that temperatures near a Kelvin could be reached. The largest sources of heat were recognized to come from the top of the cryostat, where the inlet and outlet ports were located, so that the design of the cryostat could not be easily

modified. In addition, no convenient way existed to pressurize the Helium bath without increasing its temperature or risking to burst one of the many safety relief valves of the cryostat.

A new measurement of the breakdown in superfluid Helium is underway at LANL. A smaller "medium scale" cryostat is used, designed specifically for superfluid temperatures. A smaller set (≈ 10 cm diameter) of electrodes are fixed in place and separated by $d \approx 1-2$ cm. The electrodes are individually powered by a pair of high voltage power supplies of opposite polarities, so that fields near $E \approx 100\,\mathrm{kV}\cdot\mathrm{cm}^{-1}$ can be tested without the need of voltage amplification. A ^{3}He evaporative refrigerator is used to cool the liquid Helium in the cryostat to temperatures of below 1 K. The new cryostat has been demonstrated to work at temperatures $T \approx 500$ mK [68]. In addition, the volume enclosing the Helium bath is cooled through a metal interface, so that it can be separately pressurized while being actively cooled. The breakdown measurements obtained with this new device should bring results that are relevant to the *nEDM* experiment.

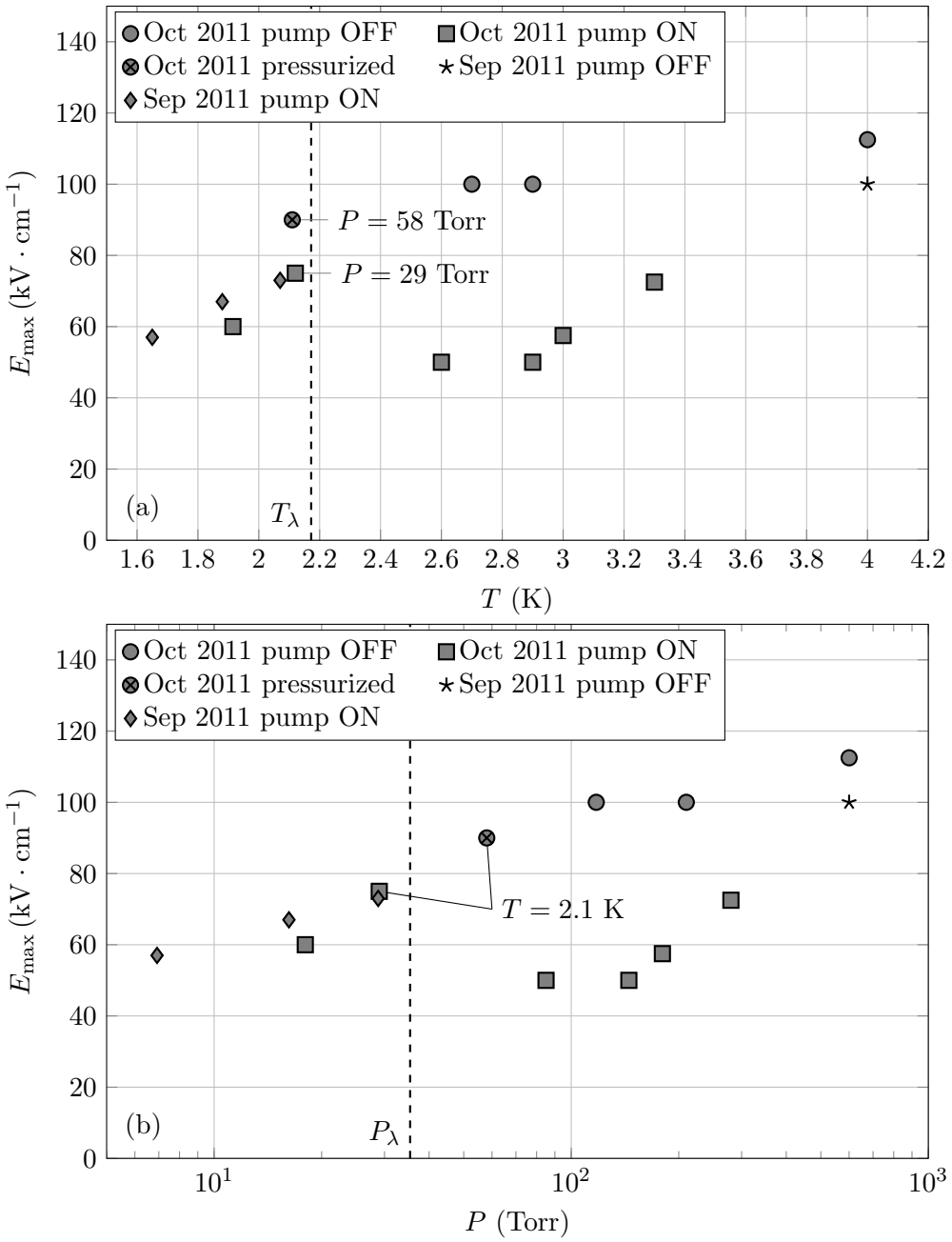

Figure 4.10: Electrical breakdown measurements for the large high voltage test setup at LANL. The data are plotted as a function of the bath temperature (a), as well as the pressure (b). The breakdown tests were conducted at different temperatures of the liquid helium bath, with a gap between electrodes of $d = 4$ mm. One pressurized data point was obtained by valving off the inner cryostat and letting the pressure build up.

Chapter 5

Systematic studies using Monte Carlo spin simulations

As the search for an EDM of the neutron reaches higher sensitivities, the study of systematic effects in the planned measurement becomes more important and necessary for the realization of the *nEDM* experiment. In order to study the effects that are expected in the measurement, a Monte Carlo simulation package was created to study interactions of spins with magnetic fields and electric fields.

5.1 Simulations

Simulations of spin interaction with magnetic and electric fields have been implemented for the geometry planned in the *nEDM* experiment. This includes the study of ultracold neutrons and their spin as they move inside the measurement cell as well as of ^{3}He atoms, which experience similar fields, but can behave differently because of their different velocities and interactions.

The Monte Carlo simulations focus on the study of the interactions with fields appropriately chosen to study certain systematic effects that can arise from magnetic field inhomogeneities and interaction with the electric field. Magnetic and electric fields which resemble the expected experimental parameters have been studied in order to validate the assumptions that the systematic effects were either small or well understood, or else suggest a different approach in the choice of the experimental design parameters.

5.1.1 Numerical Approach

The Monte Carlo simulations are carried out by tracking the classical motion of the magnetic moment vector of a particle with spin, which is aligned to its angular momentum, in the presence of an external magnetic field. The magnetic energy of a particle possessing a magnetic dipole moment μ in an external magnetic field B is [31]

$$\boldsymbol{U} = -\mu \frac{\boldsymbol{J} \cdot \boldsymbol{B}}{J} = -J\,\hbar\,\gamma\,\boldsymbol{\sigma} \cdot \boldsymbol{B} \tag{5.1}$$

where the vector $\boldsymbol{\sigma} = \boldsymbol{J}/J$ is the normalized spin vector and γ the gyromagnetic ratio. Under the influence of a magnetic field, a torque tends to align the magnetic moment vector to the field as to minimize the energy, but because of the intrinsic angular momentum of the particle, the effective torque makes the spin precess about the axis of the field. The basic equation of motion for the magnetic dipole is, then given by the Bloch equation [69]

$$\dot{\boldsymbol{\sigma}} = \gamma\,\boldsymbol{\sigma} \times \boldsymbol{B}. \tag{5.2}$$

Particular solutions exist for the Bloch equation that deal with spins precessing in simple constant fields as well as rotating fields. In the case of the constant magnetic field, it is possible to solve the Bloch equation of 5.2 by differentiating it over time, while assuming $\partial B/\partial t = 0$, so that

$$\ddot{\boldsymbol{\sigma}} = \gamma\,\dot{\boldsymbol{\sigma}} \times \boldsymbol{B} = \gamma^2\ (\boldsymbol{\sigma} \times \boldsymbol{B}) \times \boldsymbol{B} \tag{5.3}$$

$$= \gamma^2 \left[(\boldsymbol{\sigma} \cdot \boldsymbol{B})\ \boldsymbol{B} - B^2\,\boldsymbol{\sigma} \right], \tag{5.4}$$

where the quantity B is the magnitude of the constant magnetic field. The quantity $\boldsymbol{\sigma} \cdot \boldsymbol{B}$ does not change in time and can be considered the inhomogeneous part of the ODE. A set of homogeneous and inhomogeneous solutions can be found for $\boldsymbol{\sigma}$ so that

$$\boldsymbol{\sigma} = \boldsymbol{\alpha}\ e^{i\,\gamma\,B\,t} + \boldsymbol{\beta}\ e^{-i\gamma\,B\,t} + \frac{(\boldsymbol{\sigma_0} \cdot \boldsymbol{B})\ \boldsymbol{B}}{B^2}, \tag{5.5}$$

where the values for $\boldsymbol{\alpha}$ and $\boldsymbol{\beta}$ can be solved using the boundary values at time $t = 0$

$$\boldsymbol{\sigma_0} \equiv \boldsymbol{\sigma}(0) \qquad \text{and} \qquad \dot{\boldsymbol{\sigma}}(0) = \gamma\,\boldsymbol{\sigma_0} \times \boldsymbol{B}\,, \tag{5.6}$$

leading to trigonometric solutions. The final form of the equations of motion are

$$\boldsymbol{\sigma}(t) = \left[\boldsymbol{\sigma_0} - \frac{(\boldsymbol{\sigma_0}\cdot\boldsymbol{B})\ \boldsymbol{B}}{B^2}\right]\ \cos(\omega\, t) - \frac{\boldsymbol{\sigma_0}\times\boldsymbol{B}}{B}\ \sin(\omega\, t) + \frac{(\boldsymbol{\sigma_0}\cdot\boldsymbol{B})\ \boldsymbol{B}}{B^2}, \tag{5.7}$$

where the frequency of spin precession $\omega = -\gamma\, B$ has been substituted, and the sign convention has been chosen so that the rotation vector that describes the precession of the spin vector is simply

$$\boldsymbol{\omega} = -\gamma\, \boldsymbol{B}\,. \tag{5.8}$$

It is useful to note that for small intervals in time, changes to the spin vector, as described by equation 5.7 can be approximated to be

$$\boldsymbol{\Delta\sigma} \simeq \gamma\ \boldsymbol{\sigma_0}\times\boldsymbol{B}\ \Delta t - \frac{\gamma^2}{2}\ \left[\boldsymbol{\sigma_0} - \frac{(\boldsymbol{\sigma_0}\cdot\boldsymbol{B})\ \boldsymbol{B}}{B^2}\right]\ \Delta t^2. \tag{5.9}$$

This second order correction can improve the convergence of numerical methods used to compute spin precession.

Another field configuration, for which a solution to the Bloch equation can be easily found [70] is the case of a field B_{rot} that is rotating with some frequency ω_{rot} in a plane that is perpendicular to the static field B_0. If B_0 points along the x axis, the expression for the total magnetic field is

$$\boldsymbol{B}(t) = B_0\,\hat{x} + B_{rot}\ \cos\omega_{rot}\,t\,\hat{y} + B_{rot}\ \sin\omega_{rot}\,t\,\hat{z}\,. \tag{5.10}$$

A transformation to a rotating frame, where the rotation is about B_0 and the frequency of rotation matches ω_{rot}, will result in the rotating field to appear stationary corresponding to the introduction of a pseudo-field along the direction of rotation, so that the total field is now

$$\boldsymbol{B'} = \left(B_0 + \frac{\omega_{rot}}{\gamma}\right)\,\hat{x} + B_{rot}\,\hat{y}\,. \tag{5.11}$$

The solution of equation 5.7 can then be used to compute the precession of the spin vector about B' in the rotating frame, which can then be translated to the non-rotating frame.

5.2 Modeling of particle motion in the cells

The systematic effects associated with the measurement of spin precession in external magnetic fields depend on the motion of particles in those fields, so the modeling of particle motion and interactions in the measurement cell is an important aspect of the Monte Carlo simulation.

Particles that are trapped in the measurement cell stay in the cell by reflecting on the inner surface of its walls. A bouncing particle exchanges linear momentum with a boundary wall, where the minimum momentum exchange to remain inside the cell is given by the component of the particle's momentum normal to the wall before the collision. In the case of a specular reflection, the component of the incoming momentum normal to the wall changes sign, so that

$$\Delta \boldsymbol{p}_{\text{min}} = -\left(\hat{\boldsymbol{n}} \cdot \boldsymbol{p}\right) \hat{\boldsymbol{n}} \tag{5.12}$$

$$\Delta \boldsymbol{p}_{\text{specular}} = -\,2(\hat{\boldsymbol{n}} \cdot \boldsymbol{p})\, \hat{\boldsymbol{n}}, \tag{5.13}$$

where $\hat{\boldsymbol{n}}$ is the unit vector normal to the surface.

Diffuse reflections of particles from the walls are implemented in the Monte Carlo simulation following considerations of general equilibrium conditions [30, 71, 72]. In equilibrium conditions, and in absence of external forces such as gravity, the density of the phase space of the particles in the cell is expected to be uniform and interactions with the walls should preserve that uniformity. In order to correctly simulate wall reflections, a suitable distribution must be chosen that maps the outgoing momentum to the incoming one and that preserves the density of states.

The outgoing direction cannot be chosen from a simple uniform half-spherical distribution over $\Omega = 2\pi$ because the resulting density of states would not be uniform. In principle, this is because particles that have paths with steep impact angles to the wall (i.e. large component of velocity normal to the wall) will reach the wall faster than their counterparts. Since all output solid angles would be as likely, this results in the loss of steep impact angle particles being higher than the production through the diffuse process.

In general, diffuse reflections should require the flux of momentum incoming to the surface of the wall to equal the outgoing flux of momentum to keep the phase space density

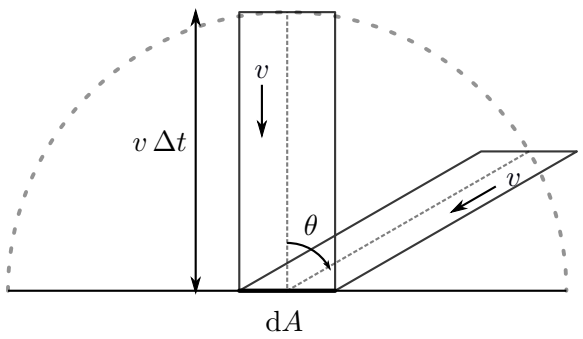

Figure 5.1: Phase space considerations for diffuse bouncing. The number of particles of fixed velocity v that are incident on the area $\mathrm{d}A$ in time Δt and from angle θ will be proportional to the volume $\mathrm{d}V = \mathrm{d}A\,\cos\theta$. In addition, the flux of momentum through the same area is proportional to $\boldsymbol{v}\cdot\mathbf{d}\boldsymbol{A} = v\,\mathrm{d}A\,\cos\theta$.

uniform. This condition is already met for specular reflections, where the normal component of momentum is inverted. A simple implementation of diffuse reflection where the outgoing momentum of a specular reflection is rotated a random angle $\phi \in [0,\, 2\pi]$ about the normal $\hat{\boldsymbol{n}}$ to the surface, will also preserve the phase space because of the azimuthal symmetry of the reflection.

Diffuse wall reflections are implemented in this work so that the direction of momentum of the particle after reflection is not correlated to the incoming direction. The particle direction after diffuse reflection is picked from a distribution [72]

$$f(\theta,\,\phi) \propto \cos^2\theta\;\mathrm{d}\Omega = \sin\theta\cos^2\theta\;\mathrm{d}\theta\,\mathrm{d}\phi \tag{5.14}$$

with angles θ and ϕ as "normal" spherical angles with respect to the normal to the wall so that the outgoing flux of particle momentum equals, on average, the incoming flux. This is because the density of phase space is assumed to be constant, so that the flux of momentum through an infinitesimal area $\mathrm{d}A$ varies as $\cos^2\theta$ as shown in Figure 5.1.

The outgoing angle θ can then be chosen from Equation 5.14, properly normalized so that the total probability is unity as

$$\frac{3}{2\pi}\int_0^{2\pi}\mathrm{d}\phi\int_0^{\frac{\pi}{2}}\mathrm{d}\theta\sin\theta\cos^2\theta = 1. \tag{5.15}$$

Using uniformly distributed random numbers $y \in [0,\, 1]$, this can be accomplished noting

that

$$y = 3 \int_0^{\theta} \mathrm{d}\theta' \, \sin\theta' \cos^2\theta' \tag{5.16}$$

$$= 1 - \left(\cos^{-1}\theta\right)^3, \tag{5.17}$$

so that the angle θ can be picked as $\theta = \cos^{-1}\left[(1-y)^{1/3}\right]$. The azimuthal angle ϕ is chosen from a uniform distribution in 2π.

5.2.1 Ultracold Neutrons

Ultracold Neutrons in the *nEDM* cell have been simulated to travel ballistically and reflect from the cell's walls without loss of kinetic energy. The UCN do not interact with other UCN or other particles in the cell, so each neutron can be simulated independently. Wall reflections are implemented with some fixed probability of diffuse reflection per bounce.

The velocity spectrum of UCN produced by the super-thermal collisions with phonons in the liquid Helium is expected to follow a power function so that

$$f(v) \propto v^k, \tag{5.18}$$

where $k \simeq 2$, with maximal trapped velocities given by the Fermi potential of the holding cell. The initial spatial distribution of the UCN is assumed to be uniform at the beginning of the simulation, as that is the moment after the UCN fill time during which UCN are produced via downscattering from a cold neutron beam. Because of their small velocity and non-interaction, only gravity affects the velocity of UCN within the cell, so that the distribution along the y axis, aligned with gravity, becomes skewed, with a higher density of particles towards the bottom of the cell.

Although UCN are trapped inside the cell by the Fermi potential V_F which allows neutrons with velocities of a few $\mathrm{m} \cdot \mathrm{s}^{-1}$ to reflect from the walls and neutrons with greater speeds to escape, the interaction is not modeled in the Monte Carlo simulation of this work, and the walls are assumed to be impenetrable. Future studies could address the effects of velocity dependence of neutron losses. Most of the systematic effects discussed in this chapter depend on the neutron velocity inside the cell, so a trap lifetime that is velocity dependent could result in the systematic effects changing with time.

The neutron lifetime τ_n is an important limiting factor in the measurement of UCN properties. The measurement cycle is, in fact, designed to maximize the sensitivity to shifts in frequency, by choosing a measurement time adapted [35] to the lifetime of the neutrons in the cell, which depends on the measurement geometry and material properties of the cells, the neutron lifetime and the capture process on ^{3}He. The Monte Carlo simulations of this work do not include physical lifetimes, since the neutron lifetime would not be a primary contributor to the systematic effects sought in this work. On the contrary, the simulations focus only on UCN that are inside the measurement cell for the entire simulation period.

5.2.2 ^{3}He atoms

Atoms of ^{3}He, in trace amounts, diffuse in a super-fluid ^{4}He bath at temperatures well below 1 K. The velocity spectrum of the ^{3}He atoms is given by the Maxwell-Boltzmann velocity distribution function in the form

$$f(v) = \frac{4}{\sqrt{\pi}\, v_{mp}^3}\, v^2\, e^{-v^2/v_{mp}^2}\, \mathrm{d}v, \tag{5.19}$$

where v_{mp} is the most probable speed, given by

$$v_{mp} = \sqrt{\frac{2\, k_B\, T}{M_\star}}, \tag{5.20}$$

where the effective mass of ^{3}He diffusing in liquid Helium $M_\star \simeq 2.2\, M_3$ was used [73].

In this regime, the phonon number density in the bulk of the ^{4}He bath drops rapidly with lower temperature and ^{3}He atoms can then travel ballistically for long periods of time before scattering with phonons. The fractional density of ^{3}He is low enough, on the order of 10^{-10}, so that collisions between ^{3}He atoms are negligible. The mass diffusion coefficient for ^{3}He atoms in a superfluid ^{4}He bath was measured to be [74]

$$D = \frac{(1.6 \pm 0.2)\, \mathrm{cm}^2\, \mathrm{s}^{-1}}{[T(\mathrm{K})]^7}. \tag{5.21}$$

The velocity of ^{3}He atoms is also small enough so that the probability of scattering with phonons in the bulk does not depend on the instantaneous velocity of a single ^{3}He atom [75]. Rather, the mean time between phonon scattering is defined in terms of the root mean

velocity at temperature T

$$v_{rms} = \sqrt{< v^2 >} \tag{5.22}$$

$$= \sqrt{\frac{3\, k_B\, T}{M_\star}} = \sqrt{\frac{3}{2}}\, v_{mp} \tag{5.23}$$

as

$$\tau_p = \frac{3D}{v_{rms}^2}. \tag{5.24}$$

Because of the dramatic temperature dependence of D in Equation 5.21, the mean free path of a ^{3}He atom in bulk liquid, if defined as

$$\bar{\lambda_p} = \bar{v}\, \tau_p \tag{5.25}$$

with the mean speed $\bar{v} = < v > = 2\, v_{mp}/\sqrt{(\pi)}$, can be orders of magnitude different with a temperature change of 100 mK. Table 5.1 summarizes some useful properties of ^{3}He diffusion at temperatures below 1 K. For Helium temperatures ∼300 mK, the mean free path of ^{3}He atoms becomes comparable to the size of the storage volume, so that two temperature regimes exist. Below 300 mK the ^{3}He atoms travel essentially ballistically, constrained by the walls of the cell, while at temperatures above 300 mK, the mean free path can be very short compared to the characteristic length of the cell, so that ^{3}He atoms spend a long time scattering in the bulk liquid and seldom reach the walls. A characteristic diffusion time for the particle to reach a distance R can be defined [76] to be

$$\tau_D = \frac{R^2}{D} = \frac{3\, R^2}{\tau_c\, v_{rms}^2}\,, \tag{5.26}$$

where the mean collision time τ_c is used in order to take into account diffuse collisions with the walls in addition to scattering from excitations in the liquid. The effective mean collision time can be estimated from a combination of the mean time between wall collisions τ_w and the mean time between scattering from excitations τ_p. The effective mean time between collisions is then

$$\frac{1}{\tau_c} = \frac{1}{\tau_p} + \frac{1}{\tau_w}\,, \tag{5.27}$$

From kinetic theory arguments, the mean time between wall collisions can be estimated from

the frequency of collision on the inner surface of the cell. Assuming a uniform distribution of phase space for a mono-energetic particle of velocity v moving in a volume V, the collision rate on a section of area $\mathrm{d}A$ will go as

$$\frac{1}{\tau_w} = \frac{\mathrm{d}A}{V} \left\langle v_\perp^+ \right\rangle = \frac{\mathrm{d}A\, v}{4\, V}\,, \tag{5.28}$$

where $v_\perp^+$ represents the component of the velocity normal to the surface and directed towards it, so the averaging is done over half of the full solid angle, resulting in a factor of 1/4. Integrating over the whole inner surface area A, a mean free path independent of velocity can be defined to be

$$\lambda_w = \tau_w\, v = \frac{4\, V}{A} \simeq 7.85\,\mathrm{cm}\,, \tag{5.29}$$

where the dimensions of the *nEDM* cell ($7.6{\times}10.2{\times}40\,\mathrm{cm}^3$) have been used in the evaluation. Figure 5.2 shows the typical collision times for ^{3}He atoms in the *nEDM* cell as a function of He bath temperature.

T (mK)	v_{mp} (m/s)	λ_p (cm)
100	15.84	$2.28 \cdot 10^4$
200	22.39	$1.26 \cdot 10^2$
300	27.43	$6.02 \cdot 10^0$
400	31.67	$6.96 \cdot 10^{-1}$
500	35.41	$1.31 \cdot 10^{-1}$
600	38.79	$3.33 \cdot 10^{-2}$
700	41.90	$1.05 \cdot 10^{-2}$
800	44.79	$3.84 \cdot 10^{-3}$

Table 5.1: Kinetic properties of diffuse ^{3}He atoms in superfluid Helium below 1 K as a function of temperature.

In the Monte Carlo simulations the scattering with phonons is modeled so that the direction of motion of ^{3}He atoms after scattering is randomized and so that the speed is picked from the Maxwell-Boltzmann distribution at every scattering event. The time between collisions with phonons is determined by picking a time t_{scat} from a distribution

$$f(t)_{scat} = \frac{1}{\tau_p} \exp\left[-\frac{t}{\tau_p}\right] \mathrm{d}t \tag{5.30}$$

at the beginning of the simulation and after each scattering so that a scattering event can be modeled to occur at the position of the particle at time t_{scat}. This is repeated until the simulation period is over. In addition, re-thermalization of the speed can be implemented at wall reflections. In the lowest temperature regime, where $T < 300$ mK, the mean free path for collisions with excitations is long enough so that ^{3}He atoms do not get a chance to re-thermalize and acquire a new speed of propagation for long periods of time. The process of re-thermalization at the walls is implemented with attention to phase space considerations, resulting in a Maxwell-Boltzmann distribution of velocities, following equation 5.19. Since the faster atoms reach the walls before the slow ones as the frequency of collisions with the walls is linear in v, they have a greater chance of re-thermalizing to a slower velocity and spend a longer time traveling at the lower velocity. After many wall collisions, this would result in a distribution of particle velocities that is skewed toward lower velocities. In order to preserve the density of states, the Maxwell-Boltzmann distribution needs to be scaled by an additional factor v to become

$$f(v) = \frac{2}{v_{mp}^4}\, v^3\, e^{-v^2/v_{mp}^2}\, \mathrm{d}v. \tag{5.31}$$

5.2.3 Numerical Method

A Runge-Kutta numerical method is used to compute the spin precession equation of motions of equation 5.2. The method, outlined in Numerical Recipes [77], relies on the 4^{th} and 5^{th} order approximations of the equations of motion, using adaptive time step computation. By computing two different orders of approximation, it is possible to estimate the error that comes from the numerical approximation at each step. This can be used to either validate a computation, in case the error is below a chosen threshold, or alternatively discard a computed step and require the computation to be repeated using a smaller step which should provide the desired error.

The numerical method, as implemented in the simulation software, has been compared against the known solutions to the Bloch equations, such as equation 5.7, to validate the method. An additional constraint was found to be useful in the computation of spin precession, that is requiring the normalization of the unit spin vector after each numerical step. This can be partially accomplished by replacing the first order Bloch equation 5.2 in the

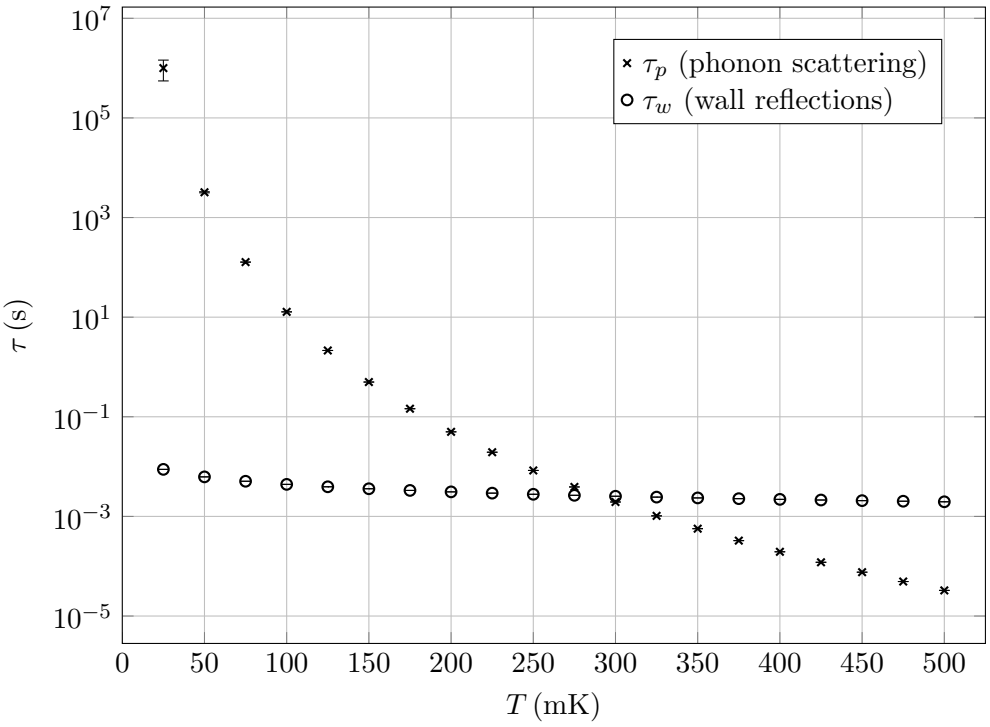

Figure 5.2: Typical times between collision for ^{3}He atoms in the *nEDM* measurement cell as a function of temperature. The small dependence of the mean free period between collisions with the cell walls is due to the increase in average particle speed at higher temperatures.

numerical engine with the second order equation 5.9, although efficiency concerns result in slower overall computation when including second order corrections.

The simulation software was designed so that the numerical computation of spin precession is separate and independent of the position of the particle in the measurement cell. The path that a particle follows in the cell does determine the magnetic field that spin will precess about, but the path is not otherwise affected by the evolution of spin. This implementation must then ignore the magnetic force on the magnetic dipole due to gradients. Because of the separation of geometrical computations from spin precession, the paths are also not affected by the time steps that the numerical method chooses. This method allows to run different simulations in which the complete paths of particles are the same, while the magnetic and electric fields can be varied. In this case, only the path related choices are determined by the random number generator in the code, and they include starting position and velocity vectors, as well as all the diffuse scattering events which change the velocity vector. Therefore, two runs that are started with the same seed but different field parameters will line up exactly in position, for all the particles studied.

5.2.4 Cloud Computing

A run management package was developed around the simulation software to enable Monte Carlo simulation runs to be executed in parallel to increase the overall computing power and decrease simulation run time. Since the particles are modeled not to interact with each other in the simulation runs, their dynamics during the simulations are determined solely by the starting parameters and the random number generator. So it is straightforward to split simulations with any number of particles into smaller runs with fewer particles and run them separately.

The run management is handled over `HTTP` protocol using an open-source Content Management System, Drupal [78] (PHP), to interface with a relational MySQL [79] database for the management of runs. The software was written so that the input parameter files to the binary simulation program would be small and plain textual, which can be easily stored in a database. The output files, on the other hand, are larger and stored using the file format of ROOT [80], organized in *TTree* structures and stored on disk. The web interface offers control of the execution of simulations with the advantage of making a graphical client available to any computer with the sole requirement of having a browser and a connection to the

Internet. For instance, the graphical client allows programmatic generation of run parameters for batch execution. The web interface also provides a layer of simplification to other pieces of software by implementing an API (Application Programming Interface) to which computers on different networks can communicate by exchanging plain-text queries and results over `HTTP`, without need of setting up sophisticated private networks or protocols.

In addition to storing simulation run metadata, the web interface is also responsible for managing a run queue, which is spread over a pool of computing units associated with it. Some of the computers that are local to Kellogg Radiation Laboratory at Caltech were readily added to the pool of available computers, so that some of the processing power could be shared, when unused. Some customization options also allow to choose the number of processors on a single computer to dedicate to the simulation effort. As of Summer 2013, 16 processors over 3 computers are available for simulation work on the KRL network.

Since the communication between worker computers and the central database computer is over `HTTP`, it is up to the worker computers to query the web API for more simulation work and report back on the status of the work. This is advantageous because it concentrates the complexity of the management code onto the central computer with very lightweight scripts on the worker computers. This also reduces the need to share semi-permanent authentication information between worker and server computers reducing possible security issues if one of the workers were to be compromised.

To boost computing power, the simulation package is developed to include capabilities to run on commercially available computing centers. Amazon Web Services (AWS) [81] have been utilized for the purpose. AWS provides virtual environments of Elastic Compute Cloud (EC2) instances for pay, where the full operating system (Linux) is available to the customer, by means of root user access, giving great flexibility on the design of complex systems. The cost of each individual instance ($\approx \$0.10\,\mathrm{h}^{-1}$ in 2013) is computed hourly, so that the system can be used for extra bursts of computing power as needed. Different types of instances are available to satisfy the different use scenarios, such as high-CPU, large memory or large network capabilities. The ones preferred for the Monte Carlo simulations were of high-CPU kind, featuring the equivalent of 20 processors as Elastic Compute Units. The EC2 pricing is modeled in such a way that it does not matter whether the computing is done over the course of a few days on a single instance, or all at once during the course of a few hours on dozens of instances. In addition, if instances are not used, no additional

fee is incurred. This has made the system really useful in cases where time sensitive results were expected and even hundreds of processors have been involved in the simulation effort for a short time. Another service offered is Simple Storage Service (S3) which is used to store interim simulation output from runs that were completed on the AWS network, before transferring them to Caltech for analysis. Deployment of these cloud instances has been automated and consists of booting a pre-prepared instance image (stored on S3), where all the commonly needed software is pre-installed, retrieving the latest version of the simulation source code and compiling it on the machine and setting up the environment. The worker instances then make requests to the central database server for work. Every time a run is completed, the instance sends the output data files to interim storage. Finally the instance is able to turn itself off, if no other work is available.

5.3 Spin Relaxation

A spin ensemble will be subject to spin relaxation under the influence of real-world magnetic fields that are different in magnitude or orientation or that vary differently for different particles. Particles that are trapped and moving in a measurement cell, for instance, will be subject to magnetic fields of different values if the field in the cell is non-uniform. When this happens the spins, which might have started aligned to each other, will precess to different orientations and will no longer be aligned to each other. This can be measured as a decrease in the ensemble polarization.

It is worth looking at two different types of relaxation, namely the longitudinal spin-lattice relaxation with characteristic time T_1, in which the spin polarization with respect to the reference magnetic field changes with time, and the spin-spin transverse relaxation with characteristic time T_2, in which the spin-coherent polarization is measured to decrease.

5.3.1 Longitudinal spin relaxation T_1

The longitudinal spin-lattice relaxation T_1 represents the decay rate of the polarization vector with respect to an externally applied magnetic field B_0. The expected longitudinal polarization as a function of storage time of a spin ensemble is

$$P_{long} \simeq P_{long}(0) \exp\left[-\frac{t}{T_1}\right], \tag{5.32}$$

where $P_{long}(0)$ is the initial polarization at time $t = 0$. This is under the assumption that no external process exists that can interact energetically with the spins in the system, so that no favorable orientation of spins with respect to the magnetic field exists. This assumption is valid in the regime studied where the coupling between spins is negligible. Because of the symmetry of the Bloch equation, the relaxation process would then be equivalent for both polarizations, resulting in the expected equilibrium polarization vanishing as $t \to \infty$ with the spin vector being uniformly distributed over the full solid angle.

In order to simulate the longitudinal relaxation and calculate the expected value for T_1 for a given configuration of fields, in the Monte Carlo simulations, spins start out aligned with the reference magnetic field so that $P_{long}(0) = 1$. The polarization is measured after tracking the spins for a period of simulation time $T \simeq 10 - 100\,\mathrm{s}$. If the reference magnetic field is in the $\hat{x}$ direction, then the polarization can be characterized by the decaying quantity

$$P_{long} = \langle \sigma_x \rangle \,. \tag{5.33}$$

After a period of time T, a spin ensemble relaxes so that the average component of the spin vector aligned with the reference field decreases, while the components transverse to it grow in a way that is azimuthally symmetric. For small deflection angles, the growth of the transverse spin components can be characterized as a normal distribution with width σ

The longitudinal relaxation process for ^{3}He atoms diffusing in superfluid Helium has been simulated to estimate the relaxation time T_1 expected in the *nEDM* experiment at various temperatures below 1 K. The longitudinal relaxation times T_1 expected for UCN are much longer than for ^{3}He because of the lower speed of UCN.

The formalism of McGregor [82] has been used to compute the expected longitudinal relaxation times. The expression for the relaxation rate is given by

$$\frac{1}{T_1} = \frac{\gamma^2}{2} \left[S_{Hy}(\omega_0) + S_{Hz}(\omega_0) \right] \tag{5.34}$$

where ω_0 is the Larmor frequency, γ is the gyromagnetic ratio and where the field spectra S_{Hi} for the two transverse directions in the $y - z$ plane have been used. The spectrum for a single direction can be simplified to

$$S_{Hy}(\omega) = |\nabla B_y|^2 \; S_y(\omega) \tag{5.35}$$

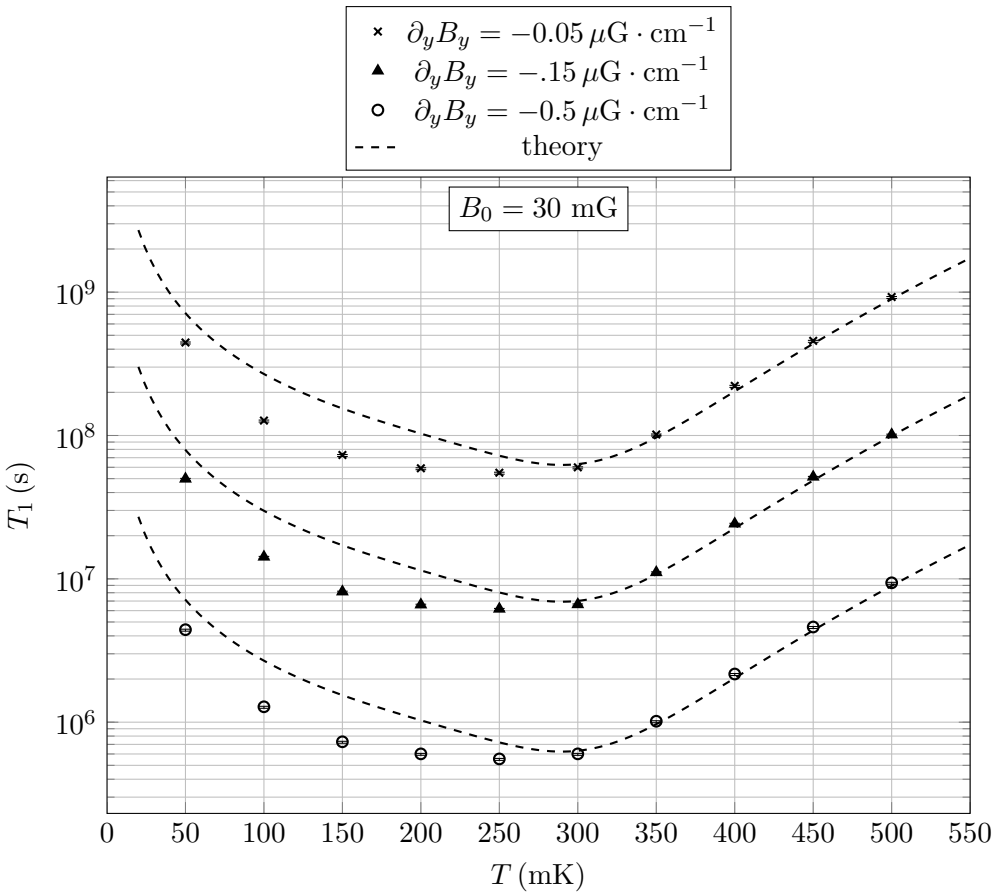

Figure 5.3: Longitudinal spin relaxation times (T_1) extracted from Monte Carlo simulations for ^{3}He atoms as a function of bath temperature for different uniform gradient values. The gradient for these data is uniform and symmetric so that $\partial_x B_x = -2\,\partial_y B_y = -2\,\partial_z B_z$, with the reference field B_0 aligned with the $\hat{x}$ axis. Each data point represents a run consisting of 10,000 particles, so that the error bars in the figure are small ($\sim 1\%$) compared to the values.

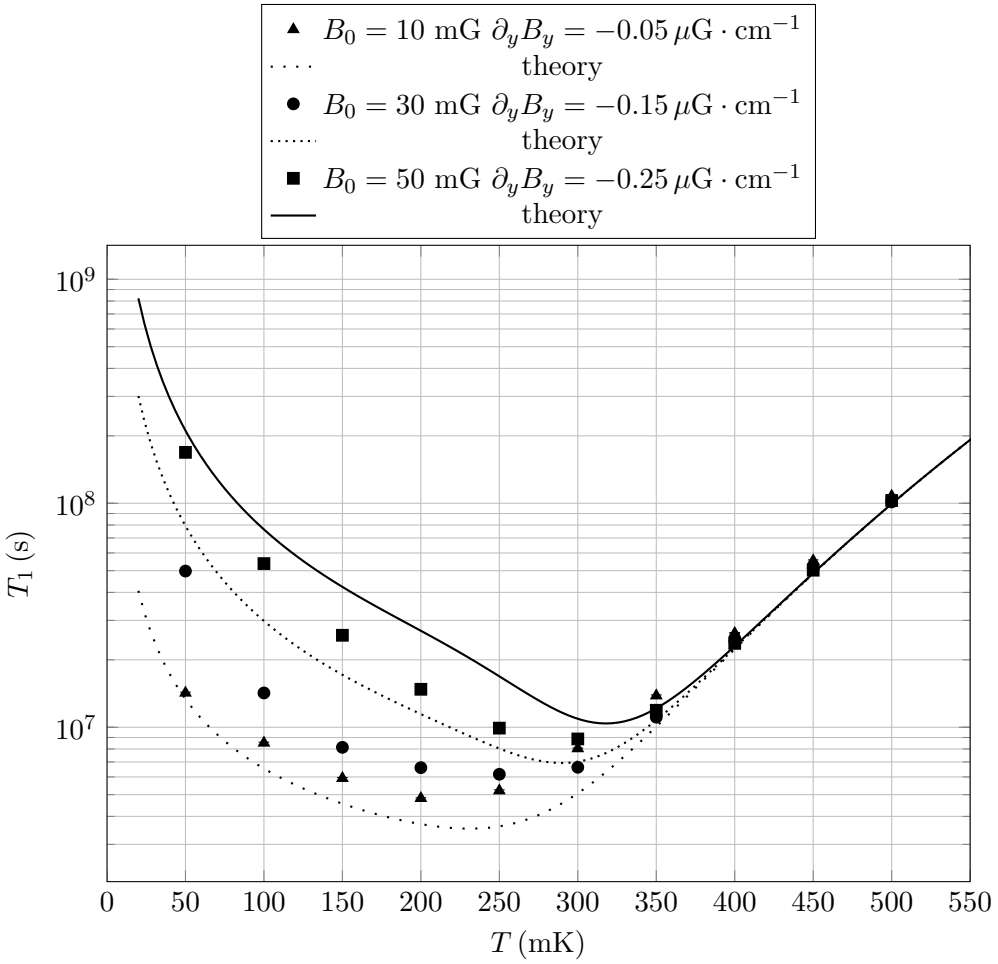

Figure 5.4: Longitudinal spin relaxation times (T_1) extracted from Monte Carlo simulations for ^{3}He atoms as a function of bath temperature. The different simulations share the same value of relative gradient, which is in this case $(1/B_0)\,(\partial B_y/\partial y) = 5 \times 10^{-6}\,\text{cm}^{-1}$. Note that for higher temperatures, the relaxation times depend only on the ratio between the gradient and the holding field, as can be seen from equation 5.38 in the limit $\tau_c \to 0$.

which can be computed from the spectrum of the velocity autocorrelation function

$$\langle v_x(t)\, v_x(t+\tau)\rangle = \left\langle v_x^2 \right\rangle \, e^{-\tau/\tau_c} \tag{5.36}$$

to be

$$S_y(\omega) = \frac{2\,\left\langle v_y^2 \right\rangle \,\tau_c}{\omega^2\,(1+\omega^2\tau_c^2)}. \tag{5.37}$$

If the gradients for the transverse field directions are equal in magnitude, the relaxation rate of Equation 5.34 can be simplified to

$$\frac{1}{T_1} = \frac{|\nabla B_y|^2}{B_0^2}\,\frac{2\,\left\langle v_y^2 \right\rangle \,\tau_c}{1+\omega^2\tau_c^2}, \tag{5.38}$$

where the dependency on the ratio of the gradient magnitude to the reference field B_0 has been explicitly shown.

Figures 5.3 and 5.4 show the data obtained from running Monte Carlo simulations of longitudinal spin relaxation studies for ^{3}He atoms in the *nEDM* cell. In these simulations, the particle spin vectors are started aligned with the B_0 reference field and are allowed to freely precess for a period of time. The polarization of the ensemble is measured at the end of the run. The agreement of the simulation data with the formalism described above is good for the higher temperature regime ($T > 300\,\mathrm{mK}$) where the collisions with phonon excitations dominate and lengths of diffusion are well defined. For the lower temperatures ($T < 300$ mK), the time between phonon collisions becomes longer, comparable to the Larmor period, while the diffuse wall reflections become the principal mode of collision, introducing more subtle effects due to the geometry of the trap that are not included in equation 5.38.

5.3.2 Transverse spin relaxation T_2

The spin-spin relaxation T_2 represents the decay rate of the coherent spin polarization. In a system where spins precess in the $y-z$ plane about field $\boldsymbol{B_0} = B_0\,\hat{\boldsymbol{x}}$ the coherent polarization is represented by the magnitude of the transverse vector

$$P_{trans} = \langle \sigma_y + \mathring{\imath}\,\sigma_z \rangle\,. \tag{5.39}$$

In order to extract the dephasing relaxation rate from the Monte Carlo simulations particle spins start out perpendicular to the reference field and precess for a period T under the influence of the fields in the cell. The average quantities $\langle\sigma_y\rangle$ and $\langle\sigma_z\rangle$ can be computed separately from the data. In addition, it is possible to rotate the mean transverse spin vector so that

$$\begin{pmatrix} \langle\sigma_y'\rangle \\ 0 \end{pmatrix} = \begin{pmatrix} \langle\sigma_y\rangle & \langle\sigma_z\rangle \\ -\langle\sigma_z\rangle & \langle\sigma_y\rangle \end{pmatrix} \cdot \begin{pmatrix} \langle\sigma_y\rangle \\ \langle\sigma_z\rangle \end{pmatrix} \tag{5.40}$$

where the quantity $\langle\sigma_y'\rangle$ represents the magnitude of the polarization and the correlation between the mean quantities is removed and the polarization error can be extracted with ease.

It is also possible to distinguish two processes which contribute to the relaxation of the coherent spin polarization. The first process is strictly dephasing in the precession plane, while the second is relaxation of the spin away from the precession plane. The in-plane dephasing can be extracted by assuming that after precessing for period T a phase angle ϕ will be distributed normally about some angle ϕ_0 so that

$$f(\phi) = \frac{1}{\sqrt{2\pi}\,\sigma_\phi} \exp\left[-\frac{(\phi-\phi_0)^2}{2\,\sigma_\phi^2}\right] \mathrm{d}\phi. \tag{5.41}$$

The width of the distribution is then used to compute the polarization

$$P_{trans} = \frac{1}{\sqrt{2\pi}\,\sigma_\phi} \int_{-\infty}^{\infty} \mathrm{d}\phi\, \cos\phi \exp\left[-\frac{(\phi-\phi_0)^2}{2\,\sigma_\phi^2}\right] \tag{5.42}$$

$$= \exp\left[-\frac{\sigma_\phi^2}{2}\right] \tag{5.43}$$

and the relaxation time can be defined from the relation

$$\frac{1}{T_2} = \frac{\sigma_\phi^2}{2\,T}, \tag{5.44}$$

with T as the measurement period.

The second process of transverse relaxation deals with spins leaving the precession plane, so that after a period T a spread in spherical angle θ is expected. In similar fashion, the

angle θ can be thought of as spread around an angle $\theta_0 \simeq \pi/2$ with some width σ_θ. This relaxation process is related to the longitudinal relaxation T_1.

The full transverse relaxation time T_2 can then be computed from the combined relaxation process

$$\exp\left[-\frac{T}{T_2}\right] = \exp\left[-\frac{\sigma_\phi^2 + \sigma_\theta^2}{2}\right] \tag{5.45}$$

Since the transverse relaxation T_2 is, in general, shorter than the longitudinal relaxation T_1, it is an important concern for the experimental measurement to try to minimize the effect of relaxation and run the measurement so that the expected relaxation time is longer $T_2 \gg T$ than the experimental measurement period.

Figure 5.5 shows simulation results for the transverse spin relaxation times for ^{3}He atoms in a uniform magnetic field gradient, as a function of temperature. The processes of dephasing, T_2^ϕ and that of leaving the precession plane, T_2^θ have been extracted separately from the simulation data to visualize their temperature dependence. The transverse relaxation times become shorter, in this case of a symmetric gradient, as the temperature of the Helium bath increases. This is because the ^{3}He atoms experience a lowered mobility as the mean free path is shortened from phonon scatterings resulting in a broadening of the resonant frequency. The formalism of McGregor [82] described below is used in the figure to compute the full transverse relaxation.

As an example of how the two relaxation processes can yield different results, it is useful to look at two similar uniform gradients, one for which $\partial_x B_x$ is large, resulting in a symmetric gradient condition $\partial_x B_x = -2\,\partial_y B_y = -2\,\partial_z B_z$, and one for which a small value $\partial_x B_x \approx 0$ and an "anti-symmetric" transverse gradient $\partial_y B_y = -\partial_z B_z$ exist. In the case where the gradient along x is large, spins will precess at different frequencies depending on their average x position, with frequency shifts linear in gradient strength. It is expected, then, that the dephasing in angle ϕ will be significant. On the other hand, if only the transverse components of the gradient are present, they contribute a second order shift in the B field, of magnitude

$$\Delta B = \sqrt{B_0^2 + 2\left(\frac{\partial B_y}{\partial y}\, r\right)^2} - B_0 \tag{5.46}$$

$$\simeq \frac{1}{B_0}\left(\frac{\partial B_y}{\partial y}\, r\right)^2, \tag{5.47}$$

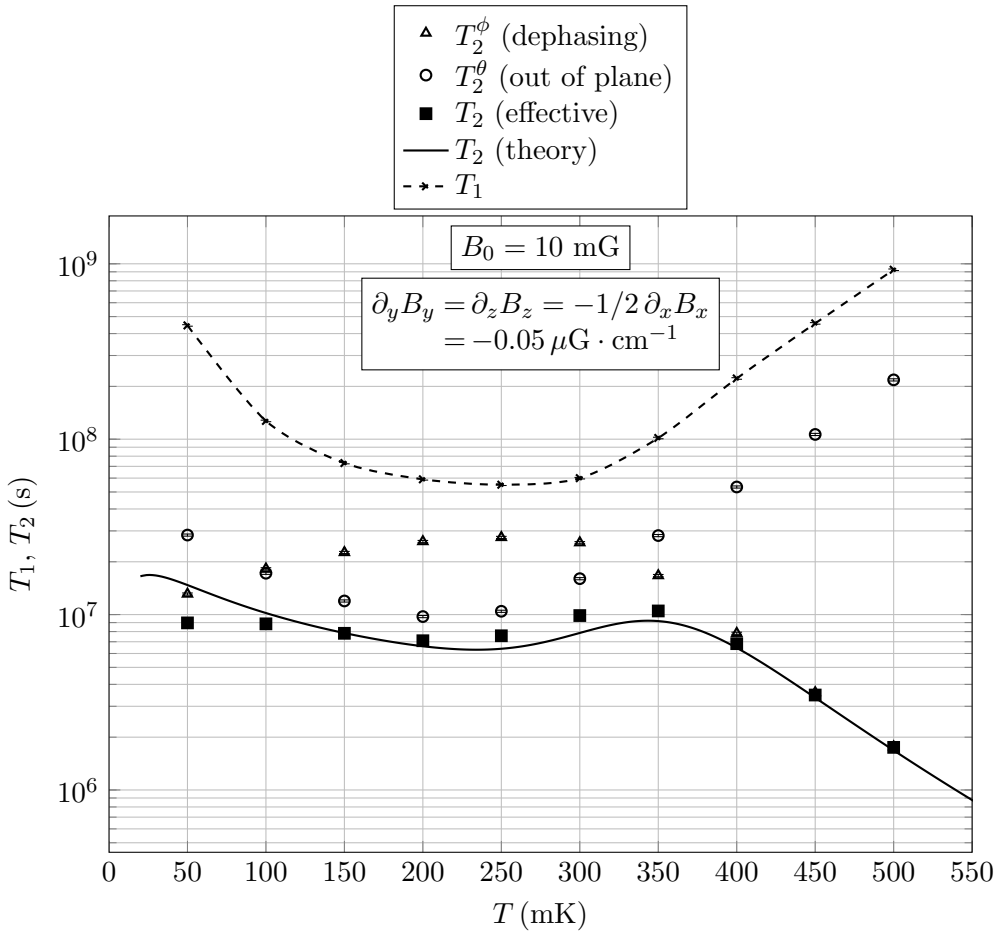

Figure 5.5: Spin relaxation times extracted from Monte Carlo simulations for ^{3}He atoms as a function of bath temperature. The atoms are exposed to a symmetric uniform gradient. The two processes of transverse spin relaxation, dephasing T_2^ϕ and out of plane relaxation T_2^θ have been extracted from the simulation data, as well as the effective transverse spin relaxation T_2. For comparison, the longitudinal relaxation times T_1 are shown. Equation 5.48 has been used for the analytical T_2 curve.

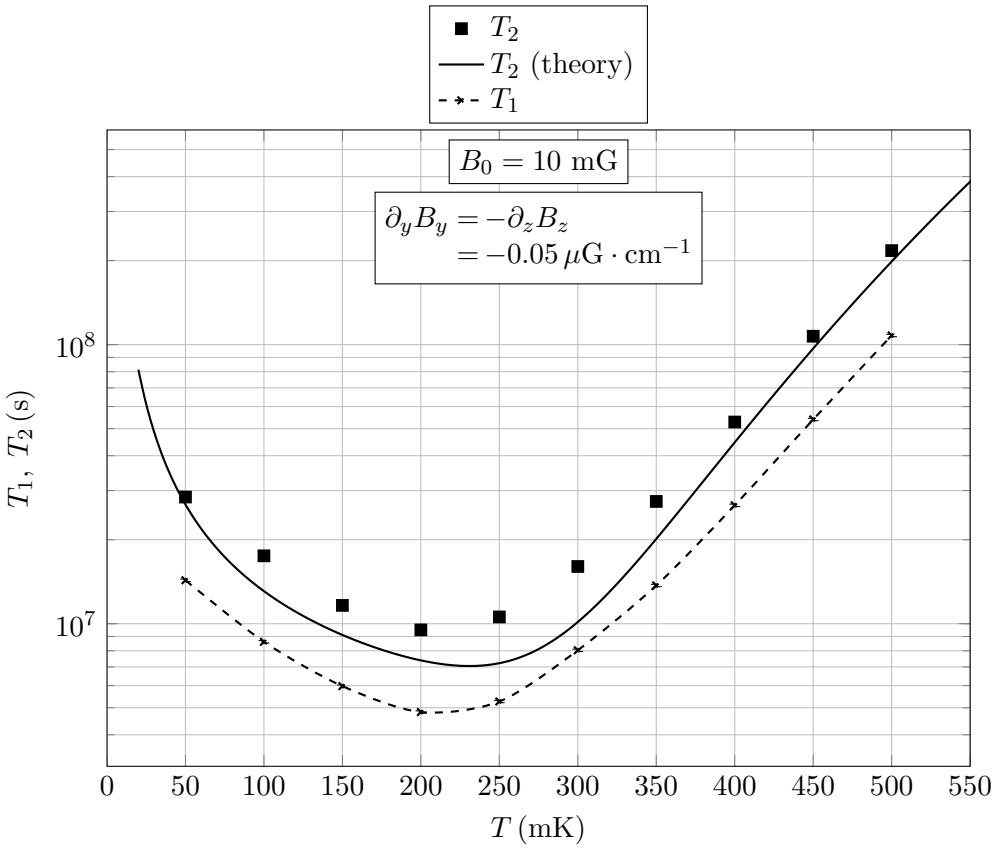

Figure 5.6: Longitudinal (T_1) and transverse (T_2) spin relaxation times extracted from Monte Carlo simulations for ^{3}He atoms as a function of bath temperature. The atoms are exposed to an anti-symmetric magnetic field gradient of the form $\partial_y B_y = -\partial_z B_z$. In this case, the dephasing process is small ($T_2^\phi > 10^{11}$ s) due to a small $\partial_x B_x$ gradient component, and the relaxation time T_2 is dominated by the out of plane relaxation T_2^θ.

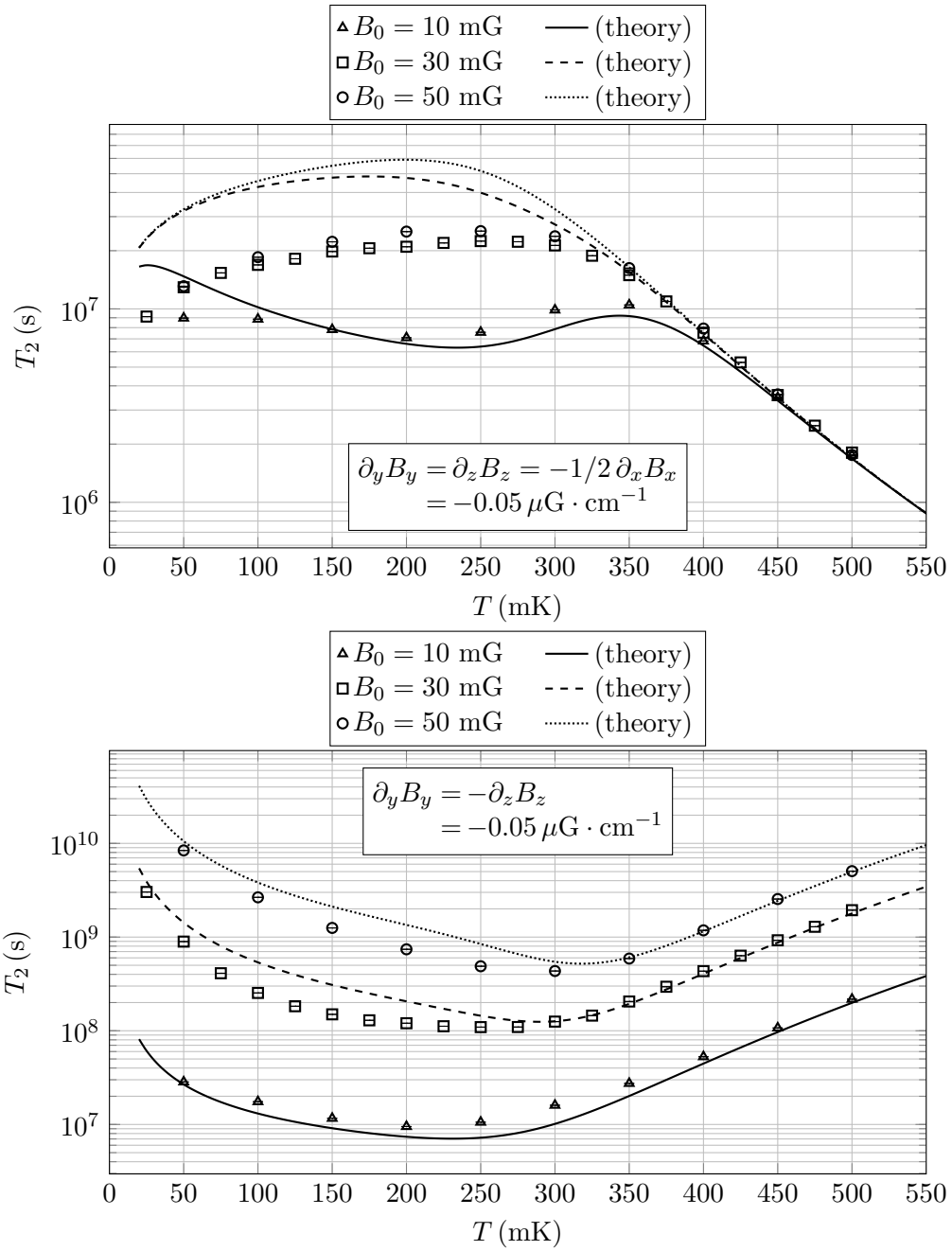

Figure 5.7: Transverse spin relaxation times (T_2) extracted from Monte Carlo simulations for ^{3}He atoms as a function of bath temperature, for different of uniform gradients profiles and magnetic field strengths. In the top figure the magnetic field gradient has a symmetric shape, while on the bottom a gradient is chosen of similar magnitude but of transverse symmetry. The gradient magnitude is not changed as the magnitude of the magnetic field B_0 changes. The analytical curves from equation 5.48 are plotted for comparison.

where r is the distance from the point where $\boldsymbol{B} = B_0\,\hat{\boldsymbol{x}}$. In this case, the dephasing in angle ϕ should occur slower than in the symmetric gradient case —assuming equal magnitude transverse gradients— while the relaxation process akin to the longitudinal relaxation T_1 of section 5.3.1 would still exist, resulting in longer T_2 relaxation times. It is possible in such a case for the transverse relaxation time T_2 to be longer than the T_1 longitudinal relaxation time, as shown in figure 5.6.

The formalism of McGregor [82] can be used to compute the transverse relaxation times for the cases described above and for the geometry of the *nEDM* cells. The long rectangular prism geometry is similar to a long cylindrical geometry, so that equation (37) in [82] can be applied and the transverse relaxation becomes

$$\frac{1}{T_2} = \frac{1}{2\,T_1} + \frac{1}{120}\,\frac{\gamma^2\,L^4}{D}\,\left(\frac{\partial B_x}{\partial z}\right)^2 + \frac{7}{96}\,\frac{\gamma^2\,a^4}{D}\,\left(\frac{\partial B_x}{\partial x}\right)^2\,, \tag{5.48}$$

where a is the radius of a cylinder that can be approximated by the average of the two smallest half-sides of the rectangular prism cell, $a = (L_x + L_y)/4$. The temperature dependent diffusion coefficient D, introduced in equation 5.21, should be replaced by a suitable coefficient that includes wall collisions, important for low Helium temperatures. Such a replacement can be done by noting that the transverse relaxation time constant of relevance is τ_D, of equation 5.26, where the effective collision time τ_c includes the mean wall collision time, so that from equation 5.24, the relation is then

$$D' \to \frac{1}{3}\,v_{rms}^2\,\tau_c\,, \tag{5.49}$$

where the effective collision time, inclusive of wall collisions is used instead. It is clear that the last term of equation 5.48 does not contribute to the relaxation if the gradient along x vanishes, so that in that case the transverse relaxation rate is simply related by $T_2 = 2\,T_1$. If a gradient of the form $\partial B_x/\partial z$ is present, the relaxation is proportional to the fourth power of the length of the cell, from the second term of equation 5.48. The longest length of the cell is planned to be $L_z = 40$ cm for the *nEDM* experiment, so that the ratio $(L_z/a)^4 \simeq 6.52 \times 10^3$, resulting in a relaxation rate likely dominated by the gradient along z. Figure 5.7 shows the simulation results for transverse spin relaxation for ^{3}He atoms, where the relaxation is dominated by the $\partial B_x/\partial x$ gradient term of equation 5.48. Figure

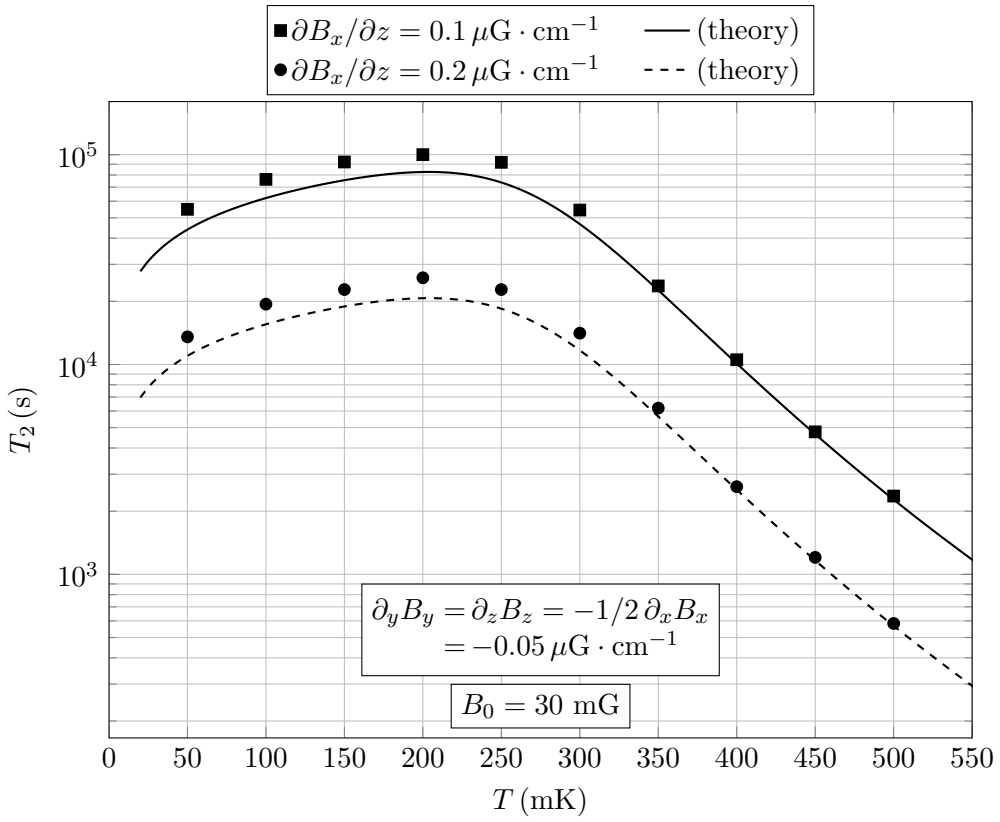

Figure 5.8: Transverse (T_2) spin relaxation times extracted from Monte Carlo simulations for ^{3}He atoms as a function of bath temperature. In addition to a uniform symmetric magnetic field gradient, a uniform gradient of the form $\partial B_x/\partial z$ along the longer side of the measurement cell has been included. The second term of equation 5.48 contributes to the shorter relaxation times, as compared to the values in figure 5.7.

5.8 shows an example of relaxation times for ^{3}He under the influence of a gradient along z of magnitude $\partial B_x/\partial z = \partial B_z/\partial x = 0.1\,\mu\mathrm{G}\cdot\mathrm{cm}^{-1}$.

5.3.2.1 Field symmetry considerations

It is worth noting that the transverse spin relaxation rate is related [82, 83] to the characteristic diffusion time τ_D and to the deviation in precession frequency by

$$\frac{1}{T_2} = \left\langle (\Delta\omega)^2 \right\rangle \tau_D \tag{5.50}$$

$$= \gamma^2 \left\langle (\Delta B)^2 \right\rangle \tau_D\,, \tag{5.51}$$

and is present in the last two terms of equation 5.48, where a constant gradient is assumed to permeate a dimension of the cell, L for instance. It is possible to relate a constant

gradient to the field deviation for a single direction, z for instance, if the field is expressed as

$$B_x(z) = B_0 + G_z\, z\,, \tag{5.52}$$

where $G_z = \partial B_x/\partial z$ is the constant gradient in question. The field deviation, averaged over L, is then computed to be

$$\left\langle \left(\Delta B^2\right)\right\rangle_L = \left\langle B^2\right\rangle_L - \left(\langle B\rangle_L\right)^2 \tag{5.53}$$

$$= \left(B_0^2 + 2\, B_0\, G_z \left\langle z\right\rangle + G_z^2 \left\langle z^2\right\rangle\right) - B_0^2 \tag{5.54}$$

$$= G_z^2 \left\langle z^2\right\rangle_L = G_z^2\, \frac{L^2}{12}\,. \tag{5.55}$$

If the magnetic field profile in the same direction were to be quadratic, the gradient would be linear in z instead of constant and the field could be expressed as

$$B_x(z) = B_0 + \frac{\sqrt{3}}{L}\, Q_z\, z^2\,, \tag{5.56}$$

where Q_z represents the quadratic coefficient of the magnetic field, scaled to equal the root mean square of the gradient

$$\left\langle \left(\frac{\partial B_x}{\partial z}\right)^2 \right\rangle = \frac{12}{L^2}\, Q_z^2 \left\langle z^2\right\rangle = Q_z^2\,. \tag{5.57}$$

It is possible to compute the average field deviation for this field over the length L of the cell to be

$$\left\langle \left(\Delta B^2\right)\right\rangle = \left\langle B^2\right\rangle - \left(\langle B\rangle\right)^2 \tag{5.58}$$

$$= \left(B_0^2 + \frac{2\sqrt{3}}{L}\, B_0\, Q_z \left\langle z^2\right\rangle + \frac{3}{L^2}\, Q_z^2 \left\langle z^4\right\rangle\right) - \left(B_0 + \frac{\sqrt{3}}{L}\, Q_z \left\langle z^2\right\rangle\right)^2 \tag{5.59}$$

$$= \frac{3}{L^2}\, Q_z^2 \left(\left\langle z^4\right\rangle - \left\langle z^2\right\rangle^2\right) = Q_z^2\, \frac{L^2}{60}\,. \tag{5.60}$$

Since the mean square gradient for the linear case is simply G_z^2, equation 5.55 shows that, given the same root mean square gradients, the rate of spin relaxation should be at least a factor of $60/12 = 5$ smaller for a quadratic gradient than a constant gradient. In addition, an argument of symmetry comes into play in the diffusion time τ_D. In fact, the diffusion

time varies as $\propto L^2$, but this is the characteristic time to sample the field, so that if the field is symmetric about $z = 0$ then the length used in the computation of τ_D can be halved, giving an additional improvement of 4 over the constant gradient case. The total improvement in T_2 for a quadratic profile over a constant gradient is ~ 20, assuming the same root mean gradient. It is then important to make sure that the magnetic coils are designed in such a way to produce a field that is symmetric.

5.4 Motional $v \times E$ Field

A particle moving in a stationary electric field must experience a motional magnetic field B_v in the particle's rest frame. This is due to the apparent motion of the charges that comprise the stationary electric field in a frame moving with the particle. Since B_v comes from a Lorentz transformation of the stationary electric field, the nature of the motional field is relativistic, but since the velocities of the particles of interest in this work (e.g. ^{3}He atoms and UCN) are small compared to the speed of light, the relativistic factor $\gamma \simeq 1$ does not contribute to the magnitude of the field and can be neglected. In SI units the motional field is then

$$\boldsymbol{B_v} = \frac{\boldsymbol{E} \times \boldsymbol{v}}{c^2}\,, \tag{5.61}$$

where only components of the velocity $\boldsymbol{v}$ perpendicular to the electric field $\boldsymbol{E}$ give rise to the field and the motional field is perpendicular to $\boldsymbol{E}$.

If the particle has a magnetic moment, then the spin equations of motion will be subject to the particle's local field

$$\boldsymbol{B'} = \boldsymbol{B_0} + \frac{\boldsymbol{E} \times \boldsymbol{v}}{c^2}. \tag{5.62}$$

If an external reference magnetic field $\boldsymbol{B_0}$ that is parallel in direction to the $\boldsymbol{E}$ field is applied to the system, the motional field contributes a small tilt of the direction of the local field $\boldsymbol{B'}$ by an angle

$$\theta \simeq \sin\theta = \frac{B_v}{\sqrt{B_0^2 + B_v^2}} \tag{5.63}$$

$$\simeq \frac{B_v}{B_0}. \tag{5.64}$$

In addition, the motional field contributes to an increase in the magnitude of the local field

in quadrature

$$\frac{B'}{B_0} = \sqrt{1 + \left(\frac{B_v}{B_0}\right)^2} \tag{5.65}$$

$$\simeq 1 + \frac{B_v^2}{2\,B_0^2} = 1 + \frac{E^2\,v_\perp^2}{2\,B_0^2\,c^2}, \tag{5.66}$$

where $v_\perp$ is the component of the velocity perpendicular to the field E.

Although the speeds are generally small compared to the speed of light, the motional field B_v due to large electric fields is not negligible, especially in systems where the ambient magnetic field is small. For instance, a particle moving perpendicular to an electric field $E = 100\,\mathrm{kV}\cdot\mathrm{cm}^{-1}$ at a mere $v = 1\,\mathrm{m}\cdot\mathrm{s}^{-1}$ will experience a motional field of magnitude $B_v \simeq 1.1\,\mu\mathrm{G}$. For the case of the *nEDM* measurement where the magnitude of the holding field $B_0 \simeq 30\,\mathrm{mG}$, the motional field B_v is large enough to affect the spin precession of the moving particles.

A similar argument can be done for a particle moving through a stationary magnetic field. It will experience a motional electric field E_v in its rest frame from the simple equivalence of the Lorentz force in the lab frame. The motional electric field would have a form

$$\boldsymbol{E_v} = \boldsymbol{v} \times \boldsymbol{B} \tag{5.67}$$

where the relativistic factor $\gamma \simeq 1$ has been neglected. Even though the motional field E_v is not scaled by a factor of $1/c^2$, its relative strength at non-relativistic speeds is small compared to an externally applied electric field. In fact, its magnitude in a field $B_0 = 30\,\mathrm{mG}$ and in a reference frame moving with velocity of $v = 1\,\mathrm{m}\cdot\mathrm{s}^{-1}$ is $E_v = 3\,\mu\mathrm{V}\cdot\mathrm{m}^{-1}$, a decisively small quantity that can be ignored.

5.4.1 Collisions

Since the motional field $\boldsymbol{B_v}$ of a moving particle depends on the direction and magnitude of the velocity $\boldsymbol{v}$ with respect to the electric field $\boldsymbol{E}$, a change in velocity signifies a change in the local field of the moving particle. A reflection from a boundary wall or a scattering collision will alter the path of a moving particle resulting in changes in the motional field. If gravity affects the direction of motion perpendicular to a uniform electric field, the motional field will also vary. Because the motional field is perpendicular to $\boldsymbol{v}$ and $\boldsymbol{E}$, it will appear

to be following the motion of the particle as it bounces in the measurement cell.

5.5 Motional spin relaxation

An interesting consequence of the motional $\boldsymbol{v} \times \boldsymbol{E}$ field arises for particles with magnetic moment moving in an externally applied combination of E and B fields, whose motion is constrained to a volume or subject to collisions. An ensemble of such particles would experience many changes in velocity with respect to the stationary E field, so that its motional field would be constantly and abruptly varying in direction due to wall collisions. The effective magnetic field would be "tilted" in the direction of the motional field. These small random shifts in the orientation of B will induce relaxation of the ensemble's magnetization. The interesting aspect of the nature of this relaxation process is that it can occur even in a combination of E and B fields that are perfectly uniform [84].

The relaxation process can be related to the relaxation processes of section 5.3 where the magnetic field gradients are now replaced by the motional fields. Since the motional fields are perpendicular to E, and thus B_0, the situation is similar to the case mentioned in 5.3.2 for a vanishing component of the gradient along B_0, namely $\partial_x B_x \approx 0$, so that the effect of dephasing, T_2^{ϕ}, is small and the longitudinal and transverse relaxation times are related by

$$T_2 \simeq 2\,T_1\,. \tag{5.68}$$

Figure 5.9 shows the effect of the electric field on the relaxation times for ^{3}He atoms.

The longitudinal relaxation times can be computed from equation 5.34 of [82] with a suitable replacement for $S_{Hy}(\omega_0)$ and $S_{Hz}(\omega_0)$, for shifts due to the motional field B_v. The equivalent transverse fields can be expressed by

$$\begin{aligned} \widetilde{B}_y &= -\,E\,v_z\,/c^2 \\ \widetilde{B}_z &= E\,v_y\,/c^2\,, \end{aligned} \tag{5.69}$$

where the reference fields B_0 and E are assumed to be pointing along the x direction. The expression for the spectrum is found [85] to be related to the velocity autocorrelation

function

$$\left\langle \widetilde{B}_y(t)\, \widetilde{B}_y(t+\tau) \right\rangle = \langle v_z(t)\, v_z(t+\tau) \rangle \, \frac{E^2}{c^4} \tag{5.70}$$

$$= \frac{E^2}{c^4} \, \left\langle v_z^2 \right\rangle \, e^{-\tau/\tau_c} \tag{5.71}$$

where the substitution of equation 5.36 was introduced and with a similar expression for the other transverse component. The spectrum is then

$$S_{Hy}(\omega) = \frac{E^2}{c^4} \, \frac{2 \left\langle v_z^2 \right\rangle \, \tau_c}{1 + \omega^2 \tau_c^2} \tag{5.72}$$

Because of symmetry considerations, the longitudinal relaxation rate is then expressed

$$\frac{1}{T_1} = \frac{2}{3} \, \frac{\gamma^2 \, E^2}{c^4} \, \frac{v_{rms}^2 \, \tau_c}{1 + \omega_0^2 \, \tau_c^2} \, , \tag{5.73}$$

where the substitution $\left\langle v_y^2 \right\rangle + \left\langle v_z^2 \right\rangle = 2/3 \, v_{rms}^2$ has been used.

In the case that a magnetic field gradient is present, along with a large E field, the motional spin relaxation and the relaxation due to the gradient can interact differently, so that a systematic difference in relaxation rates can be expected if the gradient field and the motional field tend to be aligned or not, as can be seen in figure 5.9.

5.6 Geometric phase

An important systematic effect in the search for Electric Dipole Moments comes from the interaction of magnetic moments with the motional $\boldsymbol{v} \times \boldsymbol{E}$ field [22]. The effect in question, named *Geometric Phase* (GP), is akin to Berry's phase [86, 87] and it alters the effective precession frequency of magnetic moments precessing in a $B + E$ field combination in a way that is dependent on the relative alignment of the fields. The geometric phase has been studied extensively for its relevance in EDM measurements [88, 89], on beams [24] as well as on particles in traps [31, 90]. The systematic shift in frequency is linear in E and gives rise to an effective *false EDM* for the particles in question, which looks like a physical EDM, as it changes sign with reversal of the E field. The geometric phase affects the precession of UCN and ^{3}He atoms differently, due to their different kinematic properties. The measurement of the EDM is effectively extracted from the relative frequency difference of the two spin

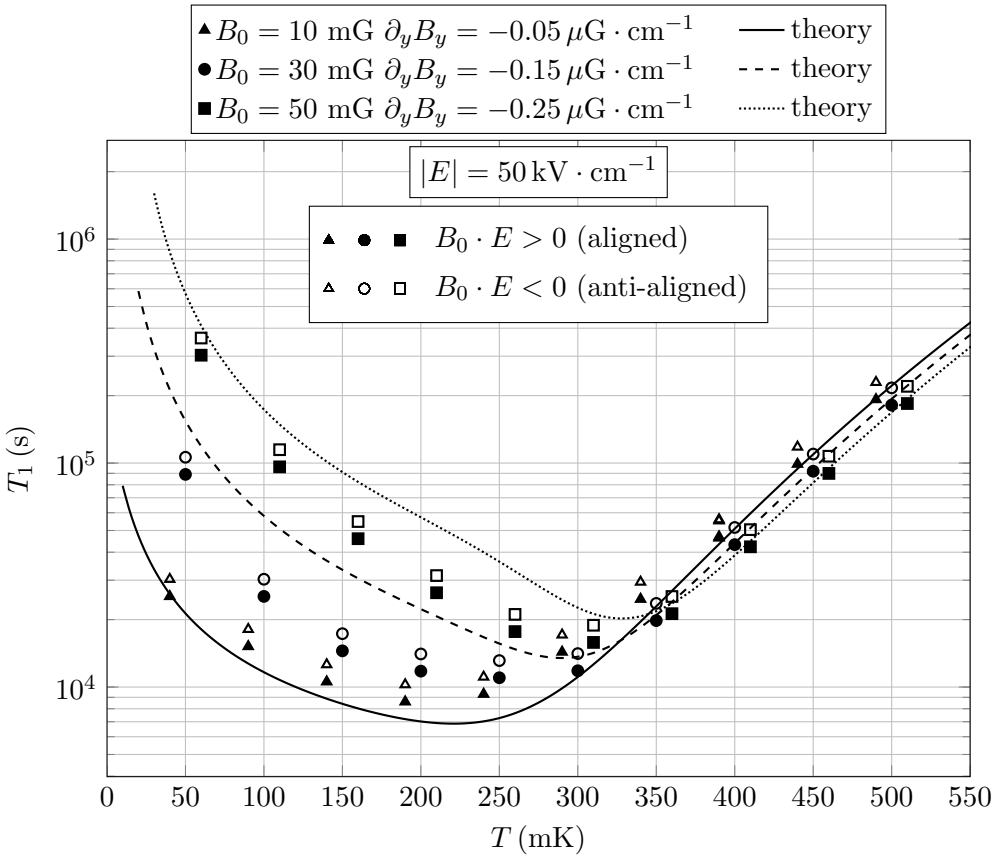

Figure 5.9: Monte Carlo simulations results showing the effect of motional spin relaxation on T_1 for ^{3}He atoms as a function of bath temperature. A uniform symmetric magnetic field gradient with relative magnitude $(1/B_0)\,(\partial B_y/\partial y) = 5 \times 10^{-6}\,\text{cm}^{-1}$ permeates the cell, as well as the electric field E parallel to B_0. A noticeable variation in relaxation times between runs with E and B aligned and anti-aligned comes from the interaction of the magnetic field gradient with the motional field. Note that groups of values have been shifted horizontally for clarity. The model of equation 5.73, adapted to include the relaxation due to the gradient is shown to agree with the simulation data.

systems, so both have been studied in simulation. Experimentally, the false EDM differs from a physical EDM because it depends on the kinematics of the system and if variations of experimental parameters, other than the E field, introduce systematic effects on the false EDM itself, then it can be distinguished from a physical EDM.

As seen in Equation 5.65, the motional field will, in general, increase the effective precession frequency quadratically in E regardless of the relative alignment of the E and B fields. This frequency shift does not result in a false EDM since it can be recognized as a systematic shift by measuring the precession frequency of a setup where the relative alignment of the fields has been inverted. The EDM signal is extracted from the difference in precession frequencies between the aligned field configuration ($\uparrow\uparrow$) and the anti-aligned ($\uparrow\downarrow$). Considering that both configurations will introduce different shifts from the frequency expected from precession in uniform B_0 so that

$$\Delta\omega^{\uparrow\uparrow} = \omega^{\uparrow\uparrow} - \omega_0 \,, \tag{5.74}$$

with similar expression for the anti-aligned ($\uparrow\downarrow$) case, the false EDM due to the geometric phase can be obtained from the difference

$$d_{\mathrm{GP}} = -\frac{\hbar}{2}\,\frac{\Delta\omega^{\uparrow\uparrow} - \Delta\omega^{\uparrow\downarrow}}{2\,E} \,, \tag{5.75}$$

where $J = 1/2$ is assumed from here on for the case of spin-1/2 particles. With the fields anti-aligned, a precession shift quadratic in E would be identical as in a setup with the fields aligned which is not characteristic of an EDM and would cancel out.

5.6.1 Origin of the false EDM

In the presence of an electric field E, the geometric phase effect arises from the precession of spins in an inhomogeneous magnetic field where the motional $v \times E$ field B_v is non-negligible and it adds by superposition with non-uniformities in the B field. Only the non-uniformities in B that are perpendicular to E can produce a false EDM. When the E field direction is inverted, the motional field changes sign and where there was once constructive interference with inhomogeneities in the B field, resulting in a slight increase in precession frequency, the interference is now destructive and the resulting precession is slower. An inversion

of the particle direction of motion also switches the sign of B_v. It might be expected, then, that averaging over the velocity distribution could effectively cancel the difference in precession frequencies between the two E field directions, but in fact this canceling out does not happen, as shown below.

5.6.1.1 Motion in one dimension

In a simple example the geometric phase arises for a particle moving in one dimension without collisions and under the influence of a uniform magnetic field gradient. The reference B_0 and E fields are aligned with the $\hat{x}$ direction and the particle can move along $\hat{z}$ with velocity v_z, so that the motional field is $B_v = -E\,v_z/c^2\,\hat{y}$, where the signs of E and v_z determine its direction. In the presence of a constant small field gradient, the total field in the frame of the moving particle is given by

$$\boldsymbol{B}(t) = \left(B_0 + \frac{\partial B_x}{\partial z}\,z(t)\right)\hat{x} + \left(\frac{\partial B_y}{\partial z}\,z(t) - \frac{E\,v_z(t)}{c^2}\right)\hat{y} + \frac{\partial B_z}{\partial z}\,z(t)\,\hat{z}\,. \tag{5.76}$$

Because of the motion of the particle, the field changes in time as

$$\frac{\partial \boldsymbol{B}(t)}{\partial t} = \frac{\partial \boldsymbol{B}}{\partial z}\,v_z(t)\,, \tag{5.77}$$

so that if the field from the gradient is small with respect to B_0, the total field will appear to slightly tilt away from $\hat{x}$, with an angle between the total field and B_0 given by

$$\left|\boldsymbol{B_0} \times \left(\boldsymbol{B_0} + \frac{\partial \boldsymbol{B}}{\partial z}\,z(t)\right)\right| = B_0^2\sqrt{1 + \frac{1}{B_0^2}\left(\frac{\partial B}{\partial z}\,z(t)\right)^2}\;|\sin\theta| \tag{5.78}$$

$$\left|\boldsymbol{B_0} \times \frac{\partial \boldsymbol{B}}{\partial z}\,z\right| \simeq B_0^2\;|\theta|\;, \tag{5.79}$$

so that a frequency of rotation can be found to be

$$\boldsymbol{\omega_r} = \dot{\boldsymbol{\theta}} \simeq \frac{\boldsymbol{B_0}}{B_0^2} \times \frac{\partial \boldsymbol{B}}{\partial z}\,v_z\,, \tag{5.80}$$

where the cross product ensures that the rotation vector represents the direction of rotation in the usual way. A rotating reference frame can now be chosen where the total field is stationary and a pseudo-magnetic field of magnitude ω_r/γ arises from the rotation. The

pseudo-magnetic field can interfere with the motional field B_v for a gradient along the direction of motion, $\partial B_z/\partial z$, so that the effective field in the rotating frame is given by

$$\boldsymbol{B'} = B_0\,\hat{x} + \left(\frac{1}{\omega_0}\,\frac{\partial B_z}{\partial z} - \frac{E}{c^2}\right)\,v_z\,\hat{y} \tag{5.81}$$

where the sign of E determines whether the interference is constructive or destructive. The interference does not change if the velocity of the particle v_z is inverted. This results in a shift in frequency of precession that is asymmetric for different orientations of the E field and does not average out over the two velocity directions. The magnitude of the frequency shift is given by

$$\Delta\omega = -\gamma\,B' - \omega_0 \tag{5.82}$$

$$= -\gamma\,\left(B' - B_0\right) \tag{5.83}$$

so the difference in shifts between the two $B + E$ field alignments is

$$\Delta\omega^{\uparrow\uparrow} - \Delta\omega^{\uparrow\downarrow} = \gamma\,\sqrt{B_0^2 + v_z^2\,\left(\frac{1}{\omega_0}\,\frac{\partial B_z}{\partial z} + \frac{E}{c^2}\right)^2} + \tag{5.84}$$

$$- \gamma\,\sqrt{B_0^2 + v_z^2\,\left(\frac{1}{\omega_0}\,\frac{\partial B_z}{\partial z} - \frac{E}{c^2}\right)^2} \tag{5.85}$$

$$\simeq -\frac{2\,v_z^2\,E}{B_0^2\,c^2}\,\frac{\partial B_z}{\partial z}\,. \tag{5.86}$$

As pointed out in [31], this shift in frequency does not depend on the gyromagnetic ratio of the particle in question, but only on the magnitude of the gradient relative to the square of B_0.

5.6.1.2 Motion in multiple dimensions

Any time the total field appears to be rotating due to the motion of a particle in a trap, the pseudo-magnetic field of the rotating frame can interfere with the motional field. Only motion perpendicular to the reference fields contributes to a non-vanishing phase accumulation, so that the difference in precession frequency shift with contributions from two

dimensions is

$$\Delta\omega^{\uparrow\uparrow} - \Delta\omega^{\uparrow\downarrow} = -\frac{2\,E}{B_0^2\,c^2}\left[v_y^2\,\frac{\partial B_y}{\partial y} + v_z^2\,\frac{\partial B_z}{\partial z}\right] \tag{5.87}$$

$$= -\frac{2\,E}{c^2}\left[\frac{v_y^2}{\omega_0^2}\,\frac{\partial B_y}{\partial y} + \frac{v_z^2}{\omega_0^2}\,\frac{\partial B_z}{\partial z}\right]. \tag{5.88}$$

If the uniform gradient is symmetric so that $\partial_y B_y = \partial_z B_z = -\partial_x B_x/2$, then the above expression becomes

$$\Delta\omega^{\uparrow\uparrow} - \Delta\omega^{\uparrow\downarrow} = \frac{v_\perp^2\,E}{B_0^2\,c^2}\,\frac{\partial B_x}{\partial x} \tag{5.89}$$

where $v_\perp$ represents the magnitude of the components of velocity perpendicular to $\hat{x}$. On the other hand, if the gradient is anti-symmetric so that $\partial_y B_y = -\partial_z B_z$ the frequency difference becomes

$$\Delta\omega^{\uparrow\uparrow} - \Delta\omega^{\uparrow\downarrow} = -\frac{2\,E}{B_0^2\,c^2}\,\frac{\partial B_y}{\partial y}\,\left(v_y^2 - v_z^2\right), \tag{5.90}$$

so that some canceling of the effect occurs when averaged over the possible velocities as $\langle v_y^2\rangle \simeq \langle v_z^2\rangle$.

5.6.1.3 Geometric phase and collisions

The arguments on the origin of the geometric phase as described above do not take into account particle collisions during its motion, and can be valid for ballistic motion, but it turns out that collisions can have a large effect on the geometric phase. The direction of motion of a particle in the trap changes due to collisions with the walls or other particles, and the geometric phase can accumulate if the field due to inhomogeneities in the magnetic field appears to be rotating in the local frame of a particle. The classical direction of Larmor spin precession about the B_0 field provides a preferred sense of rotation for a transverse magnetic field. If a particle follows a path that is curving around the direction of the reference fields due to collisions, the motional field which is always perpendicular to the velocity vector will appear rotating in the local frame of the particle. Depending on the geometry of the magnetic field, there can also be a transverse component of the magnetic field that is co-rotating and interfering with the motional field. The apparent rotation of a small field B_r about B_0 will change its relative strength with respect to B_0. This is because, in a frame rotating about B_0 at frequency ω_r, where a rotating field B_r appears

to be stationary, B_0 appears modified by a pseudo-field so that

$$B_0' \to B_0 + \frac{\omega_r}{\gamma}\,, \tag{5.91}$$

and in the case in which $\omega_r = \omega_0 = -\gamma\, B_0$, the effective field cancels B_0. In the rotating frame, the total magnetic field magnitude is

$$\left|\boldsymbol{B'}\right| = \sqrt{\left(B_0 + \frac{\omega_r}{\gamma}\right)^2 + (B_r)^2} \tag{5.92}$$

so that the Larmor frequency is $\omega_0' = -\gamma\,|B'|$, where the alignment of B' with respect to B_0 must be taken into account when the pseudo-field ω_r/γ is larger than B_0. Back in the laboratory frame, the effective precession frequency shift is given by

$$\Delta\omega = (\omega_r - \omega_0) - \gamma\, B' \tag{5.93}$$

$$= (\omega_r - \omega_0)\ \times \left[1 - \frac{\gamma}{|\gamma|}\sqrt{1 + \frac{\gamma^2\, B_r^2}{(\omega_r - \omega_0)^2}}\right]. \tag{5.94}$$

This form allows for cases where $\omega_r > \omega_0 > 0$ and the rotating field is, in essence, outpacing the rotation of the spin vector in the same direction, as well as $\omega_r < \omega_0$, but breaks down when $\omega_r \simeq \omega_0$, resulting in resonances. Because the shift is such that ω_r affects the relative strength B_r/B' of the rotating field on the Larmor precession, the interference between the motional field B_v and the magnetic gradient will be asymmetric if the E field is inverted, and the geometric phase does not cancel out when the velocity is averaged between two opposite directions of motion.

A simple scenario considered by [31, 75], for which the geometric phase effect is easily calculable for a rotating path, applies to traps of circular geometry with E and B perpendicular to the plane of the circle, and with a gradient of circular symmetry, with $\partial_y B_y = \partial_z B_z = -\partial_x B_x/2$. Considering only the particles that travel in the plane of the circle and following garland paths along the circumference of the trap, both the motional $v \times E$ field and the gradient field appear rotating at a constant frequency in the reference frame of the particle. Their motion is parametrized by the radius R of the trap and the velocity in the plane $v_\perp$, so that the angular frequency of a rotating frame where the fields appear stationary is $\omega_r = v_\perp/R$. Equation 5.94 describes the expected shift. The rotating

field is expressed as

$$B_r = -\left(\frac{1}{2}\frac{\partial B_x}{\partial x} + \frac{E}{c^2}\,\omega_r\right) R\,\hat{r}\,, \tag{5.95}$$

where $\hat{r}$ represents the radial vector and the reference fields B_0 and E are assumed to be parallel with $\hat{x}$, and aligned or anti-aligned depending on the sign of E. The difference in frequency shift for $B + E$ fields aligned ($\uparrow\uparrow$) and anti-aligned ($\uparrow\downarrow$) can be expressed as

$$\Delta\omega^{(\uparrow\uparrow)} - \Delta\omega^{(\uparrow\downarrow)} = -\frac{\gamma}{|\gamma|}\,(\omega_r - \omega_0) \times \left[\sqrt{1 + \frac{(\gamma\, B_r^{(\uparrow\uparrow)})^2}{(\omega_r - \omega_0)^2}} - \sqrt{1 + \frac{(\gamma\, B_r^{(\uparrow\downarrow)})^2}{(\omega_r - \omega_0)^2}}\right] \tag{5.96}$$

$$\simeq -\frac{\gamma^3}{|\gamma|}\,\frac{1}{\omega_r - \omega_0}\,\frac{(B_r^{(\uparrow\uparrow)})^2 - (B_r^{(\uparrow\downarrow)})^2}{2} \qquad \text{for } B_r \ll B_0 \tag{5.97}$$

$$= -\frac{\gamma^3}{|\gamma|}\,\frac{R^2\,E}{c^2}\,\frac{\partial B_x}{\partial x}\,\frac{\omega_r}{\omega_r - \omega_0}\,. \tag{5.98}$$

This expression can be used to extract the shift in frequency that is linear in E, by canceling out shifts common to the two field settings. A false EDM signal can be extracted as

$$d_{\mathrm{GP}} = -\frac{\hbar}{2}\,\frac{\left\langle \Delta\omega^{(\uparrow\uparrow)}\right\rangle - \left\langle \Delta\omega^{(\uparrow\downarrow)}\right\rangle}{2\,E}\,, \tag{5.99}$$

where the averaging should be done over the particle velocity distribution. For a fixed particle speed, the frequency shift difference can be averaged over the two possible directions of rotation, which are equally likely, to obtain a value for the false EDM as a function of speed. Noting that the rotating field $B_r^{(\uparrow\uparrow)} \to B_r^{(\uparrow\downarrow)}$ for $\omega_r \to -\omega_r$, the averaged frequency shift from equation 5.97 becomes

$$\left\langle \Delta\omega^{(\uparrow\uparrow)}\right\rangle - \left\langle \Delta\omega^{(\uparrow\downarrow)}\right\rangle \simeq -\frac{1}{2}\,\frac{\gamma^3}{|\gamma|}\left[\frac{1}{\omega_r - \omega_0}\,\frac{(B_r^{(\uparrow\uparrow)})^2 - (B_r^{(\uparrow\downarrow)})^2}{2} + \right. \tag{5.100}$$

$$\left. - \frac{1}{\omega_r + \omega_0}\,\frac{(B_r^{(\uparrow\downarrow)})^2 - (B_r^{(\uparrow\uparrow)})^2}{2}\right] \tag{5.101}$$

$$= -\frac{\gamma^3}{|\gamma|}\,\frac{(B_r^{(\uparrow\uparrow)})^2 - (B_r^{(\uparrow\downarrow)})^2}{2}\,\frac{\omega_r}{\omega_r^2 - \omega_0^2} \tag{5.102}$$

$$= -\frac{\gamma^3}{|\gamma|}\,\frac{R^2\,E}{c^2}\,\frac{\partial B_x}{\partial x}\,\frac{\omega_r^2}{\omega_r^2 - \omega_0^2} \tag{5.103}$$

$$= \frac{\gamma}{|\gamma|}\,\frac{v_\perp^2\,E}{B_0^2\,c^2}\,\frac{\partial B_x}{\partial x}\left[1 - \frac{\omega_r^2}{\omega_0^2}\right]^{-1} \tag{5.104}$$

This expression corresponds to equation (19) in [31]. The false EDM can be computed from

equation 5.99 to be

$$d_{\mathrm{GP}} \simeq \frac{\gamma^3}{|\gamma|}\,\frac{\hbar}{8\,E}\,\frac{\omega_r}{\omega_r^2-\omega_0^2}\,\left[\left(B_r^{(\uparrow\uparrow)}\right)^2-\left(B_r^{(\uparrow\downarrow)}\right)^2\right] \tag{5.105}$$

$$= \frac{\gamma^3}{|\gamma|}\,\frac{\hbar}{4\,c^2}\,\frac{\omega_r^2\,R^2}{\omega_r^2-\omega_0^2}\,\frac{\partial B_x}{\partial x} \tag{5.106}$$

In Section 5.5, the motional spin relaxation was introduced, an effect present even in the case of perfectly uniform E and B fields. This is not the case for the systematic geometric phase effect, since no phase will be accumulated when precessing in uniform $B+E$ fields. This can be shown by noticing that if the alignment of the E field to the reference B field is the only variable changing, then a simple flip in the direction of motion will result in the same motional B_v field. If the motional field is the only perturbing field, and assuming that paths have equal probability, the frequency shift cancels out. In a circular orbit, the only rotating field would be the motional field and a flip in the electric field polarization does not change the magnitude or the frequency of the rotating field. Although spins will precess to different orientations if the E field is inverted in the uniform fields case, the total phase accumulated with respect to the axis aligned with B_0 and E will be identical for two particles that follow the same path, so that any angle between the spins will be due only to off-plane components, in a completely symmetrical way. This has also been verified in simulations.

5.6.2 Geometric phase extraction

In the Monte Carlo simulations, the geometric phase can be extracted by tracking an ensemble of spin vectors, measuring the phase at the end of a long period T of free precession in the test fields and comparing the result to the expected phase given a reference field B_0. In these simulations, the spins are started polarized perpendicular to the reference field, so that

$$\boldsymbol{\sigma_0}\cdot\boldsymbol{B_0}=0\,, \tag{5.107}$$

with $\boldsymbol{\sigma_0}$ representing the spin vector at time $t=0$. In the real experiment this is achieved using a $\pi/2$-pulse in order to rotate the particle spins, which start out aligned with B_0, into the precession plane. The phase accumulated after a period of precession T can be computed up to modulo 2π by comparing the spin vectors $\boldsymbol{\sigma}$ at the end of the simulations

with their starting orientations. The phase ϕ is then related by

$$\sin\phi = \frac{\boldsymbol{B_0}\cdot(\boldsymbol{\sigma_0}\times\boldsymbol{\sigma})}{B_0\ |\boldsymbol{\sigma}_\perp|} \tag{5.108}$$

$$= \frac{\boldsymbol{B_0}\cdot(\boldsymbol{\sigma_0}\times\boldsymbol{\sigma})}{\sqrt{B_0^2-(\boldsymbol{\sigma}\cdot\boldsymbol{B_0})^2}} \tag{5.109}$$

$$\cos\phi = \frac{\boldsymbol{\sigma_0}\cdot\boldsymbol{\sigma}}{|\boldsymbol{\sigma}_\perp|} \tag{5.110}$$

$$= \frac{B_0\ (\boldsymbol{\sigma_0}\cdot\boldsymbol{\sigma})}{\sqrt{B_0^2-(\boldsymbol{\sigma}\cdot\boldsymbol{B_0})^2}} \tag{5.111}$$

where the normalizing term $|\boldsymbol{\sigma}_\perp|$ represents the magnitude of the spin projection on the precessing plane and is used to ensure the unit magnitude of the vectors in the expressions. Since each particle spin at the end of the precession period is compared directly to the spin that the particle had at the start, the initial phase is removed so that the initial spin ensemble can be chosen to be uniformly distributed in the precession plane in order to avoid any spurious effects from starting the spins in one orientation rather than another.

As mentioned in section 5.1.1, two simulations can be run with the same seed for the random number generator, but for which the field configuration is different. It is then possible to run two simulation runs, identical but for the E field pointing in opposite directions, so that the effect of the $v\times E$ motional field can be examined for each particle. This has the advantage of partly separating the geometric phase effect from the transverse spin relaxation. In fact, the transverse relaxation of a spin ensemble broadens the width of the accumulated phase signal, as described in section 5.3.2, resulting in uncertainty in the phase measurement. By comparing the accumulated phase pair-wise for particles that have gone through the same path, but with different electric field orientations, the geometric contribution of the geometric phase can be extracted using equation 5.108 to compute the frequency difference

$$\Delta\omega^{\uparrow\uparrow}-\Delta\omega^{\uparrow\downarrow} = \frac{\Delta\phi(T)}{T} = \sin^{-1}\left[\frac{\boldsymbol{B_0}\cdot\left(\boldsymbol{\sigma}^{\uparrow\downarrow}\times\boldsymbol{\sigma}^{\uparrow\uparrow}\right)}{\sqrt{B_0^2-(\boldsymbol{\sigma}^{\uparrow\downarrow}\cdot\boldsymbol{B_0})^2}\sqrt{B_0^2-(\boldsymbol{\sigma}^{\uparrow\uparrow}\cdot\boldsymbol{B_0})^2}}\right] \tag{5.112}$$

after a period T of precession. In this form, $\boldsymbol{\sigma}^{\uparrow\uparrow}$ and $\boldsymbol{\sigma}^{\uparrow\downarrow}$ represent the spin vectors for the respective aligned and anti-aligned $B+E$ field combinations. The cross product ensures that an accumulated positive phase difference represents a counter-clockwise rotation in the

plane of precession.

The frequency shift usually varies for each individual particle path simulated. In fact, for small frequency shifts, some of the particles would gain phase angle during the precession, while others would lose it, and only the average phase shift would be non-zero. Moreover, the extracted value would be the same whether analyzing the particle phase pair-wise or as two ensembles. The difference is in the narrowing of the phase measurement. For example, if a simulation run includes a sizable gradient in the same direction of the field, such as $\partial B_x/\partial x$ for a field B_0 aligned with x, then, two particles which spend a different amount of time in two halves of the cells with respect to x, will be exposed to two different average magnitudes of the B field, and, apart from other effects, they will precess at different frequencies. If the phase from these two particles is averaged, the spread in phase will add to the uncertainty when the false EDM is extracted, as only the average value will contribute. On the other hand, if both of these simulated particles are compared directly to corresponding particles under different E field settings, the difference in precession frequency will cancel out.

In order to get a sensible result from the geometric phase simulations the period of precession needs to be long enough for the diffusion processes to well randomize the motion of the particles. A few seconds is usually all it takes to sample the space. In addition, the period should be long enough to separate the effects of spin relaxation, which broaden the phase distribution as

$$\sigma_\phi \propto \sqrt{T}\,, \tag{5.113}$$

while the systematic shift in frequency should scale linearly in time. A precession period $T \approx 500$ s was used for the simulation of geometric phase.

5.6.2.1 Theoretical formalism

The shift in frequency introduced by the geometric phase effect for particles whose motion is confined to a measurement trap has been studied by [31, 75, 90–92], for different geometries and diffusion considerations, developing a theoretical framework that can be used to estimate the effect for the *nEDM* experiment. The theoretical approach relies on the use of correlation functions to compute the systematic frequency shift proportional to E. Small field components that are perpendicular to $B_0\,\hat{x}$ introduce transverse rotation frequencies noted by $\omega_i = -\gamma\,B_i$ for $i = y,\, z$. It is shown in [90] that a shift in Larmor precession

frequency can be expressed by

$$\delta\omega(\Delta t) = -\frac{1}{2}\int_0^{\Delta t} \mathrm{d}\tau \left\langle \cos\omega_0\tau \times \left[\omega_y(t)\omega_z(t-\tau) - \omega_y(t-\tau)\omega_z(t)\right] \right. \tag{5.114}$$

$$\left. + \sin\omega_0\tau \times \left[\omega_y(t)\omega_z(t-\tau) + \omega_z(t)\omega_z(t-\tau)\right] \right\rangle , \tag{5.115}$$

where an averaging over the spin ensemble is present in the integrand that can be computed from the correlation functions. For the geometric phase, the transverse fields of interest are given by interference between the motional $v \times E$ field, whose components were given by equation 5.69, and the gradient of the B field. These can be expressed as

$$\omega_y = -\gamma \left(\frac{\partial B_y}{\partial y}\, y - \frac{E}{c^2}\, v_z \right) \tag{5.116}$$

$$\omega_z = -\gamma \left(\frac{\partial B_z}{\partial z}\, z + \frac{E}{c^2}\, v_y \right) . \tag{5.117}$$

The expression for a shift in frequency due to the interaction of a gradient and the motional $v \times E$ field is adapted from the formalism found in [93], where the expression $\Delta\Omega_E$ of equation (1) is the shift in frequency linear in E. The difference of frequencies is twice that quantity

$$\Delta\omega^{\uparrow\uparrow} - \Delta\omega^{\uparrow\downarrow} = -\frac{\gamma^2 E}{c^2} \left[\frac{\partial B_y}{\partial y}\, S_y(\omega_0) + \frac{\partial B_z}{\partial z}\, S_z(\omega_0) \right] , \tag{5.118}$$

where $S_i(\omega)$ is the spectrum of the velocity autocorrelation function, defined as

$$S_i(\omega) = \int_0^{\infty} \mathrm{d}t\, \cos(\omega\, t)\, R_i(t)\,, \tag{5.119}$$

where the velocity correlation function has been used in

$$R_i(t) = 2 \int_0^t \mathrm{d}\tau\, \langle v_i(t)\, v_i(t-\tau) \rangle\ . \tag{5.120}$$

The expression for the spectrum is found by [75] and is valid for situations in which collisions affect the motion of the particles in the cell. It is is evaluated for motion in one

dimension L_i in [93] to be

$$S_i(\omega_0) = \frac{L_i^2}{4} \sum_{m=-\infty}^{\infty} \frac{1}{\pi^2\,(m+1/2)^2} \frac{\left(\frac{\omega_0\,L_i}{2\,v_i}\right)^2 - \pi^2\,(m+1/2)^2}{\left[\left(\frac{\omega_0\,L_i}{2\,v_i}\right)^2 - \pi^2\,(m+1/2)^2\right]^2 + \frac{\omega_0^2\,L_i^4}{16\,v_i^2\lambda^2}} \tag{5.121}$$

where λ is the mean free path of diffusion. If the motion is collision free and reflections from the walls of a measurement cell are specular, the mean free path $\lambda \to \infty$ and

$$\lim_{\lambda\to\infty} S_i(\omega_0) = \frac{L_i^2}{4} \sum_{m=-\infty}^{\infty} \frac{1}{\pi^2\,(m+1/2)^2} \frac{1}{\left(\frac{\omega_0\,L_i}{2\,v_i}\right)^2 - \pi^2\,(m+1/2)^2} \tag{5.122}$$

$$= \frac{v_i^2}{\omega_0^2} \left[1 - \frac{2\,v_i}{\omega_0\,L_i}\,\tan\left(\frac{\omega_0\,L_i}{2\,v_i}\right)\right], \tag{5.123}$$

where the infinite series has been reduced using Mathematica [94]. The presence of the tangent in the expression accounts for the many resonances in the spectrum of equation 5.122. This expression can be combined with 5.118 to produce

$$\Delta\omega^{\uparrow\uparrow} - \Delta\omega^{\uparrow\downarrow} = -\frac{2\,E}{B_0^2\,c^2} \left[v_y^2\,\frac{\partial B_y}{\partial y} + v_z^2\,\frac{\partial B_z}{\partial z} + v_y^2\,\frac{\tan(\omega_0\,\Delta t_z)}{\omega_0\,\Delta t_z} + v_z^2\,\frac{\tan(\omega_0\,\Delta t_z)}{\omega_0\,\Delta t_z}\right], \tag{5.124}$$

where the time intervals $\Delta t_y = L_y/2\,v_y$ and $\Delta t_z = L_z/2\,v_z$ were introduced. An additional factor of 2 was included in 5.124, which differs from the formalism of [93]. The modified expression agrees with the Monte Carlo simulation data for the difference in frequencies extracted using equation 5.112, as shown below. In addition, the first two terms of equation 5.124 are present in the expression for particles traveling at constant speed without wall collisions, as described in section 5.6.1.2 validating the need for the extra factor.

The spectrum of equation 5.123 has been used to compute the expected frequency shift described by equation 5.118 and compared to simulation data obtained for motion of UCN in a 2-dimensional representation of the *nEDM* measurement cells. In this simulation, the particles are constrained to move on the $y-z$ plane perpendicular to the direction of the magnetic and electric fields and bounce with specular reflections on a rectangular boundary ($10.2 \times 40\,\mathrm{cm}^2$). The spectra are computed for the two possible directions of motion. The motion is characterized by the ratio of the velocity components, which stays constant, up to a sign, after specular reflections from the rectangular walls. The characteristic time factors L_i/v_i in equation 5.123 are constant in both directions for paths that have the same slope.

The velocity can be defined as

$$\begin{pmatrix} v_y \\ v_z \end{pmatrix} = \begin{pmatrix} v\,\cos\phi \\ v\,\sin\phi \end{pmatrix} \tag{5.125}$$

so that the spectra S_y and S_z can be defined in terms of ϕ, and an expression for the geometric phase frequency shift can be found from equation 5.118 with dependence on the velocity v and angle ϕ. Figures 5.10 and 5.11 show the geometric phase for motion in 2 dimensions in a holding field of $B_0 = 10\,\mathrm{mG}$, for different UCN velocities and magnetic field gradient symmetries. Figures 5.12 and 5.13 show the same for a field of $B_0 = 30\,\mathrm{mG}$. The analytical formalism agrees well with the simulation data as the resonances in the spectrum are dominated by reflections from opposite walls. Additional features that appear in the simulation data are due to the repetitive nature of paths that are closed. These paths occur when the velocity components are such that the particles traverse integer numbers of cell lengths in the same time so that

$$\frac{|v_y|}{n\,L_y} = \frac{|v_z|}{m\,L_z} \qquad\qquad \mathrm{m,\ n} \in \mathbb{N}\,. \tag{5.126}$$

Figure 5.14 shows results for UCN in 3 dimensions with diffuse wall reflections.

In order to compute the geometric phase for ^{3}He atoms in the cell, the formalism of equation 5.121 can be averaged over the velocity distribution of the ^{3}He atoms. The atoms are moving in a superfluid Helium bath kept at a temperature $T < 1$ K, and the distribution of velocities will follow a Maxwell-Boltzmann distribution as seen in equation 5.19. For velocity components perpendicular to the direction of the E field, the relation

$$\left\langle v_i^2 \right\rangle = \frac{1}{3}\,\left\langle v^2 \right\rangle \tag{5.127}$$

was used to compute an effective spectrum

$$\langle S_i(\omega_0) \rangle = \frac{4}{\sqrt{\pi}\,v_{mp}^3} \int_0^\infty \mathrm{d}v\, S_i(\omega_0,\, v/\sqrt{3})\;\, v^2\, e^{-v^2/v_{mp}^2} \tag{5.128}$$

where v_{mp}, the most probable velocity depends on temperature T according to equation 5.20. The mean free path λ changes by many orders of magnitude with the temperature of the bath, as the mean time between interactions with phonons is given by equation 5.24

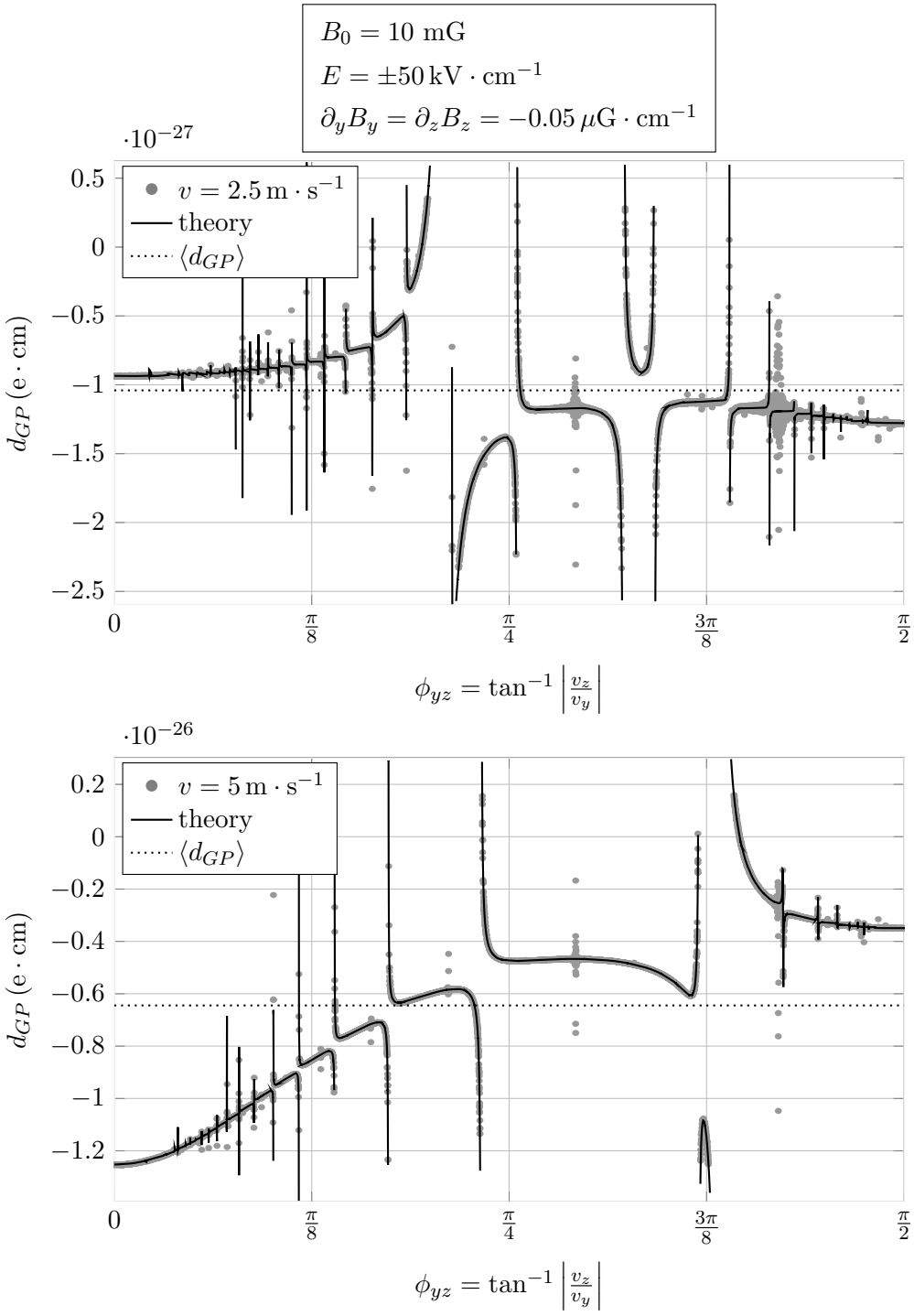

Figure 5.10: Geometric phase simulation results for UCN moving at constant velocity and with specular wall reflections in a 2-dimensional rectangular boundary. The data are plotted as a function of the angle between the velocity components. A symmetric magnetic field gradient $\partial_y B_y = \partial_z B_z$ permeates the cell. The analytical curve reflects the formalism of equation 5.124 and agrees with the simulation data. Most of the resonances present in the simulation data are accounted for by the analytical formula but additional features stand out that are due to motion on closed paths in the rectangle.

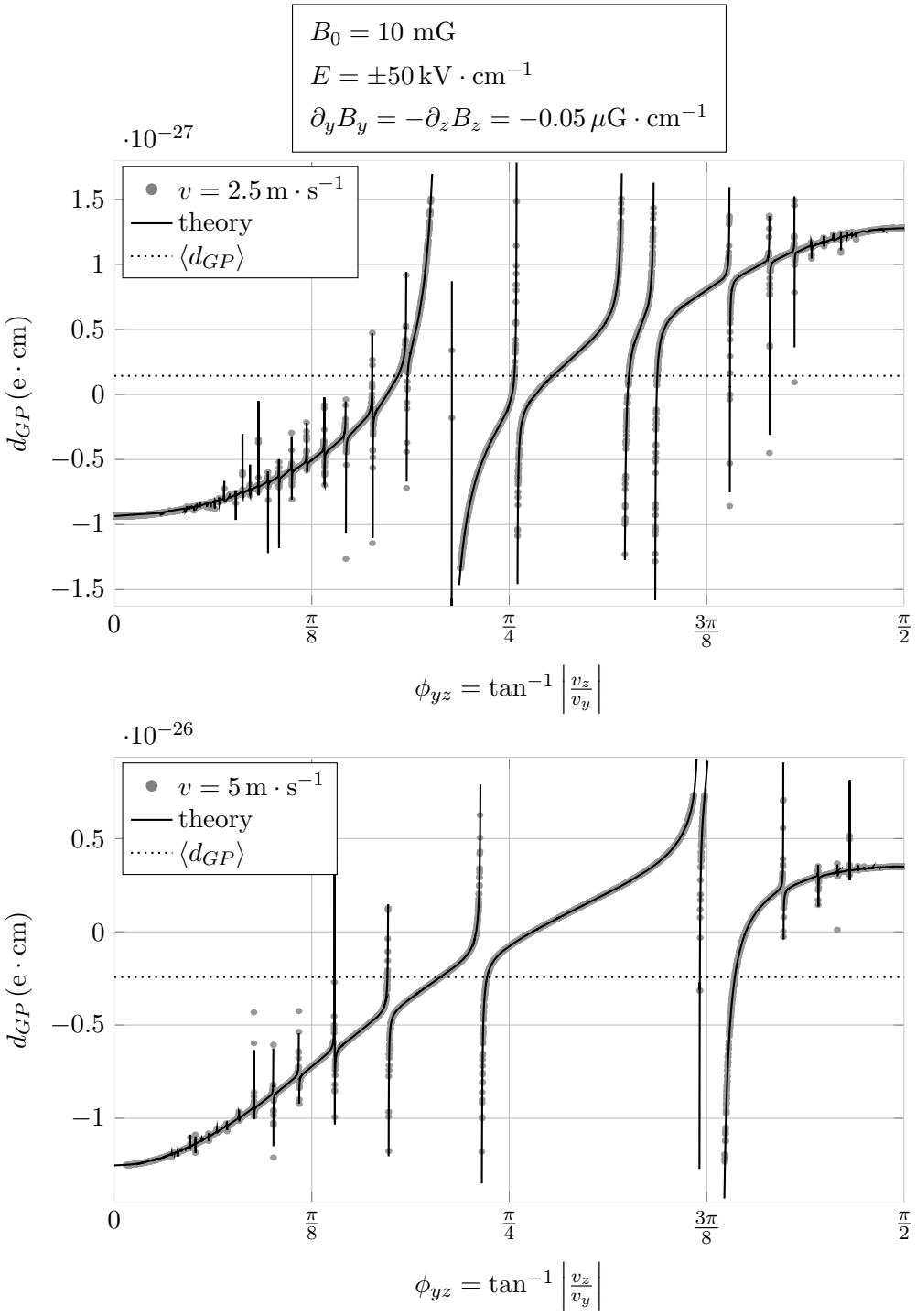

Figure 5.11: Geometric phase simulation results for UCN moving at constant velocity and with specular wall reflections in a 2-dimensional rectangular boundary. The data are plotted as a function of the angle between the velocity components. An anti-symmetric magnetic field gradient $\partial_y B_y = -\partial_z B_z$ permeates the cell. The analytical curve reflects the formalism of equation 5.124.

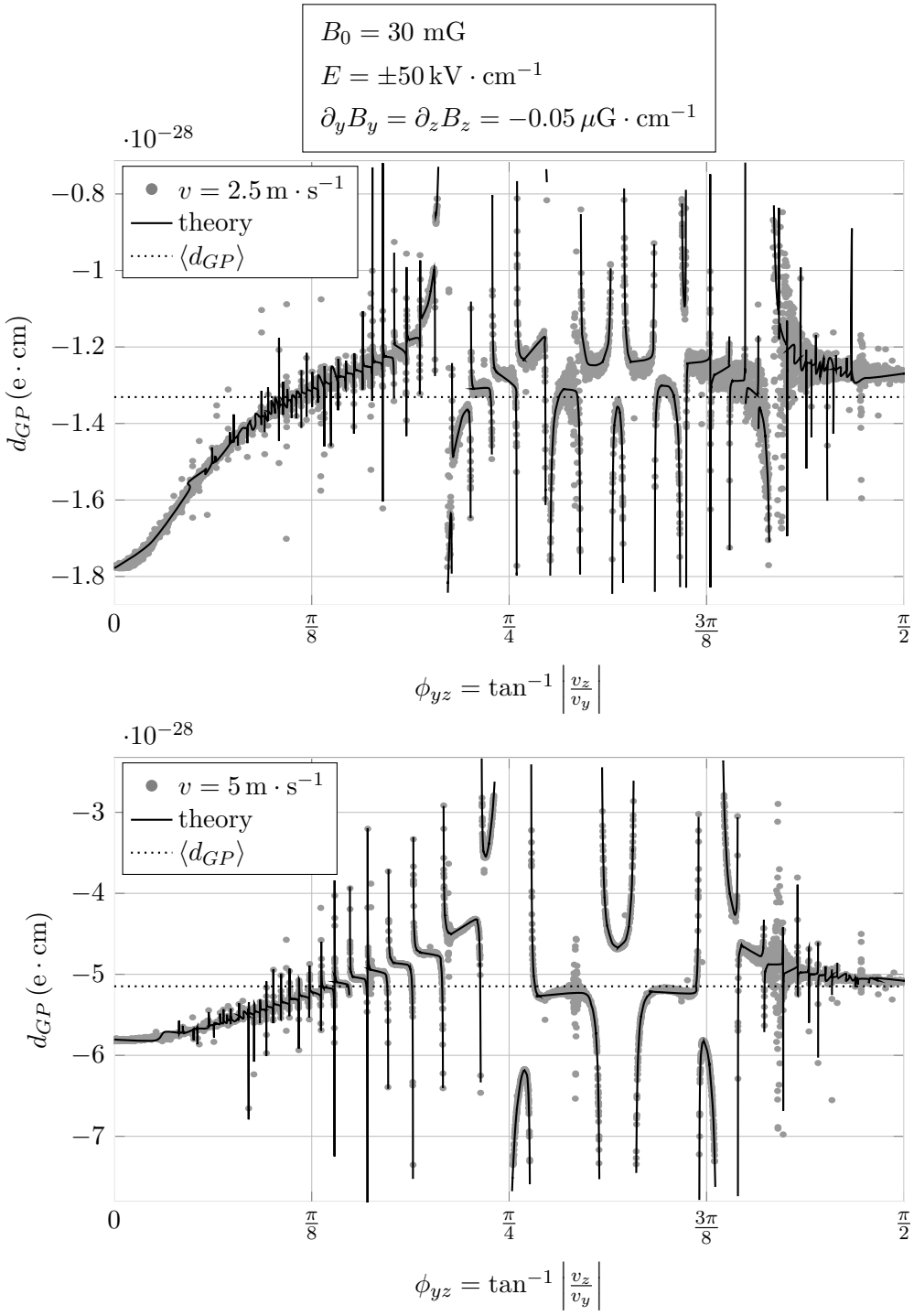

Figure 5.12: Geometric phase simulation results for UCN moving at constant velocity and with specular wall reflections in a 2-dimensional rectangular boundary. The data are plotted as a function of the angle between the velocity components. A symmetric magnetic field gradient $\partial_y B_y = \partial_z B_z$ permeates the cell. The analytical curve reflects the formalism of equation 5.124 and agrees with the simulation data. Most of the resonances present in the simulation data are accounted for by the analytical formula but additional features stand out that are due to motion on closed paths in the rectangle.

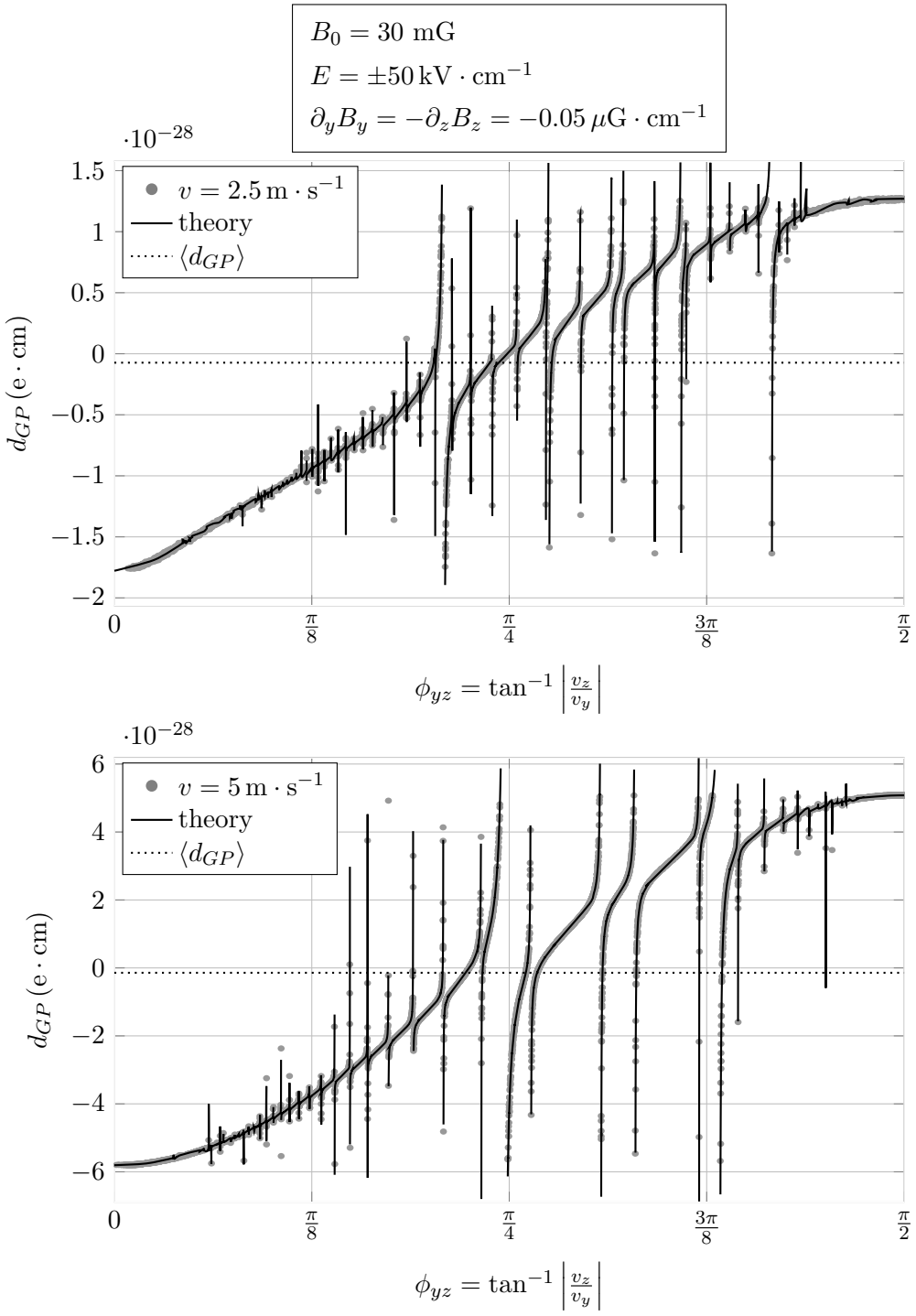

Figure 5.13: Geometric phase simulation results for UCN moving at constant velocity and with specular wall reflections in a 2-dimensional rectangular boundary. The data are plotted as a function of the angle between the velocity components. An anti-symmetric magnetic field gradient $\partial_y B_y = -\partial_z B_z$ permeates the cell. The analytical curve reflects the formalism of equation 5.124.

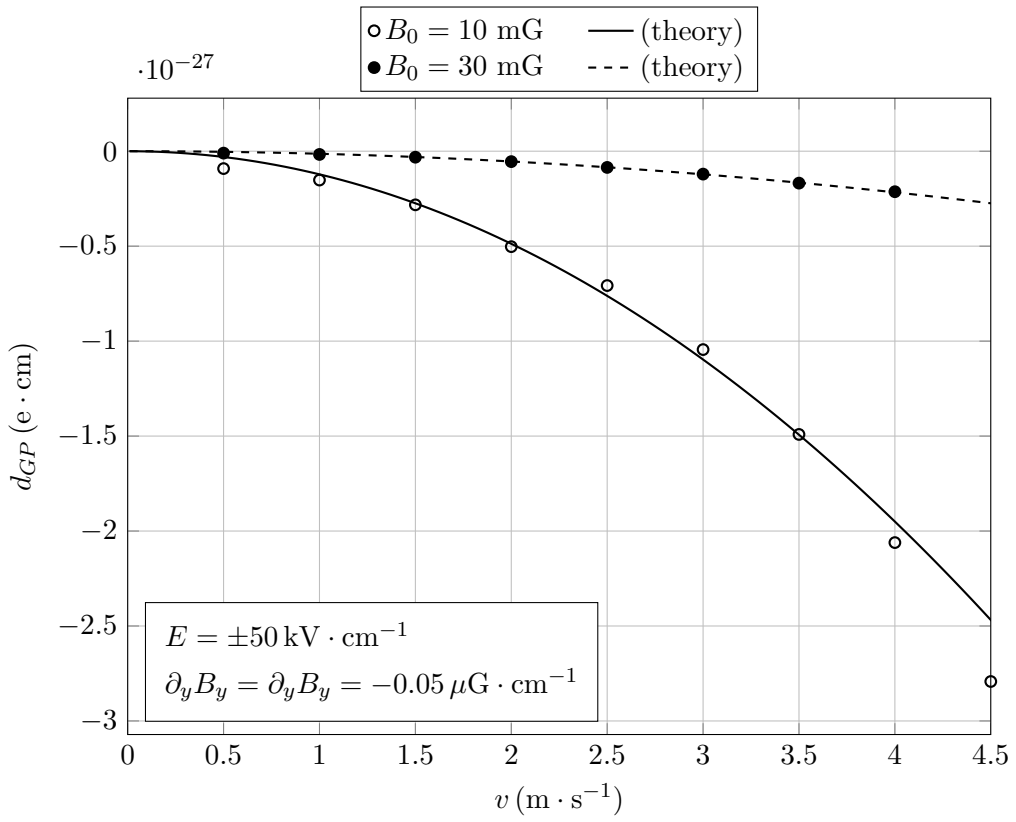

Figure 5.14: Simulation results of the false EDM from geometric phase for UCN in the *nEDM* measurement cell as a function of particle speed. Since the UCN are modeled as mono-energetic, it is useful to restrict the simulations to a single velocity and apply the velocity distribution expected from the UCN production after. The formalism from equation 5.89 is shown for comparison, where the mean perpendicular velocity is approximated to be $v_\perp^2 \simeq 2\left\langle v^2 \right\rangle / 3$.

and is displayed in figure 5.2.

Figures 5.15 and 5.16 show the results of extraction of the false EDM due to geometric phase from simulation of ^{3}He atoms. It is likely that the geometric phase for the UCN system will be smaller than for the ^{3}He system. This is mostly due to the slower speeds at which the UCN move in the cell, and the similarity of the two gyromagnetic ratios.

5.7 $\pi/2$ oscillatory pulse

The oscillatory field used to rotate the spins of both UCN and ^{3}He atoms into the precession plane, the $\pi/2$-pulse, has been modeled in order to optimize the field parameters. In this scenario, spins start aligned with a reference field B_0. A field that is resonating at the Larmor precession frequency of a single species of spin is effective in rotating the spin polarization vector. This is used, for example, in the Ramsey technique of separate oscillatory fields [43] implemented in other free precession measurements [32, 33]. For the *nEDM* measurement, the two species of spins have a similar gyromagnetic ratio $\gamma_3/\gamma_n \simeq 1.11$, so that the pulse of a resonating oscillating field for one of the spins would favor transitions in the other. It is necessary, then, to apply a pulse tuned to rotate both spin species simultaneously into the precessing plane.

The oscillatory field is perpendicular to the holding field B_0, and is parametrized by the oscillation frequency $\omega_{\pi/2}$, its magnitude $B_{\pi/2}$ and duration of the pulse $\tau_{\pi/2}$, so that the total field can be expressed as

$$\boldsymbol{B}(t) = \begin{cases} B_0\,\hat{x} + B_{\pi/2}\,\cos(\omega_{\pi/2}\,t)\;\hat{y} & \text{for } t < \tau_{\pi/2} \\ B_0\,\hat{x} & \text{for } t \geq \tau_{\pi/2} \end{cases} , \tag{5.129}$$

where an additional phase $\phi_{\pi/2}$ can be added to the cosine term. This field can be separated into a clockwise and a counter-clockwise rotating components

$$\boldsymbol{B}(t) = \begin{pmatrix} B_0 \\ 0 \\ 0 \end{pmatrix} + \frac{B_{\pi/2}}{2} \begin{pmatrix} 0 \\ \cos(\omega_{\pi/2}\,t) \\ \sin(\omega_{\pi/2}\,t) \end{pmatrix} + \frac{B_{\pi/2}}{2} \begin{pmatrix} 0 \\ \cos(\omega_{\pi/2}\,t) \\ -\sin(\omega_{\pi/2}\,t) \end{pmatrix} , \tag{5.130}$$

which, in a frame rotating at $\omega_{\pi/2}$ appear as a stationary field and a field rotating at $-2\,\omega_{\pi/2}$.

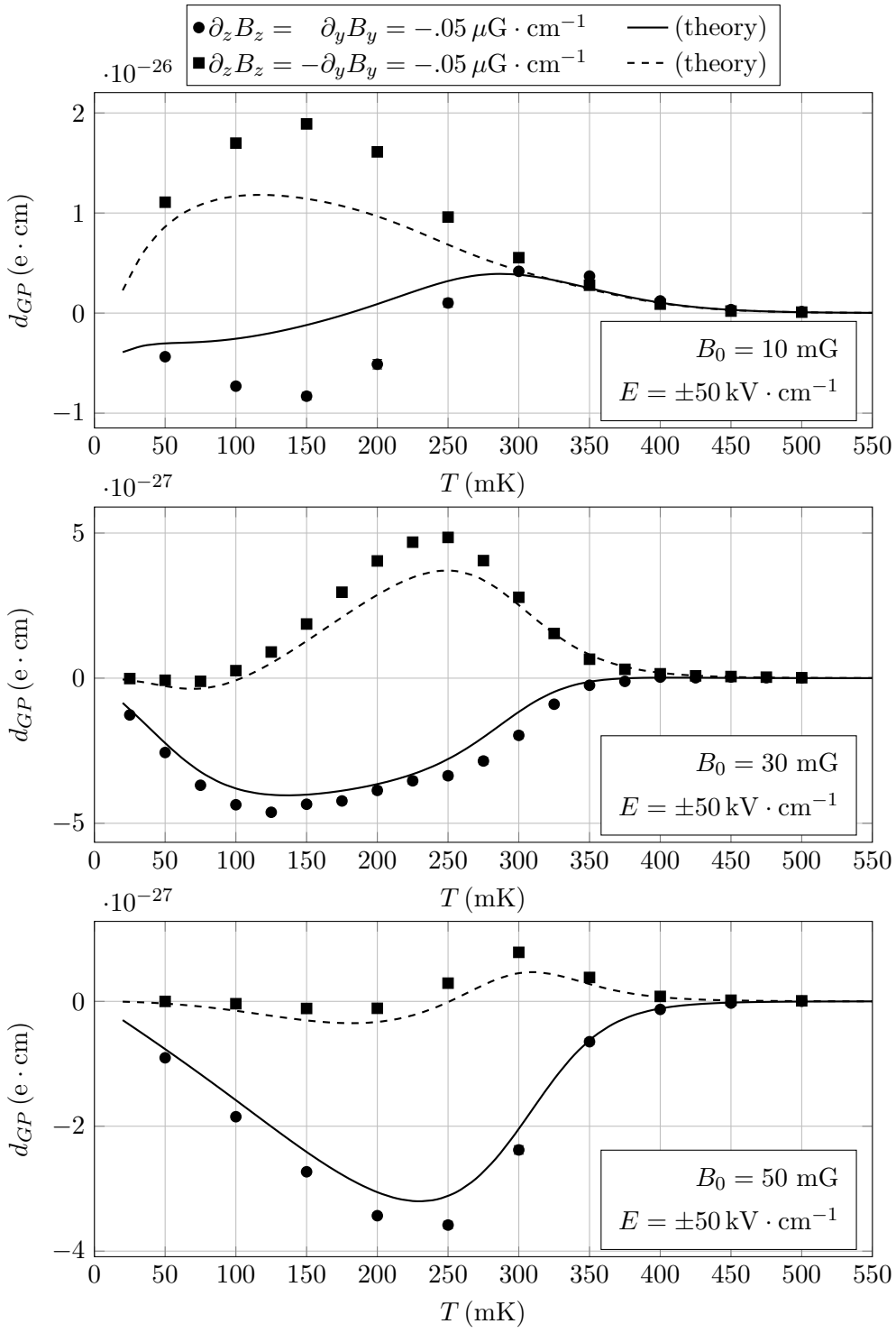

Figure 5.15: Simulation results of false EDM from geometric phase studies for ^{3}He atoms in the *nEDM* measurement cell as a function of bath temperature. The false EDM signal is extracted from the frequency difference between settings with E field aligned and anti-aligned to the reference field B_0. Symmetric and anti-symmetric gradients are compared for different holding field values. The results are compared to expected values using the formalism of equation 5.121. See figure 5.16 for a detail of the higher temperature region of this plot.

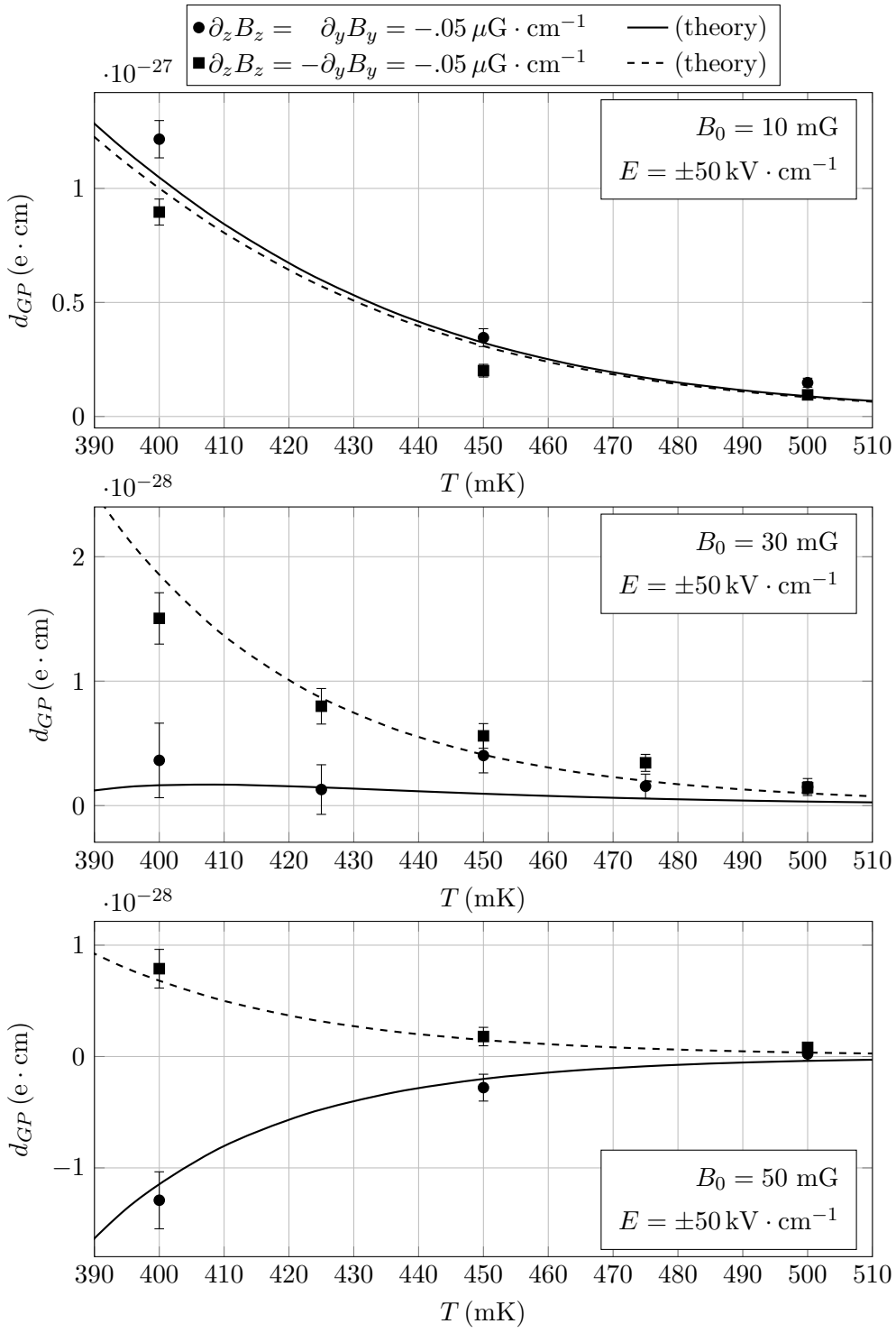

Figure 5.16: Detail of simulation results of false EDM from geometric phase studies for ^{3}He atoms in the *nEDM* measurement cell as a function of bath temperature. Shown here is the temperature range of interest for the *nEDM* measurement, while figure 5.15 shows lower temperatures. The false EDM signal is extracted from the frequency difference between settings with E field aligned and anti-aligned to the reference field B_0. Symmetric and anti-symmetric gradients are compared for different holding field values. The results are compared to expected values using the formalism of equation 5.121.

If the rapidly rotating field is ignored in the rotating frame the expression for the field is

$$\boldsymbol{B'}(t) \simeq \left(B_0 + \frac{\omega_{\pi/2}}{\gamma_s} \right) \hat{x} + \frac{B_{\pi/2}}{2} \hat{y} \,, \tag{5.131}$$

where γ_s represents the gyromagnetic ratio of the species of spin and an assumption has been made that spins precess with a frequency $\omega = -\gamma_s B_0$, so that the apparent field reduces the value of B_0 in a frame co-rotating with the spin precession about B_0. Since the gyromagnetic ratios of the two species differ, the B_0 field cannot be effectively canceled in a rotating frame for both species, so a partial component of the field aligned in $\hat{x}$ will be present for one or both species, depending on the frequency of the rotating frame. One possibility is to make the field in $\hat{x}$, in the rotating frame, the same magnitude but pointing in opposite directions for the two species, by picking

$$\omega_{\pi/2} = -2 B_0 \frac{\gamma_n \gamma_3}{\gamma_n + \gamma_3} \,. \tag{5.132}$$

Another possibility is to make the Larmor frequency due to the field in $\hat{x}$ the same, using the mean gyroscopic ratio

$$\omega_{\pi/2} = -B_0 \bar{\gamma} = -B_0 \frac{\gamma_n + \gamma_3}{2} \,, \tag{5.133}$$

the average frequency of the two spin species. There are other possible frequencies that can be used, and each configuration is a specific combination of the parameters $B_{\pi/2}$, $\omega_{\pi/2}$ and $\tau_{\pi/2}$.

In general, the field $B_{\pi/2}$ must be large enough to be able to rotate the polarization by at least $\pi/2$. In the rotating frame, this means that it must have a magnitude greater than the effective reference field perpendicular to it, resulting in the conditions

$$B_{\pi/2} \geq 2 \left| B_0 + \frac{\omega_{\pi/2}}{\gamma_s} \right| \,, \tag{5.134}$$

for both spin species s. In addition, the spins must end up in the precessing plane at the same time right after the $\pi/2$-pulse is over, so the time $\tau_{\pi/2}$ must be chosen to satisfy

$$\hat{\boldsymbol{x}} \cdot \boldsymbol{\sigma_s}(\tau_{\pi/2}) = 0 \,. \tag{5.135}$$

Using equation 5.7 to compute the spin precession about the total field B' in the rotating frame, as in equation 5.131 with $\boldsymbol{\sigma}_0 = \hat{x}$, the conditions for the spins to be in the precession plane at the same time are

$$\frac{1}{(B'_s)^2}\left[\left(\frac{B_{\pi/2}}{2}\right)^2 \cos(\gamma_s\, B'_s\, \tau_{\pi/2}) + \left(B_0 + \frac{\omega_{\pi/2}}{\gamma_s}\right)^2\right] = 0 \tag{5.136}$$

for both species of spin, where B'_s is the magnitude of the total magnetic field in the rotating frame as in equation 5.131.

A possible solution using the frequency $\omega_{\pi/2}$ as in equation 5.132 results in a condition

$$B_{\pi/2} = 2\, B_0\, \frac{\gamma_3 - \gamma_n}{\gamma_3 + \gamma_n} \tag{5.137}$$

$$\simeq 0.107\, B_0\,, \tag{5.138}$$

where equation 5.134 has been used, and the minimum field value is chosen so that the spins spend a longer time in the precession plane. Since, in this setting, the fields in the rotating frame are symmetric, the conditions of equation 5.136 become

$$\cos\left(\gamma_s\, \frac{\sqrt{2}\, B_{\pi/2}}{2}\, \tau_{\pi/2}\right) = 0\,, \tag{5.139}$$

for each spin species s. There is no exact solution for this set of equations, and the first time that both spins are simultaneously a few thousandths of a radian away from the precession plane is for $B_{\pi/2} \cdot \tau_{\pi/2} \simeq 12.97\,\mathrm{mG}\cdot\mathrm{s}$, which for a field $B_0 = 30$ mG, constraining the magnitude of $B_{\pi/2}$ per equation 5.137 to a value $B_{\pi/2} \simeq 3.18$ mG, results in a period of the $\pi/2$-pulse of $\tau_{\pi/2} \simeq 4$ seconds. This long period can be reduced if the parameters are allowed to be adjusted, allowing, for example, larger values of the oscillating field than the constraint of equation 5.137 that can be found numerically. Furthermore, since this solution has been found with an oscillating field approximated as a rotating field, a numerical approach should be taken to find the best parameter combination. Table 5.2 shows a sample of the parameters that have been found by numerical optimization and can be used for an effective $\pi/2$-pulse.

Figure 5.17 shows the effect of the application of a $\pi/2$-pulse to both species of spins initially aligned to B_0 and the $\hat{x}$ axis. Since the frequency of the oscillating field is not at resonance, some oscillations of the spin polarization are noticeable.

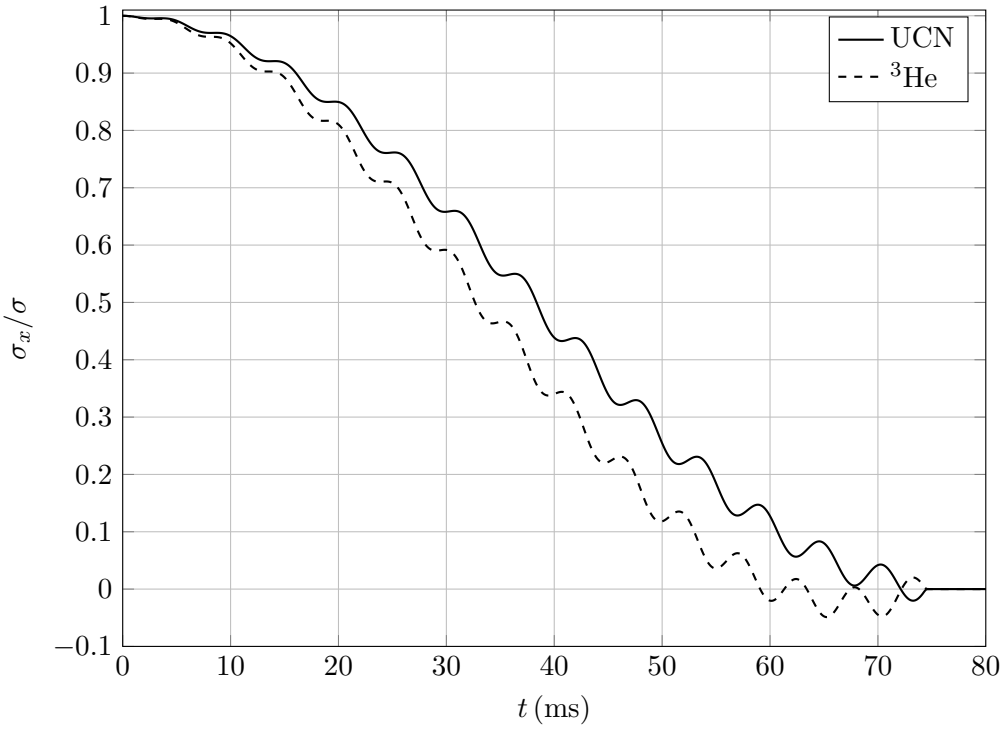

Figure 5.17: Spin polarization under the influence of a $\pi/2$-pulse oscillatory field, as calculated for a holding field of $B_0 = 30$ mG. The polarizations for both spin species start aligned with the B_0 holding field at the start of the pulse ($t = 0$) and rotate with some oscillations into the precession plane during the duration of the pulse $\tau_{\pi/2} \simeq 74.459$ ms. The frequency of the pulse $\omega_{\pi/2} \simeq 578.92658$ has been chosen to reflect equation 5.132. The magnitude of the pulse field is $B_{\pi/2} \simeq 3.220$ mG. The oscillations of the polarization are due to the operation of the $\pi/2$-pulse off resonance. The spins also appear to overshoot the precession plane during their rotation and only end up precessing in it if the pulse is turned off at the right time.

$\omega_{\pi/2}$ solution	$\omega_{\pi/2}/B_0$	$B_{\pi/2}/B_0$	$\frac{\bar{\gamma}\,B_0}{2\,\pi}\,\tau_{\pi/2}$
$-B_0\,\gamma_n$	-0.9469 $\bar{\gamma}$	0.308	8.518
$-B_0\,\frac{2\,\gamma_3\,\gamma_n}{\gamma_3+\gamma_n}$	-0.9972 $\bar{\gamma}$	0.107	6.668
$-B_0\,\frac{\gamma_3+\gamma_n}{2}$	-1.0000 $\bar{\gamma}$	0.134	7.474
$-B_0\,\gamma_3$	-1.0531 $\bar{\gamma}$	0.345	6.813

Table 5.2: Sample of parameters for the oscillating $\pi/2$-pulse numerically optimized to bring the spins of both UCN and ^{3}He atoms within 1/1000 of a radian in the precession plane. Different solutions for the pulse frequency have been modeled, where the frequency is fixed on the exact solution, while the pulse magnitude $B_{\pi/2}$ and duration $\tau_{\pi/2}$ are optimized numerically. All quantities are expressed in terms of the reference field B_0 and the mean gyromagnetic ratio $\bar{\gamma}$, and the pulse duration is expressed in the number of precessions that a spin with gyromagnetic ratio $\bar{\gamma}$ would complete about the B_0 field. Note that solutions exist for the $\pi/2$-pulse frequencies that match the Larmor resonant frequency of either spin species.

5.7.1 Ramsey separated oscillatory fields

As discussed in section 2.3.2.3, the frequency of the $\pi/2$ pulse can be kept coherent with the spin precession of ^{3}He atoms during a measurement of an *nEDM* run. The $\pi/2$-pulse can then be used to return the ^{3}He polarization back to the original orientation with respect to B_0, so that an accurate phase measurement of the accumulated precession phase of the ^{3}He spin ensemble can be performed. This would be similar to a Ramsey measurement using separate oscillatory fields [43], where the polarization at the end of the second oscillatory pulse depends highly on the phase accumulated during a long period of free precession. The polarization of the ^{3}He in the *nEDM* experiment could be measured by allowing some polarized UCN to enter the cell, and measuring the capture rate.

Because the $\pi/2$-pulse is designed to simultaneously turn two species of spins into the plane of precession, only specific combinations of parameters can be used, so varying the frequency of the oscillating field will result in worse precession plane alignment for the EDM measurement. One parameter that can be varied is the measurement period T of free precession, which does not affect the initial spin alignment. By varying T by a small amount, the phase of the ^{3}He spins with respect to the $\pi/2$ oscillating field grows as the

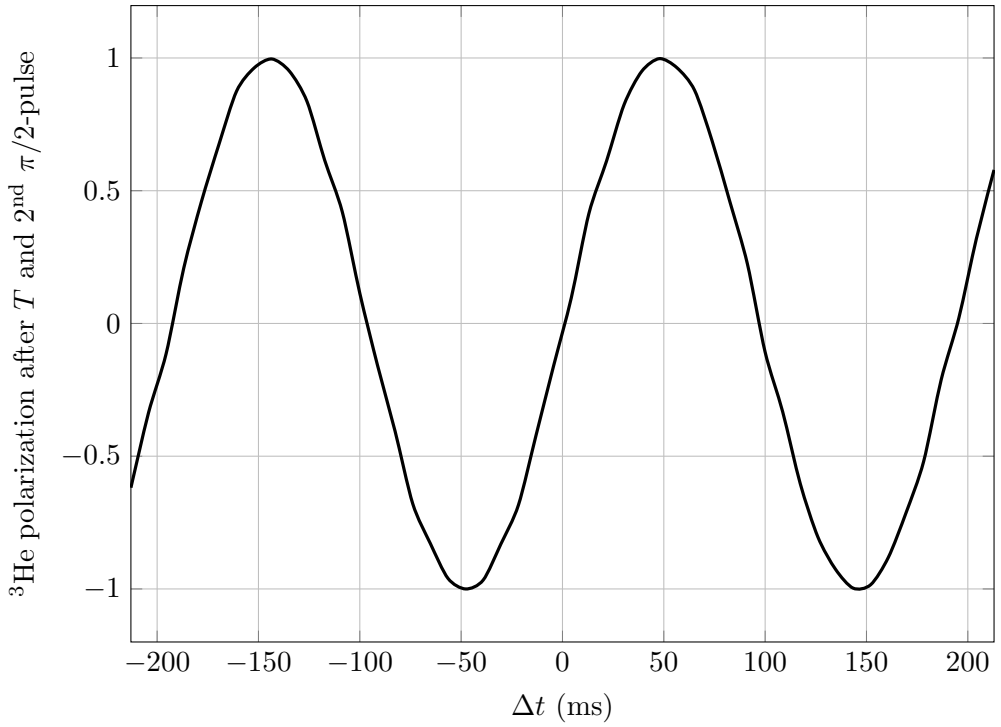

Figure 5.18: Example of the measurement of the ^{3}He polarization after a long period $T \simeq 500$ s of free precession in EDM measurement. The value of the polarization of ^{3}He spin ensemble is obtained by pulsing the $\pi/2$ field a second time after a long period $T + \Delta t$, so that the accumulated phase can be measured. The value T has been chosen so that a pulsing of the $\pi/2$ field will leave the ^{3}He spins in the precession plane, so that varying Δt will have the highest resolution.

difference in their frequencies, resulting in a period of oscillation of

$$T_{beat} = \frac{2\,\pi}{-\gamma_3\,B_0 - \omega_{\pi/2}}\,, \tag{5.140}$$

after which the ^{3}He spin ensemble will have precessed one full cycle more than the oscillating field. The ^{3}He polarization after the second $\pi/2$-pulse depends on this phase difference so that two EDM measurements can be operated with two measurement times differing by a small $\Delta T < T_{beat}$ to compare the accumulated phase across the runs. A field of $B_0 = 30$ mG and a frequency $\omega_{\pi/2}$ as in equation 5.132 results in $T_{beat} \simeq 0.19$ s. Figure 5.18 shows how the polarization after a second $\pi/2$-pulse varies with different measurement times. Figure 5.19 shows how the separate oscillatory fields technique can be used to measure the effective magnetic field strength.

The ^{3}He polarization can be measured by allowing polarized neutrons into the measure-

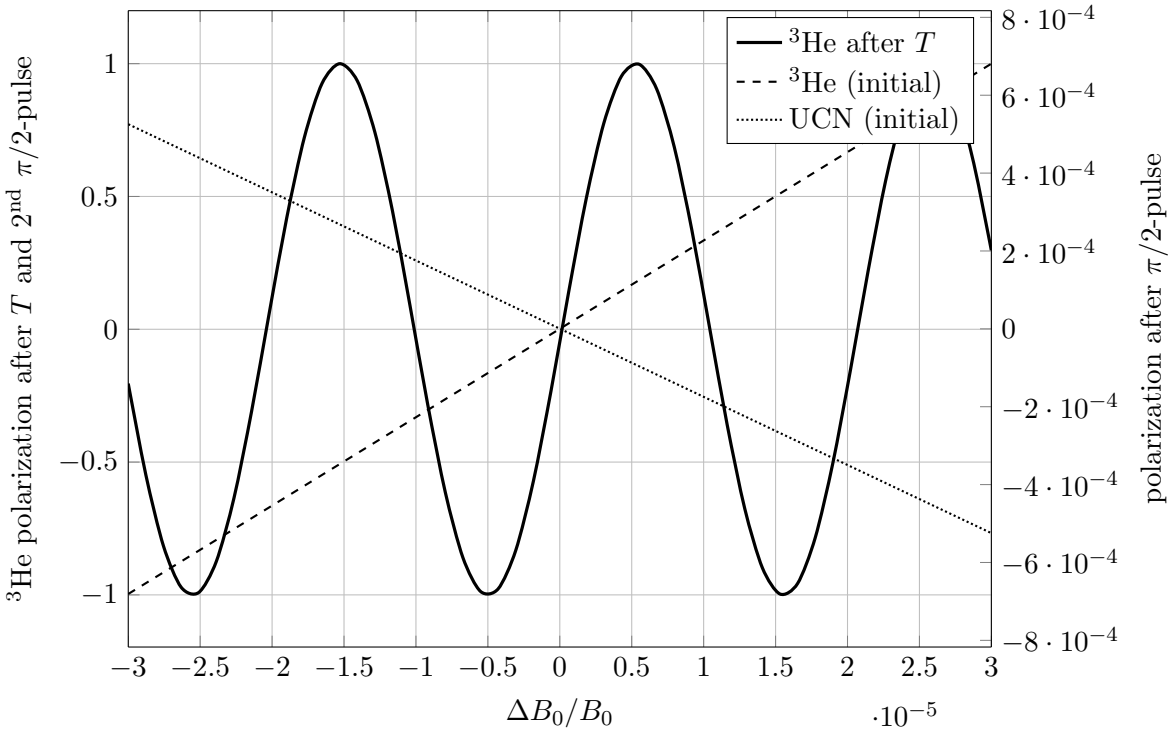

Figure 5.19: Example of the measurement of the ^{3}He polarization after a long period $T \simeq 500$ s of free precession in EDM measurement. The right axis shows the polarization of UCN and ^{3}He spins right after the $\pi/2$-pulse rotates them into the precession plane ($P = 0$). The left axis shows the polarization of ^{3}He spin ensemble, obtained by pulsing the $\pi/2$ field a second time after a period T, so that the accumulated phase can be measured. The quantities are plotted as a function of deviations of the holding field B_0 and the period T of free precession is chosen so that the polarization after the second pulse nearly vanishes, resulting in the highest resolution for changes in B_0. Note that small deviations in B_0 have a small effect on the effectiveness of the $\pi/2$-pulse to rotate both spins into the precession plane (right axis).

ment cells after the second $\pi/2$-pulse and observing the capture signal. The UCN population during filling can be expressed as

$$N_{\mathrm{UCN}}(t) = \frac{P_{\mathrm{UCN}}}{\Gamma_3 + \Gamma_\beta + \Gamma_{loss}} \left(1 - e^{-(\Gamma_3+\Gamma_\beta+\Gamma_{loss})\,t}\right) , \tag{5.141}$$

with $P_{\mathrm{UCN}}/V \simeq 0.25\,\mathrm{s}^{-1}\,\mathrm{cm}^{-3}$ representing the production of UCN in superfluid Helium, and the other quantities given by table 5.3. The effective capture of neutrons on ^{3}He atoms

	rate (Hz)	description
Γ_3	$2 \cdot 10^{-3}$	n-^{3}He capture rate
Γ_β	$1.13 \cdot 10^{-3}$	neutron β decay rate
Γ_{loss}	$8.3 \cdot 10^{-4}$	trap lifetime of ≈ 1200 s
P_{UCN}	780	UCN production in a single cell

Table 5.3: UCN production and losses for the *nEDM* experiment. [35]

depends on the relative alignment of the spins so it should be replaced by

$$\Gamma_3'(\theta) = \Gamma_3\,(1 - \cos\theta)\,, \tag{5.142}$$

where θ is the angle between the spin vectors. During the initial fill (≈ 1000 s) at the beginning of a EDM measurement run, the polarizations of the neutrons and ^{3}He atoms is aligned, so that the capture rate is small. A counting measurement at the end of the period T of free precession would occur with a significant rate of capture, where $\theta \simeq \pi/2$. A simple counting measurement for a fixed fill time T_{fill} would result in a number of events measured given by

$$N_{meas}(\theta) = \int_0^{T_{fill}} \mathrm{d}t\,\Gamma'(\theta)\,N_{\mathrm{UCN}}(t) \tag{5.143}$$

$$= \frac{\Gamma'(\theta)\,P_{\mathrm{UCN}}}{\Gamma_3(\theta) + \Gamma_\beta + \Gamma_{loss}} \left(T_{fill} - \frac{1 - e^{-(\Gamma_3(\theta)+\Gamma_\beta+\Gamma_{loss})\,T_{fill}}}{\Gamma_3(\theta) + \Gamma_\beta + \Gamma_{loss}}\right) , \tag{5.144}$$

where the signal rate has been represented by $\Gamma'(\theta) \simeq \Gamma_3(\theta)$ to denote that detector efficiency, proper identification of capture events and background signals can modify this quantity. If no identification of capture events is performed, neutron β-decay events will contribute to the measured number. A statistically significant discrepancy from expectation in the measured event count can be attributed to an accumulation of phase during the

period of free precession, which is related to a discrepancy in the known holding field B_0. Using a fill time $T_{fill} \simeq 120$ s, the expected event count for $\theta = \pi/2$, including a contribution of $\simeq 25\%$ from neutron decay is $N_{meas} \simeq 11,000$, resulting in a statistical noise of $\sigma(N_{meas}) \simeq 100$, or 1%. A shift in phase of $\Delta\phi \simeq 2 \times 10^{-2}$ would increase (or decrease) this number by $\Delta N \simeq 200$, so that the discrepancy would be visible. Over a measurement period $T \simeq 500$ s, this would be equivalent to measuring a frequency difference $\Delta\nu \simeq 40\,\mu$Hz.

The implementation of a phase measurement at the end of an EDM run would serve to augment the frequency measurement obtained from the SQUID signal during the run. From the proposal [35] estimate of the sensitivity of the SQUID measurement, the ^{3}He frequency should be known to $26\,\mu$Hz for the measurement period of 500 s. Since the uncertainty of the SQUID frequency measurement is proportional to $\delta\nu \propto 1/\sqrt{T^3}$, it could be advantageous to keep the ^{3}He spins in the precession plane, instead of exposing them to the second $\pi/2$-pulse, and continuing the SQUID measurement for the additional ~ 100 s of fill time.

5.8 Dressed spin simulations

The spin dressing technique introduced in section 2.3.2.2 has been implemented in the Monte Carlo simulations. The dressing field oscillates at a frequency $\omega_{\rm rf} \simeq 3000$ kHz with an amplitude $B_{\rm rf} \simeq 1.3$ Gauss. In the simulations the numerical integration of the spin equations of motion adapts the time step to the large field and fast oscillations, resulting in slower simulations than for the cases studied above. From the analysis of the runs, the mean time step in the simulations was found to be $\Delta t \approx 0.5\,\mu$s and this quantity is approximately 1/500 of the Larmor period of precession about the large $B_{\rm rf}$ field. This results in long computation times, with the computing wall-clock time being a factor of ~ 30 longer than the simulated run time. A single set of dressed spin simulation runs can require CPU usage equivalent to a week.

A set of Monte Carlo simulations was run to address the question of spin relaxation in an inhomogeneous dressing field. In particular, addressing whether the addition of active shielding of the dressing field, as introduced in section 3.3.1, affects the relaxation times. As seen in figure 3.9, the field along the longer side of the measurement cell is expected to become less uniform with the implementation of an active shield.

The formalism of McGregor [82] can be adapted to compute the expected T_2 relaxation times for the case of the spin dressing. As described in [34, 91], the deviations in the dressing field can be associated with deviations of the effective gyromagnetic ratio of the dressing parameter. The dressing parameter of equation 2.20 changes with the dressing field magnitude $B_{\rm rf}$ so that

$$\Delta X_s = \frac{\gamma_s}{\omega_{\rm rf}} \Delta B_{\rm rf} \,, \tag{5.145}$$

and since the effective gyromagnetic ratio γ_s^{eff} is given by equation 2.19, the changes in dressing field magnitude will result in

$$\Delta\gamma_s^{eff} = \frac{\gamma_s^2}{\omega_{\rm rf}} J_1\left(X_s\right) \Delta B_{\rm rf} \,. \tag{5.146}$$

The deviations in the effective gyromagnetic ratio result in a spread of precession frequencies which is akin to the dephasing process of transverse spin relaxation T_2. In particular, the relation of equation 5.50 can be used to compute the relaxation by noting that

$$\Delta\omega = \gamma\,\Delta B + \Delta\gamma\, B \tag{5.147}$$

so that the second term on the right hand side can be related to the first, relating the changes in the gyromagnetic ratio to deviations in the static field B_0

$$\Delta B_0 = \frac{\Delta\gamma_s^{eff}}{\gamma_s^{eff}} B_0 = \frac{\gamma_s\, B_0}{\omega_{\rm rf}} \frac{J_1(X_s)}{J_0(X_s)} \,. \tag{5.148}$$

The formalism of McGregor of equation 5.48 can be used to compute the transverse spin relaxation to be

$$\frac{1}{T_2} \simeq \frac{1}{120} \frac{\gamma_s^2\, L^4}{D} \frac{\gamma_s^2\, B_0^2}{\omega_{\rm rf}^2} \left[J_1(X_s)\right]^2 \left(\frac{\partial B_x}{\partial z}\right)^2 \,, \tag{5.149}$$

where the effective gyromagnetic ratio was substituted and only the major contributing term to the relaxation is included.

A small set of simulations of the spin relaxation due to a non-uniform dressing field have been carried out for ^{3}He at a temperatures near 450 mK. The distortion of the field expected from the active shielding of the dressing field introduces a large deviation of the field in the measurement cells. The gradient of relevance was calculated [95] from the coil

model introduced in section 3.3.1 to be

$$\frac{\partial B_{\mathrm{rf}}}{\partial z}_{\mathrm{RMS}} \simeq 3.2 \times 10^{-4}\,\mathrm{G}\cdot\mathrm{cm}^{-1}\,, \tag{5.150}$$

with a quadratic profile, so that the field in z is symmetric about the center of the cell and the considerations of section 5.3.2.1 should be implemented. The resulting relaxation times are on the order of $T_2 \sim 400$ s, for a temperature $T = 450$ mK. Dressed spin simulations have been shown to agree with this value. This is necessarily too small for the planned measurement, and the development of correction coils was necessary to restore some uniformity to the field. This is discussed in section 3.3.3. The correction coils reduce the gradient by a factor of 10, leading to much better relaxation times $T_2 \gtrsim 10^4$ s. Figure 5.20 shows a small set of simulation results for the dressed spin relaxation.

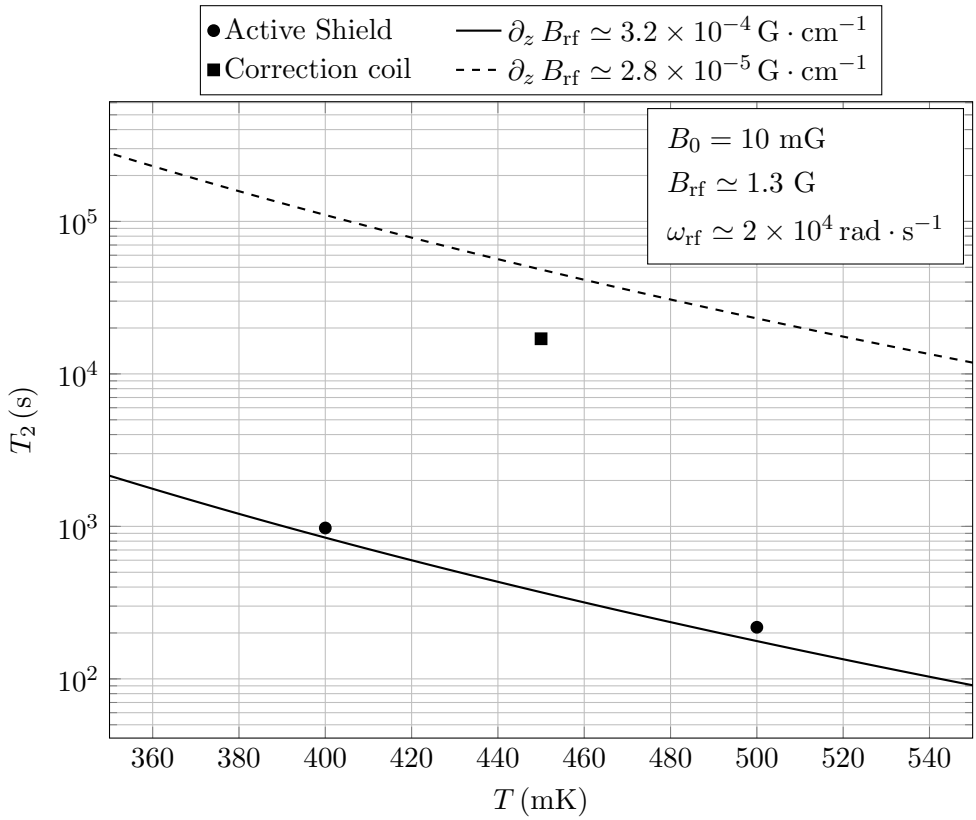

Figure 5.20: Transverse (T_2) dressed spin relaxation times extracted from Monte Carlo simulations for ^{3}He atoms as a function of bath temperature. The large gradient is produced by the distortion to the field that active shielding introduces. The addition of a small correction coil can fix the large gradient and reduce the relaxation rate. The gradient has a quadratic profile, and the model curves are derived from equation 5.149. Only the contribution from the gradient in z is plotted for the model. In the simulation result for the correction coil, the other gradients can contribute to the relaxation, resulting in a lower T_2 than calculated.

Chapter 6

Benchmarking Frequency signal extraction

A collaborative mock-data analysis task was carried out in order to design a suitable unbiased analysis framework for the data that will be acquired in the *nEDM* measurement. A few sets of Monte Carlo data were generated using *GEANT*4 by a collaborator [96] for the purpose. The analysis effort would try to extract an Electric Dipole Moment signal from the data. The motivation for such a task was to demonstrate that a frequency signal could be extracted from the analysis of capture events of neutrons onto ^{3}He, without introducing spurious effects that could be confused with an EDM. A few different analysis methodologies were carried out by other collaborators and were later compared with the known parameters of the Monte Carlo data.

The generated data included the basic signal expected from the measurement of the relative precession frequency of neutrons and ^{3}He spin under the influence of a large electric field alternatively aligned to a reference magnetic field. This technique of measurement is introduced in section 2.3.2.1.

In this chapter a particular unbinned analysis method is outlined. It is found to be consistent with other strategies and particularly convenient for the type of data expected from an Electric Dipole Moment signal.

The numerical minimization tools provided by the MINUIT package, which are also implemented in the ROOT analysis framework, prove useful to fitting for the rate parameter using a likelihood.

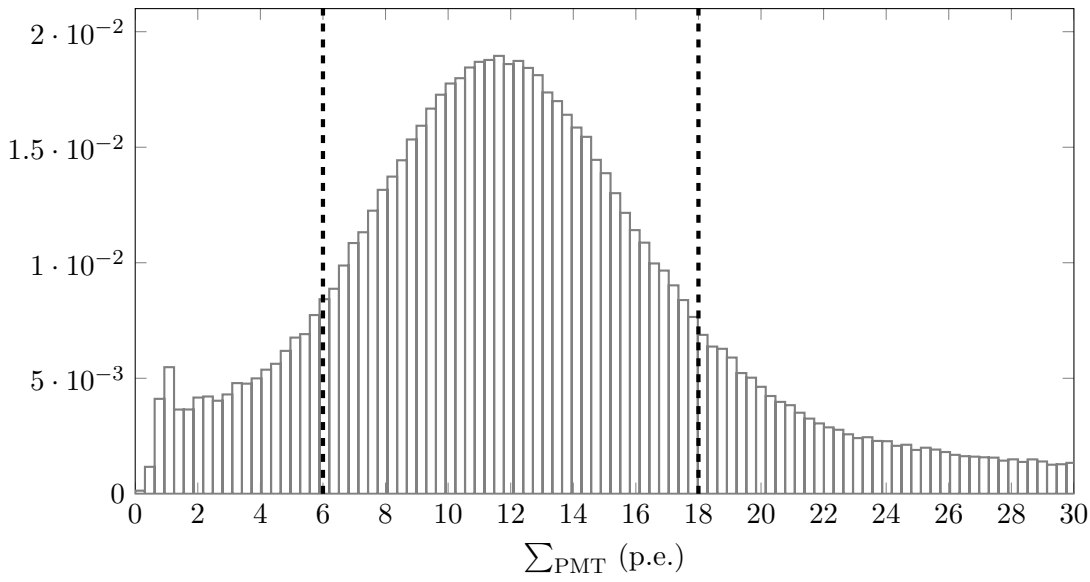

Figure 6.1: The photomultiplier spectrum for capture events in a single measurement cell with focus on the peak ~ 12 due to n-^{3}He capture events. The dashed black line shows the cut on photo-electrons used in the analysis.

6.1 Mock-data analysis

The Monte Carlo generated data consist of the response in number of photo-electrons of 8 photomultiplier tubes (PMT) attached via light guides to the cells, as well as the adjusted arrival time of the signal. Events can be identified as originating from a particular measurement cell by looking at which set of 4 PMTs has been triggered. The largest set of mock-data includes about 10^9 events from 1250 separate runs.

The energy spectrum from photomultiplier response is shown in figure 6.1. On average, the number of photo-electrons generated by n-^{3}He capture is expected to be ~ 12, so it is possible to construct a fiducial cut

$$6 < \sum_{\text{PMT}} < 18 \tag{6.1}$$

to exclude part of the unwanted background events.

The generated signal includes signals from scintillation light from neutron β decay and neutron capture on a ^{3}He nucleus, as well as additional background signals such as cosmic rays passing through the cells and light guides, and radiation from activated regions in the experimental apparatus.

One of the additional concerns motivating this analysis preparation was the possibility of the neutron β-decay asymmetry A [37] introducing effects that would significantly shift the extracted frequency and bias the resulting EDM. Because of this, the generated data included a large asymmetry $|A| \simeq 1$ in order to magnify the possible effect. The asymmetry of the decay introduces an oscillation of the light collected by the PMTs due to the phase of the neutron spin, which is precessing at the Larmor frequency. As expected, the large asymmetry did not bias the extraction of the frequency.

The ^{3}He capture signal oscillates at a beat frequency reflecting the coherent precession of neutrons and ^{3}He spins about the same magnetic field. A small difference in precession frequencies between the two cells represents the input EDM parameter for neutrons under the influence of the alternatively aligned electric field.

At the beginning of the simulation both species of spins are assumed to have gone through some mechanism by which they were rotated so as to precess perpendicular to the magnetic field. One such mechanism is described in section 5.7. This transition period is not included in the mock-data and only the resulting phase accrued from the rotation is considered. The phase is supposed to be constant for all the runs and in the real experimental setup should be known to be repeatable to the 10^{-3} radians level. One of the goals of the mock-data test is to find out how the knowledge of the initial phase would affect the confidence interval on the fit of the EDM signal.

6.2 Likelihood Fit

In order to estimate the input EDM parameter, an analysis using maximum likelihood was used to fit the neutron spin precession frequency relative to the frequency of ^{3}He spins. A statistic is constructed using the formalism described by Cowan in [97] and the parameters of the fit function are estimated. The frequency of oscillation of the capture rate is one of the parameters and it is used in the estimation of the EDM. The frequencies of both cells were studied and fitted separately, whereas the EDM signal could, otherwise, be identified as a shift in frequency between the two cells, for a single run. This would take into account changes in the reference magnetic field B_0 between different runs, affecting both cells equally.

6.2.1 Rate

The expected signal from the *nEDM* measurement is comprised of several sources that eventually produce some number of photon-electrons in the PMTs. The signal of interest to extract an EDM is an Electric field dependent modulation of the n-^{3}He capture rate, as detailed in section 2.3. Although it is possible to identify some of the extraneous sources, some amount of background is expected in the signal.

The rate $\Gamma(t) \geq 0$ is defined as the number of expected events per unit time, so that the expectation value of a measurement that spans the interval T is given by

$$E[N] = \int_T \mathrm{d}t\, \Gamma(t). \tag{6.2}$$

A simple time-varying rate for the signal expected from neutrons can be defined for a single neutron to be

$$\Gamma_n(t) = \Gamma_\beta + \Gamma_3\ [1 - P(t)\cos\phi(t)] \tag{6.3}$$

where Γ_β and Γ_3 are the *effective* rates of signal from β decay and n-^{3}He capture rate respectively. The capture rate depends on the angle ϕ between spin polarizations of the neutron and ^{3}He atoms so that Γ_3 is the capture rate for an unpolarized ensemble, while $2\,\Gamma_3$ would be the maximum capture rate if the two species of spins were polarized and remained anti-aligned. The angle between the two spin species will be modulated as the spin polarizations precess about the same field at different frequencies, as detailed in section 2.3, so that

$$\phi(t) = \omega\, t + \phi_0, \tag{6.4}$$

where ϕ_0 is the initial angle between the two spin polarizations at the beginning of the free precession measurement.

The polarization term $P(t)$ included in equation 6.3 is expected to decrease in time as the effective coherence of the signal decreases due to the spin relaxation processes affecting both spin species and detailed in 5.3. It can be expressed as

$$P(t) = P_0\, e^{-t/T_2} \tag{6.5}$$

where a combined spin-spin relaxation time T_2 is used in the exponential decay of the

coherent signal. The initial polarization P_0 is omitted as a parameter to the fit because of the evident correlation to Γ_β and Γ_3, so that a transformation of parameters can be chosen

$$\Gamma_3' \to P_0\,\Gamma_3 \tag{6.6}$$

$$\Gamma_\beta' \to \Gamma_\beta + (1 - P_0)\,\Gamma_3 \tag{6.7}$$

to fix the initial polarization $P_0 = 1$ and remove it as a degree of freedom.

A generalized version of the rate for the signal in the *nEDM* cells can be described by

$$\Gamma(t) = N(t) \times [\Gamma_\beta + \Gamma_3\,(1 - P(t)\,\cos[\omega\,t + \phi_0])] + \Gamma_B(t), \tag{6.8}$$

where the rate for a single neutron has been multiplied by $N(t)$, the number of *remaining* neutrons in the measurement cell, which should be decreasing exponentially in time. In addition, a background rate Γ_B was added to represent the possible sources of background signal.

6.2.1.1 Neutrons in the cell

The number of neutrons decreases in time via n-^{3}He capture, β decay and losses of neutrons that do not produce signal. When fitting data the exponential decay of the neutron signal can be explicitly added with two fit parameters, so that

$$N(t) = N_0\,e^{-t/\tau_{\text{eff.}}}, \tag{6.9}$$

where N_0 represents the initial number of neutrons and $\tau_{\text{eff.}}$ the effective decay parameter, a combination of the processes that decrease the neutron signal. To first order, the decay parameter is related to the signal rates

$$\frac{1}{\tau_{\text{eff.}}} \simeq \Gamma_\beta + \Gamma_3 + \frac{1}{\tau_{\text{loss}}}, \tag{6.10}$$

but, because the n-^{3}He rate oscillates in time, the decay parameter $\tau_{\text{eff.}}$ will not be a perfect representation of the signal decay rate, although this discrepancy only exists for times short compared to the period of oscillation.

An alternative approach that removes the explicit signal exponential decay and one of

the decay fit parameters, is to set

$$N(t) = N_0 - N_{\text{meas}}(t) \tag{6.11}$$

$$\simeq N_0 - \int_0^t \mathrm{d}t' \, \Gamma_n(t') \tag{6.12}$$

and count the number of neutron events measured N_{meas} before time t during the analysis. If the source of signal comes purely from neutron processes, then, each event measured decreases the total neutron number by one and, consequently, the rate by $1/N(t)$. The initial neutron number N_0, in this analysis, is generally closely related to the physical number of neutrons in the cell at the beginning of the measurement run, but is more specifically defined as the maximum number of neutrons that could be observed by running the measurement for a sufficiently long time, given the experimental circumstances of the measurement, such as losses, detection efficiency, background and more. For example, N_0 would change value if a cut was performed on a data set.

If the signal contains a non-neutron source, as is the case with any background in equation 6.8, each individual measurement cannot be assumed to decrease the number of available neutrons by exactly 1 because once in a while a background event is expected. This discrepancy can be accounted for if the computed integral of the neutron rate $\Gamma_n(t)$ is used to represent the number of neutrons measured, as it is the case for the form of equation 6.12.

6.2.1.2 Rate as probability

The rate function can be normalized to become a probability density function

$$\rho(t) = \frac{\Gamma(t)}{N_e}, \tag{6.13}$$

where N_e is the expectation value

$$N_e = E[N] = \int_0^T \mathrm{d}t \, \Gamma(t), \tag{6.14}$$

for a measurement of given rate $\Gamma(t)$ and measurement time limited to T.

6.2.2 Maximum Likelihood

The estimation of the fit parameters is performed using the maximum likelihood method with the formalism found in [97]. A likelihood statistic for a set of data can be constructed from a given model, based on the probability that the model describes the data. If the model is parametrized with n parameters expressed in the vector $\boldsymbol{\theta}$, it is understood that the parameters $\hat{\boldsymbol{\theta}}$ that maximize the likelihood are the best estimated fit parameters for the data set. In order to perform a likelihood analysis, an appropriate probability distribution should be used. The probability distribution that describes the statistical outcomes of a counting measurement is given by the Poisson distribution, which is introduced below and applied to this analysis.

6.2.2.1 Poisson Distribution

The Poisson distribution can be used to estimate the likelihood of a particular measurement as originating from a parent distribution function. If a counting measurement is performed, the probability of measuring exactly k events, given that $\lambda = E[k]$ are expected

$$P_k(\lambda) = \frac{\lambda^k \, e^{-\lambda}}{k!}, \tag{6.15}$$

and is defined for non-negative real values of λ and non-negative integer values of k.

The probability distribution is normalized so that the following expressions are true,

$$\sum_{k=0}^{\infty} P_k(\lambda) = 1 \tag{6.16}$$

$$\int_0^{\infty} \mathrm{d}\lambda \, P_k(\lambda) = 1 \tag{6.17}$$

The first condition normalizes all possible measurement outcomes by assuring that for a given value of expected events $\lambda > 0$, a number $k \in \mathbb{N}^0$ events will be measured with finite and normalized probability. Only the special case for which no event is expected, $\lambda = 0$, does not allow any possible measurement outcome except for $k = 0$. The second condition normalizes the expectation value, showing that for a fixed number of measured events k, there is a continuum of expectation values $\lambda \in [0, \infty)$ that could produce the outcome with the Poisson distribution as probability density function in λ.

In addition, the condition 6.17 can be used to draw a probability density function in time if the expected value of the measurement is given by the integral of a rate $\Gamma(t)$ as in equation 6.2. Noting that $\mathrm{d}\lambda = \mathrm{d}t\,\Gamma(t)$, the resulting normalized probability density function of the measurement time t is

$$\rho_k(t) = \Gamma(t)\,\frac{\lambda^k\,e^{-\lambda}}{k!}, \tag{6.18}$$

In this form, the probability is expressed as the probability, per unit time, of measuring exactly k events within time $t + \mathrm{d}t$. This functional form of the Poisson probability is valuable if the rate varies quickly in time and if k is small.

If no events are measured during an interval in time, equation 6.18 reduces to

$$\rho_0(t) = \Gamma(t)\,e^{-\lambda(t)}, \tag{6.19}$$

for $k = 0$. This form represents the probability distribution function of intervals between stochastic events, which is used in the unbinned analysis described in 6.2.4.

6.2.3 Binned likelihood

Given an interval in time Δt, the rate function can be used to compute the number of expected events

$$\lambda = \int_{\Delta t} \mathrm{d}t\,\Gamma(t) \tag{6.20}$$

and if a number k of events is measured, the probability of such occurrence can be calculated using equation 6.15.

A set of data that spans an interval T can be binned in N_{bins} intervals in time, of duration $\Delta t = T/N$ each. The total likelihood of the data set is found by multiplying together the Poisson probabilities of all bin contents

$$\mathcal{L} = \prod_{i=1}^{N_{\mathrm{bins}}} P\left(k_i, \lambda_i\right) = \prod_{i=1}^{N_{\mathrm{bins}}} \frac{\lambda_i^{k_i}\,e^{-\lambda_i}}{k_i!}. \tag{6.21}$$

where k_i is the number of observed events in time bin Δt_i and λ_i the expected number of events for the same bin, which depends on the parameters of the generating rate. The

logarithmic likelihood is useful when dealing with small probabilities

$$\log \mathcal{L} = \sum_{i=1}^{N_{\text{bins}}} \left[k_i \, \log(\lambda_i) - \lambda_i - \log(k_i!) \right]. \tag{6.22}$$

The maximum possible likelihood $\hat{\mathcal{L}}$ for a given binned data set $\boldsymbol{k} = \{k_1, k_2, \ldots, k_N\}$ is found by maximizing the likelihood at each bin

$$\frac{\partial(\log \mathcal{L})}{\partial \lambda_i} \to 0 \qquad \hat{\lambda}_i = k_i, \tag{6.23}$$

and since this quantity depends only on the data set and not on the parameters in the model, it can serve as reference to compare the likelihood obtained from the fit. The maximum likelihood ratio $\Lambda = \mathcal{L}/\hat{\mathcal{L}}$ can be defined to be

$$\log \Lambda = \log \mathcal{L} - \log \hat{\mathcal{L}} = \sum_{i=1}^{N_{\text{bins}}} \left[k_i \, \log\left(\frac{\lambda_i}{k_i}\right) - (\lambda_i - k_i) \right] \tag{6.24}$$

$$= \sum_{i=1}^{N_{\text{bins}}} k_i \log\left(\frac{\lambda_i}{k_i}\right) + N_{\text{obs}} - N_e, \tag{6.25}$$

where N_{obs} is the total number of events observed in all bins and N_e the expectation value of the total number of events.

The maximum likelihood study of a binned data set can be used to search for the best fit parameters $\boldsymbol{\theta}$ of a generating rate $\Gamma(t; \boldsymbol{\theta})$. As the rate parameters vary, the expected number of measured events λ_i in each bin changes thus changing the bin likelihood and the likelihood of the whole data set. The parameters can be varied until the maximum likelihood is reached.

6.2.3.1 Normalization of the fit function

If the parameter space for the model rate $\Gamma(t; \boldsymbol{\theta})$ contains a normalizing constant factor $\theta_{\text{N}} \in \boldsymbol{\theta}$ such that

$$\Gamma(t; \boldsymbol{\theta}) \to \theta_{\text{N}} \, \Gamma'(t; \boldsymbol{\theta'}), \tag{6.26}$$

with $\boldsymbol{\theta'} = \boldsymbol{\theta} - \{\theta_{\rm N}\}$, then the associated likelihood function, equation 6.22, is maximized for

$$\frac{\partial \log \mathcal{L}}{\partial \theta_{\rm N}} = \sum_{i=1}^{N_{\rm bins}} \left[\frac{k_i}{\theta_{\rm N}} - \lambda'_i \right] \to 0, \tag{6.27}$$

so that $\theta_{\rm N} = N_{\rm obs}/N'_e$, the ratio between the number of observed events and the number of events expected from the rate $\Gamma'(t;\, \boldsymbol{\theta'})$ during the measurement period T. The normalization factor does not, then, affect the likelihood of the fit. It is useful to isolate the normalization parameter and compute it in order to simplify and speed up the numerical maximization of the likelihood.

In addition, the fact that the maximed likelihood coincides with the number of events expected equaling the number of events measured is used below in the arguments concerning the unbinned likelihood analysis.

6.2.4 Unbinned likelihood

The arguments in section 6.2.3 should be valid regardless of how a data-set is binned. This is because of the normalization conditions of the Poisson distribution which allow for the likelihood to be correctly computed without bias on the number of expected or observed events. On the other hand, choosing an inappropriate bin size for the data set can hide parameter sensitivity or introduce a bias. If, for example, a parameter such as ω in equation 6.3 defines oscillations in the expected number of events, the size of a bin needs to be small compared to the period of oscillation, otherwise, the oscillations would be hidden within the bin and the sensitivity of the likelihood to ω will be negligible.

Although it is possible to shrink the bin size to increase the sensitivity to oscillations, the number of events per bin can decrease significantly, to the point where most of the bins contain not a single event. If this is the case, the binning is no longer well defined because of the many empty bins, and the number of degrees of freedom of the data set, usually associated with the number of bins, can be misinterpreted and be larger than the total number of events measured. This can bias the estimation of parameter error from the data.

An alternative to using a binned likelihood analysis, that does not suffer from the small event counts and is potentially less biased, is analyzing the data unbinned. The unbinned likelihood is computed for individual events and can be equivalently thought of as the

likelihood of intervals in time between two consecutive events. This follows the probability density function described by equation 6.19. This form, together with the normalizing condition derived from equation 6.27, results in the total log-likelihood function for unbinned events of the form

$$\log \mathcal{L} = \sum_{i=1}^{N} \log \Gamma(t_i; \boldsymbol{\theta}), \tag{6.28}$$

for rate parameters $\boldsymbol{\theta}$, where the rate is evaluated at each time t_i. This is equivalent to binning the events in N bins of variable width given by the interval in time between consecutive events. The probability distribution function derived from the rate in section 6.2.1.2 can be used directly to compute the unbinned likelihood. As expected, the maximum likelihood achieved from the individual events reveals the parameters of the fitting function which most plausibly describe the data. In this case, the number of degrees of freedom is computed from the total number of events measured.

6.2.5 Coverage

The task of fitting a parameter space $\boldsymbol{\theta}$ to data must be linked to the considerations of confidence intervals to determine the significance of the analysis and assign a value of error to the fit parameters. [97–99]. The confidence interval, or coverage probability C, is defined as the fraction of times that the parameter range defined by the estimated parameter, $\hat{\theta}_i$, of a given set of data and the errors on the parameter, contains the true parameter

$$\theta_0 \in [\hat{\theta}_i + \Delta\theta_i^-,\, \hat{\theta}_i + \Delta\theta_i^+], \tag{6.29}$$

where the parameter errors $\Delta\theta_i^{\pm}$ can be calculated. Usually, the errors on the parameter are chosen as to cover a pre-determined fraction C of parameter values.

For example, if a measurement in x is expected to be Gaussian distributed, with the estimated mean value $\hat{x}$ and the known width σ_x, the probability density function is

$$f(x) = \frac{1}{\sqrt{2\pi}\sigma_x} \exp\left[-\frac{(x-\hat{x})^2}{2\,\sigma_x^2}\right], \tag{6.30}$$

so the true parameter x_0 will be $x_0 \in [\hat{x} - n\,\sigma_x,\, \hat{x} + n\,\sigma_x]$ with a probability given by the coverage C. Table 6.1 summarizes the first few confidence levels, as well as the equivalent

log-likelihood difference of the Gaussian measurement x, defined as

$$\Delta \log \mathcal{L} = -\frac{(x-\hat{x})^2}{2\sigma_x^2} = -\frac{1}{2}\left(\frac{\Delta x}{\sigma_x}\right)^2. \tag{6.31}$$

The confidence interval of the Gaussian distribution measurement is given by the width parameter σ_x, the coverage of the range is consistently $C \simeq 68.3\%$ and does not vary with the mean parameter $\hat{x}$ of the measurement.

Δx	$C\,(\%)$	$\Delta \log \mathcal{L}$
$1\,\sigma_x$	68.27	-0.5
$2\,\sigma_x$	95.45	-2
$3\,\sigma_x$	99.73	-4.5

Table 6.1: Coverage C for the normal distribution at a distance of $n\,\sigma_x$ along with the corresponding likelihood difference.

If a measurement obeys the Poisson distribution, the coverage can be computed from the likelihood ratio, $\log \Lambda = \Delta \log \mathcal{L}$, if an appropriate error range is defined. A parallel can be drawn to the Gaussian distribution and a confidence interval can be defined as the range where the likelihood difference is $\Delta \log \mathcal{L} \in [-1/2,\, 0]$ and is expected to have the same coverage as long as the measured value k in the Poisson distribution is large. In fact, if the confidence intervals are calculated from the likelihood difference

$$\Delta \log \mathcal{L}(\Delta\lambda) = k\,\log\left(\frac{k+\Delta\lambda}{k}\right) - \Delta\lambda, \tag{6.32}$$

where $\Delta\lambda = \lambda - k$ represents the distance from the estimated parameter $\hat{\lambda} = k$, and used with the prescription for the likelihood differences of table 6.1, then a range for which the real parameter

$$\lambda_0 \in \left[\hat{\lambda} + \Delta\lambda^-,\, \hat{\lambda} + \Delta\lambda^+\right] \tag{6.33}$$

can be computed. Since measurements in the Poisson distribution assume integer values so that each measured k will be associated to different intervals as seen in table 6.2, the estimated parameter will also be restricted to integer values and the confidence interval cannot be determined by a trivial function of the real parameter λ_0 and must be computed

numerically from

$$C(\lambda_0) = \sum_{k=0}^{\infty} \frac{\lambda_0^k \, e^{-\lambda_0}}{k!} \times \begin{cases} 1 & \text{if } \lambda_0 \in \left[\hat{\lambda}_{\min}, \, \hat{\lambda}_{\max}\right] \\ 0 & \text{otherwise} \end{cases} . \tag{6.34}$$

The result of this calculation is shown in figure 6.2 and is inspired by the figure in [99] of the same. The discontinuities from the discrete observables are evident for small values of λ_0 revealing that the confidence intervals calculated with a fixed interval $\Delta \log \mathcal{L}$ can be affected systematically by the true parameter λ_0. Asymptotically, the coverage for the Poisson distribution confidence intervals approaches the value expected from the intervals found in the Gaussian model, as shown in table 6.1.

k	$\lambda_{\min}$	$\lambda_{\max}$
0	0	0.5
1	0.3	2.36
2	0.9	3.77
3	1.58	5.08
4	2.32	6.35
5	3.08	7.58
6	3.87	8.79

Table 6.2: Confidence intervals for the Poisson distribution of different measured values k, as calculated using equation 6.32 for a value $\Delta \log \mathcal{L} = -1/2$. The intervals define error ranges around the estimated parameter $\hat{\lambda} = k$.

6.2.5.1 Coverage for the unbinned likelihood

The same coverage arguments can be applied to the unbinned likelihood analysis of section 6.2.4. The coverage can be computed from the distribution function of intervals between individual events of equation 6.19. In this case a confidence interval around the best estimator for the rate, $\hat{\Gamma} = 1/\Delta t$, can be defined from the likelihood ratio as

$$\Delta \log \mathcal{L} = \log(\hat{\Gamma} + \Delta\Gamma) - \int_{\Delta t} \mathrm{d}t (\hat{\Gamma} + \Delta\Gamma) - \left(\log \hat{\Gamma} - \int_{\Delta t} \mathrm{d}t \, \hat{\Gamma} \right) \tag{6.35}$$

$$= \log\left(1 + \Delta\Gamma\Delta t\right) - \Delta\Gamma\Delta t \, . \tag{6.36}$$

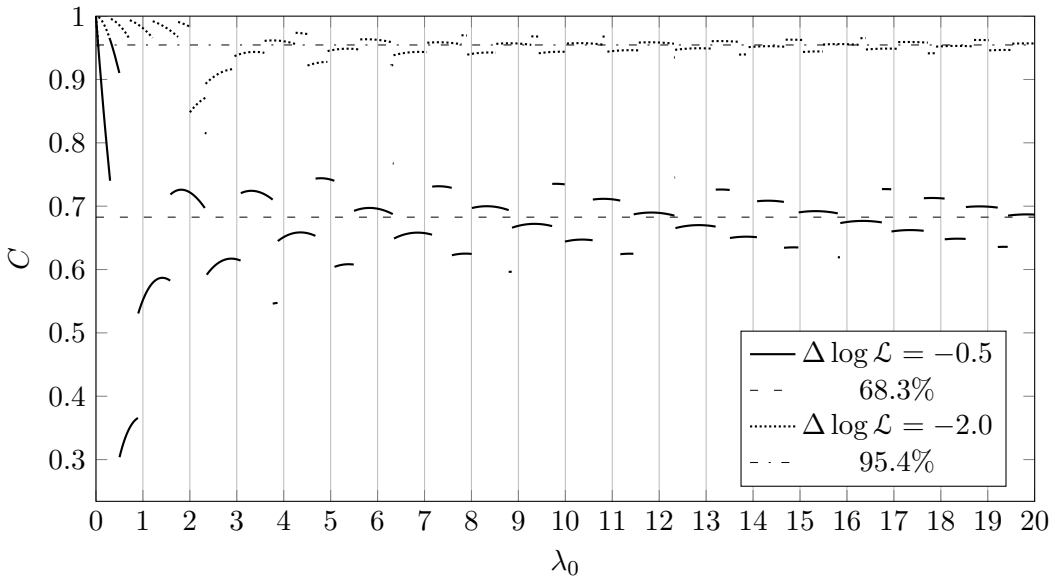

Figure 6.2: Coverage of the confidence intervals of the Poisson distribution as a function of the true parameter λ_0. The intervals are computed using equation 6.32 with the same likelihood intervals, $\Delta \log \mathcal{L}$, set by the Gaussian coverage, summarized in table 6.1

Given a fixed interval of likelihood $\Delta \log \mathcal{L}$, the quantity $x \equiv \Delta\Gamma\, \Delta t$ can be solved for, independently of Γ_0 or Δt. The two solutions $x^{\pm}$ yield the confidence interval in rate

$$\Gamma_0 \in \left[\hat{\Gamma} + \frac{x^-}{\Delta t}, \hat{\Gamma} + \frac{x^+}{\Delta t} \right] . \tag{6.37}$$

This interval can be expressed as a confidence interval in time for which the real rate parameter Γ_0 is contained

$$\Delta t \in \left[\frac{1 + x^-}{\Gamma_0}, \frac{1 + x^+}{\Gamma_0} \right] . \tag{6.38}$$

The coverage can be computed using the intervals in time from the probability distribution function of equation 6.19

$$C = \int_{(1+x^-)/\Gamma_0}^{(1+x^+)/\Gamma_0} \mathrm{d}t\, \Gamma_0 e^{-\Gamma_0 t} = e^{-(1+x^-)} - e^{-(1+x^+)}. \tag{6.39}$$

Because the coverage is not dependent on the real rate parameter Γ_0 but only on the values $x^{\pm}$ that correspond to the choice of $\Delta \log \mathcal{L}$, the desired confidence interval can be obtained by numerical solution. Table 6.3 contains the numerical solutions for the first few likelihood that have the same coverage C as the Gaussian model of table 6.1. The likelihood confidence interval $\Delta \log \mathcal{L}$ can be used when searching for the parameters that maximize the likelihood,

in order to obtain an estimate of the error of the fit parameters. The errors in a parameter are defined from the points in parameter space where the likelihood is $\Delta \log \mathcal{L}$ away from the maximum likelihood that can be found.

x^-	x^+	$C\,(\%)$	$\Delta \log \mathcal{L}$
-0.73	1.5	68.27	-0.584
-0.96	3.88	95.45	-2.293
-1	7.13	99.73	-5.032

Table 6.3: Coverage C of the unbinned likelihood constructed from intervals between consecutive events, numerically computed using equations 6.35 and 6.39, with confidence intervals comparable to the Gaussian counter-parts of table 6.1.

6.3 Goodness of Fit

A goodness of fit test should be performed to determine the statistical significance of the fit. For the case of the method of least squares, where the prior distribution is known or assumed to be Gaussian, the χ^2 statistic offers a solid method to test the fit result. In this case, the likelihood from the Gaussian probability function is used directly [97] to compute

$$\chi^2 = -2 \log \mathcal{L} = \sum_{i=1}^{N} \frac{(x_i - \hat{x})^2}{\sigma_i^2}. \tag{6.40}$$

A similar statistic can be constructed for a counting measurement following the Poisson distribution, which can be used in the analysis of binned data. The likelihood ratio defined in equation 6.24 tests how well the model fits a data set of observed values with respect to the maximum possible likelihood that those observed values could achieve. With the same prescription as equation 6.40, the goodness of fit can be constructed

$$\chi^2 \simeq -2 \log \mathcal{L} = \sum_{i=1}^{N} \left[k_i \log \left(\frac{\lambda_i}{k_i} \right) - (\lambda_i - k_i) \right], \tag{6.41}$$

at least for cases in which the mean value $\lambda \gg 1$, when the Poisson distribution approaches the Gaussian distribution.

For values of λ that are small, the maximum likelihood ratio of a Poisson-distributed sample is not independent of the mean value λ, so equation 6.41 is not a good candidate for a goodness of fit statistic. This can be seen by computing the mean value for the expected

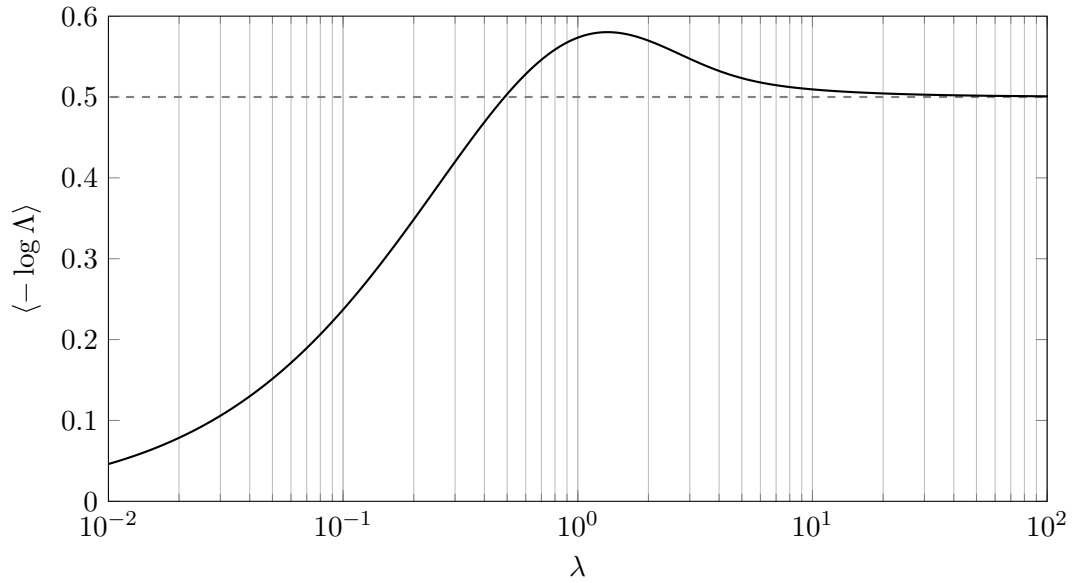

Figure 6.3: Mean log-likelihood ratio expected from Poisson distributed observables, as a function of the expected value λ. For large values of λ, this value agrees with the value of $1/2$ expected from the Gaussian example.

likelihood ratio as

$$\langle -\log \Lambda \rangle = -\sum_{k=0}^{\infty} \frac{\lambda^k\, e^{-\lambda}}{k!} \left[k \log\left(\frac{\lambda}{k}\right) - (\lambda + k) \right], \tag{6.42}$$

the values of which are pictured in figure 6.3, where the asymptotic behavior in $\lambda \to \infty$ agrees well with the value expected from the least square goodness of fit of a Gaussian distributed measurement.

Instead of using the Poisson distribution to compute the goodness of fit of an ensemble of pre-determined fixed width bins, some of which might contain few or no events, it is possible to look at the time between individual events and compute the goodness of fit from the likelihood of those intervals. This is similar to choosing variable bin widths so that each bin contains exactly one event. With the probability distribution function of the intervals between events defined by equation 6.19, and the likelihood ratio of the measurement given by the standard Poisson distribution with fixed $k = 1$, on average the likelihood ratio will be

$$\langle -\log \Lambda \rangle = -\int_0^{\infty} \mathrm{d}t\, \Gamma\, e^{-\Gamma t}\, (\log \Gamma t - \Gamma t + 1) = \gamma_{\mathcal{E}}, \tag{6.43}$$

where the $\gamma_{\mathcal{E}} = 0.577216...$ is the Euler gamma, which does not vary with the rate. There-

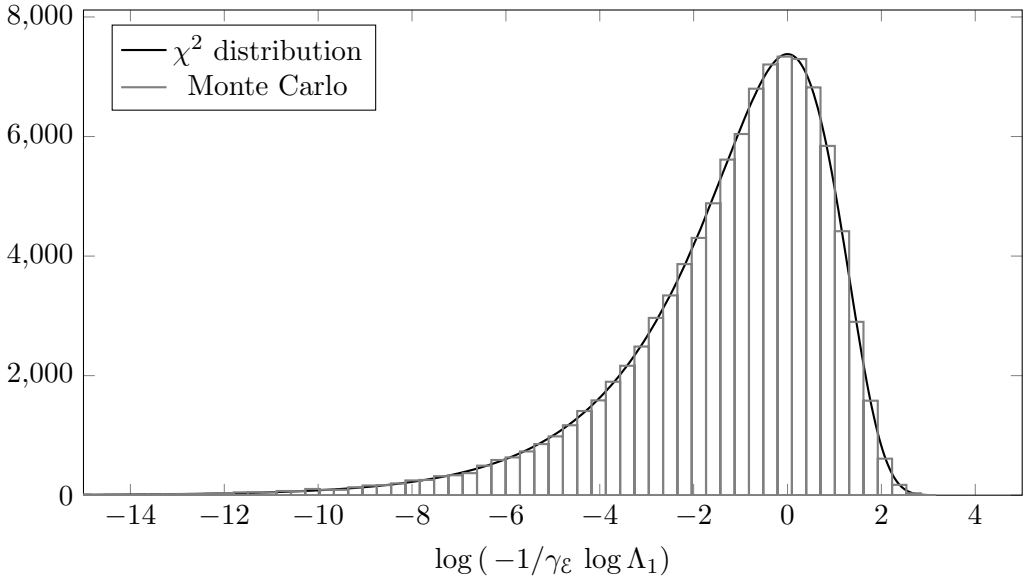

Figure 6.4: The log-likelihoods of individual time intervals between consecutive events in a random sample, scaled by the factor $-1/\gamma_\mathcal{E}$, are distributed following the χ^2 distribution. For ease of visualization and comparison, the logarithm of the log-likelihoods is plotted.

fore, a statistic

$$\chi^2 = -\frac{1}{\gamma_\mathcal{E}} \log \Lambda \tag{6.44}$$

can be used to test the goodness of fit. That is, the likelihoods computed for each time interval between events follow a χ^2 distribution, as shown in 6.4.

6.4 Mock analysis study

The analysis of the mock data is carried out using the formalism described in this section. The fit parameters $\boldsymbol{\theta}$ are estimated by maximizing the unbinned log-likelihood, computing the likelihoods of individual events with respect to a test generating rate $\Gamma(\boldsymbol{\theta}, t)$. This likelihood statistic is shown to have coverage given by values in table 6.3, so it is possible to set the error definition in the maximizer so that $\Delta \log \mathcal{L} = -0.5841$ to compute the standard confidence interval parameters errors.

In addition, the goodness of fit is computed on the data set using the χ^2 statistic computed from the likelihoods with equation 6.44. Since the data set does not need to be re-binned in order to compute the goodness of fit, the χ^2 statistic can be computed directly right after the maximum likelihood is found. The goodness of fit statistic only requires that

the expected number of events in each variable sized bin of width Δt_i is calculated using equation 6.20. Thus, this quantity can be computed for the same intervals in time used in the likelihood maximization, resulting in a goodness of fit valid for the data set used in the fit.

After cuts on the PMT energy deposition, as in equation 6.1, each Monte Carlo run consists of roughly $2.1 \cdot 10^5$ events per cell. Figure 6.5 shows the signal from a single run, which is modulated in time at a frequency of $\simeq 9.9$ Hz and decreases exponentially with time, leaving few events per bin at late times.

The ROOT analysis framework is equipped with minimization routines derived from MINUIT which were used to estimate the fit parameters in the mock analysis. Table 6.4 summarizes the fit parameters estimated from the analysis of each individual run and subsequently recombined. The observed shift in frequency, as calculated from the fit parameter ω in the two different cells, was extracted to be

$$\Delta\omega = \omega_{\uparrow\uparrow} - \omega_{\uparrow\downarrow} = (-1.52 \pm 0.99) \times 10^{-6}\ \mathrm{rad} \cdot \mathrm{s}^{-1}\,. \tag{6.45}$$

The extracted EDM signal is then calculated from the electric field magnitude $E = 74\,\mathrm{kV} \cdot \mathrm{cm}^{-1}$ given by

$$d_n = -\frac{\hbar}{2}\,\frac{\omega^{\uparrow\uparrow} - \omega^{\uparrow\downarrow}}{2\,E} \simeq (3.4 \pm 2.2) \times 10^{-27}\ \mathrm{e} \cdot \mathrm{cm}\,. \tag{6.46}$$

This agrees with the input value of the EDM parameter, which was set to $d_n = 3.3 \times 10^{-27}\,\mathrm{e} \cdot \mathrm{cm}$.

If the initial phase ϕ is known to be repeatable to a level of a 1/1000 of a radian, then the parameter ϕ can be removed from the fit parameters and the error on the frequency improves by a factor of $\sqrt{2}$. The initial phase of the scintillation signal represents the difference in accumulated precession phase between the neutron and ^{3}He spins at the end of the $\pi/2$ pulse.

6.4.1 Goodness of fit

The goodness of fit test described in section 6.3 was applied to the fit results of the mock-data analysis. The χ^2 statistic of equation 6.44 has been used to find the probability that the analyzed data set actually has, as parent distribution, the distribution offered by the

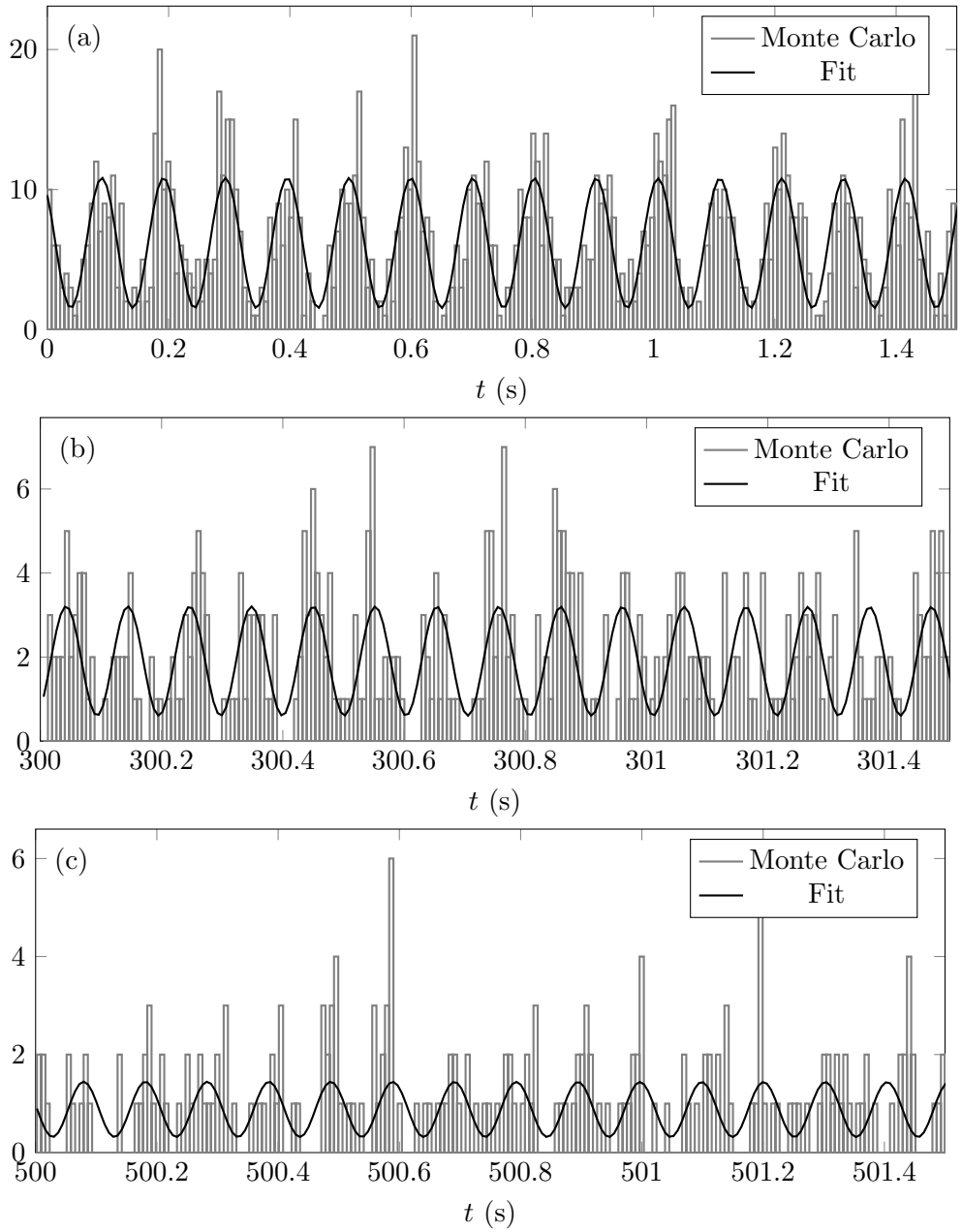

Figure 6.5: Monte Carlo events for a single mock-data run ($\sim 2 \cdot 10^5$ events) plotted over time in bins of fixed width (7 ms $\simeq 1/14\ T$) together with the expected events from the model rate with parameters which best fit the events in the run. The three plots show the event rate at the start of the run (a) and later times (b,c).

	cell 1		cell 2	
	par	err	par	err
N_0	$2.264 \cdot 10^5$	$5.3 \cdot 10^0$	$2.264 \cdot 10^5$	$5.3 \cdot 10^0$
Γ_β	$9.408 \cdot 10^{-4}$	$4.2 \cdot 10^{-7}$	$9.404 \cdot 10^{-4}$	$4.2 \cdot 10^{-7}$
Γ_3	$2.976 \cdot 10^{-3}$	$5.0 \cdot 10^{-7}$	$2.976 \cdot 10^{-3}$	$5.0 \cdot 10^{-7}$
ω	61.62685202	$7.0 \cdot 10^{-7}$	61.62685354	$7.0 \cdot 10^{-7}$
ϕ	-2.618	$1.7 \cdot 10^{-4}$	-2.618	$1.7 \cdot 10^{-4}$
$1/T_2$	$3.150 \cdot 10^{-4}$	$5.8 \cdot 10^{-7}$	$3.152 \cdot 10^{-4}$	$5.8 \cdot 10^{-7}$
Γ_B	$1.000 \cdot 10^{-2}$	$1.5 \cdot 10^{-5}$	$1.000 \cdot 10^{-2}$	$1.5 \cdot 10^{-5}$

Table 6.4: Fit parameters estimated from the 1250 runs which comprise the mock-data set, for each cell. The electric field configuration is different between cells, with cell 1 having the E field aligned to the magnetic field B_0 and cell 2 anti-aligned, resulting in a difference in precession frequency $\Delta\omega \simeq -1.52(99) \cdot 10^{-6}\,\mathrm{rad} \cdot \mathrm{s}^{-1}$ between the cells.

model rate with the best fit parameters. This can be found by computing the cumulative distribution function of the χ^2 distribution with a number of degrees of freedom given by n.d.f. $= N - n_\theta$, the difference between the number of events in the run and the number of free parameters n_θ. Figure 6.6 shows the probabilities obtained for each individual run and for each cell. Because of the large number of degrees of freedom, these quantities all represent reduced χ^2 not far away from unity. The distribution of probabilities should be uniform if the χ^2 is statistically distributed. The results from fitting the mock data show that the probability distribution is skewed towards the lower probability. This can signify that the fit function, if properly minimized, does not capture all of the characteristics of the generating function.

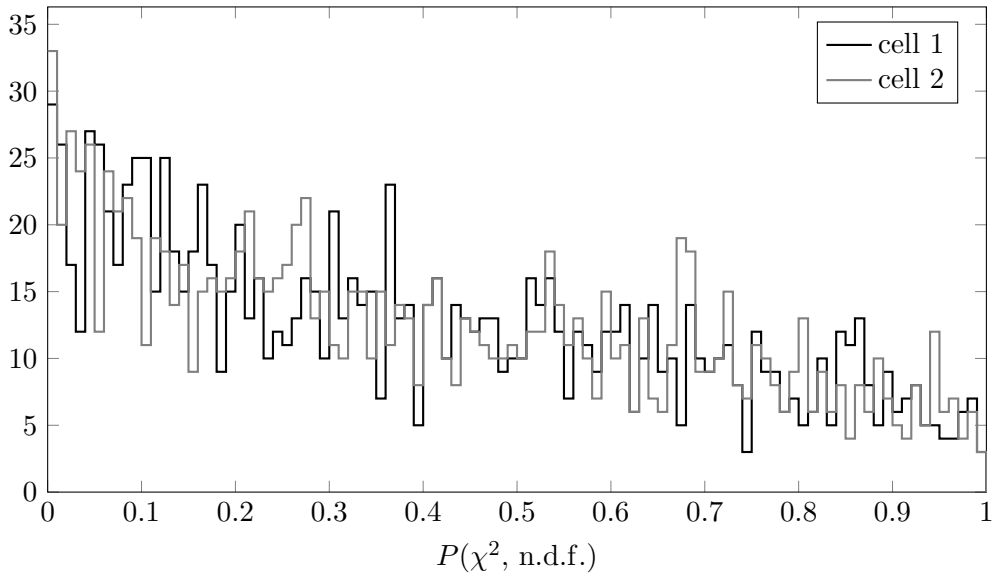

Figure 6.6: The distribution of probabilities obtained from the χ^2 statistic for each individual run in the mock-data set. The probabilities are computed from the cumulative distribution function of the χ^2 distribution. The expected shape of the curve is a uniform distribution.

Chapter 7

Summary

The proposed neutron EDM measurement is set out to provide an important test of the fundamental symmetries of the Universe. At the planned sensitivity, the experiment should offer evidence of new sources of *CP* violation and give insight to the problem of baryon number asymmetry and the concept of baryogenesis.

Some of the challenges of the new experiment have been introduced and described in this manuscript. They include the generation of a large electric field ($E \simeq 74\,\mathrm{kV \cdot cm^{-1}}$) in a liquid Helium bath at superfluid temperatures ($T \simeq 0.5\,\mathrm{K}$) and the construction of coils to provide a magnetic field that is uniform over the size of the measurement cells (40 cm).

For the measurement to achive the planned sensitivity, systematic effects arising from the *Geometric Phase* need to be well understood. The study of the systematic effect needs to be performed before the construction of the experiment, to make sure that the experimental configuration is chosen appropiately to mitigate the effect, as well as when the experiment is built and the magnetic field profiles can be measured, to further lower the error of the systematic effect. In order to study the systematic effects, Monte Carlo simulations have been advantageous, as they allow the focus to start on the simplest models of the interaction of spin with the magnetic and motional fields, and introduce and study more interesting scenarios as desired. Part of the work in this manuscript was aimed at developing software and production systems that would allow for the generation and analysis of statistically significant samples of Monte Carlo data to study the problem. This entailed the use of parallelization of the simulation program to be run on many computer cores, augmented by the availability of commercial *cloud* computing resources.

Bibliography

[1] E. M. Purcell and N. F. Ramsey. On the possibility of electric dipole moments for elementary particles and nuclei. *Phys. Rev.*, 78:807–807, Jun 1950.

[2] J. H. Smith, E. M. Purcell, and N. F. Ramsey. Experimental limit to the electric dipole moment of the neutron. *Phys. Rev.*, 108:120–122, Oct 1957.

[3] G. Harris, J. Orear, and S. Taylor. Lifetimes of the τ^+ and k_L^+s-mesons. *Phys. Rev.*, 100:932–932, Nov 1955.

[4] V. Fitch and R. Motley. Mean life of K^+ mesons. *Phys. Rev.*, 101:496–498, Jan 1956.

[5] T. D. Lee and C. N. Yang. Question of parity conservation in weak interactions. *Phys. Rev.*, 104:254–258, Oct 1956.

[6] C. S. Wu, E. Ambler, R. W. Hayward, D. D. Hoppes, and R. P. Hudson. Experimental test of parity conservation in beta decay. *Phys. Rev.*, 105:1413–1415, Feb 1957.

[7] L. Landau. On the conservation laws for weak interactions. *Nuclear Physics*, 3(1):127 – 131, 1957.

[8] J. H. Christenson, J. W. Cronin, V. L. Fitch, and R. Turlay. Evidence for the 2π decay of the k_2^0 meson. *Phys. Rev. Lett.*, 13:138–140, Jul 1964.

[9] V.L. Fitch. The discovery of charge-conjugation parity asymmetry. *Review of Modern Physics*, 53:367, 1981.

[10] J. P. Lees, V. Poireau, V. Tisserand, J. Garra Tico, E. Grauges, A. Palano, G. Eigen, B. Stugu, D. N. Brown, L. T. Kerth, Yu. G. Kolomensky, G. Lynch, H. Koch, T. Schroeder, D. J. Asgeirsson, C. Hearty, T. S. Mattison, J. A. McKenna, R. Y. So, A. Khan, V. E. Blinov, A. R. Buzykaev, V. P. Druzhinin, V. B. Golubev, E. A.

Kravchenko, A. P. Onuchin, S. I. Serednyakov, Yu. I. Skovpen, E. P. Solodov, K. Yu. Todyshev, A. N. Yushkov, M. Bondioli, D. Kirkby, A. J. Lankford, M. Mandelkern, H. Atmacan, J. W. Gary, F. Liu, O. Long, G. M. Vitug, C. Campagnari, T. M. Hong, D. Kovalskyi, J. D. Richman, C. A. West, A. M. Eisner, J. Kroseberg, W. S. Lockman, A. J. Martinez, B. A. Schumm, A. Seiden, D. S. Chao, C. H. Cheng, B. Echenard, K. T. Flood, D. G. Hitlin, P. Ongmongkolkul, F. C. Porter, A. Y. Rakitin, R. Andreassen, Z. Huard, B. T. Meadows, M. D. Sokoloff, L. Sun, P. C. Bloom, W. T. Ford, A. Gaz, U. Nauenberg, J. G. Smith, S. R. Wagner, R. Ayad, W. H. Toki, B. Spaan, K. R. Schubert, R. Schwierz, D. Bernard, M. Verderi, P. J. Clark, S. Playfer, D. Bettoni, C. Bozzi, R. Calabrese, G. Cibinetto, E. Fioravanti, I. Garzia, E. Luppi, M. Munerato, L. Piemontese, V. Santoro, R. Baldini-Ferroli, A. Calcaterra, R. de Sangro, G. Finocchiaro, P. Patteri, I. M. Peruzzi, M. Piccolo, M. Rama, A. Zallo, R. Contri, E. Guido, M. Lo Vetere, M. R. Monge, S. Passaggio, C. Patrignani, E. Robutti, B. Bhuyan, V. Prasad, C. L. Lee, M. Morii, A. J. Edwards, A. Adametz, U. Uwer, H. M. Lacker, T. Lueck, P. D. Dauncey, U. Mallik, C. Chen, J. Cochran, W. T. Meyer, S. Prell, A. E. Rubin, A. V. Gritsan, Z. J. Guo, N. Arnaud, M. Davier, D. Derkach, G. Grosdidier, F. Le Diberder, A. M. Lutz, B. Malaescu, P. Roudeau, M. H. Schune, A. Stocchi, G. Wormser, D. J. Lange, D. M. Wright, C. A. Chavez, J. P. Coleman, J. R. Fry, E. Gabathuler, D. E. Hutchcroft, D. J. Payne, C. Touramanis, A. J. Bevan, F. Di Lodovico, R. Sacco, M. Sigamani, G. Cowan, D. N. Brown, C. L. Davis, A. G. Denig, M. Fritsch, W. Gradl, K. Griessinger, A. Hafner, E. Prencipe, R. J. Barlow, G. Jackson, G. D. Lafferty, E. Behn, R. Cenci, B. Hamilton, A. Jawahery, D. A. Roberts, C. Dallapiccola, R. Cowan, D. Dujmic, G. Sciolla, R. Cheaib, D. Lindemann, P. M. Patel, S. H. Robertson, P. Biassoni, N. Neri, F. Palombo, S. Stracka, L. Cremaldi, R. Godang, R. Kroeger, P. Sonnek, D. J. Summers, X. Nguyen, M. Simard, P. Taras, G. De Nardo, D. Monorchio, G. Onorato, C. Sciacca, M. Martinelli, G. Raven, C. P. Jessop, J. M. LoSecco, W. F. Wang, K. Honscheid, R. Kass, J. Brau, R. Frey, N. B. Sinev, D. Strom, E. Torrence, E. Feltresi, N. Gagliardi, M. Margoni, M. Morandin, A. Pompili, M. Posocco, M. Rotondo, G. Simi, F. Simonetto, R. Stroili, S. Akar, E. Ben-Haim, M. Bomben, G. R. Bonneaud, H. Briand, G. Calderini, J. Chauveau, O. Hamon, Ph. Leruste, G. Marchiori, J. Ocariz, S. Sitt, M. Biasini, E. Manoni, S. Pacetti, A. Rossi, C. Angelini, G. Batignani, S. Bettarini, M. Carpinelli, G. Casarosa,

A. Cervelli, F. Forti, M. A. Giorgi, A. Lusiani, B. Oberhof, E. Paoloni, A. Perez, G. Rizzo, J. J. Walsh, D. Lopes Pegna, J. Olsen, A. J. S. Smith, A. V. Telnov, F. Anulli, R. Faccini, F. Ferrarotto, F. Ferroni, M. Gaspero, L. Li Gioi, M. A. Mazzoni, G. Piredda, C. Bünger, O. Grünberg, T. Hartmann, T. Leddig, H. Schröder, C. Voss, R. Waldi, T. Adye, E. O. Olaiya, F. F. Wilson, S. Emery, G. Hamel de Monchenault, G. Vasseur, Ch. Yèche, D. Aston, D. J. Bard, R. Bartoldus, J. F. Benitez, C. Cartaro, M. R. Convery, J. Dorfan, G. P. Dubois-Felsmann, W. Dunwoodie, M. Ebert, R. C. Field, M. Franco Sevilla, B. G. Fulsom, A. M. Gabareen, M. T. Graham, P. Grenier, C. Hast, W. R. Innes, M. H. Kelsey, P. Kim, M. L. Kocian, D. W. G. S. Leith, P. Lewis, B. Lindquist, S. Luitz, V. Luth, H. L. Lynch, D. B. MacFarlane, D. R. Muller, H. Neal, S. Nelson, M. Perl, T. Pulliam, B. N. Ratcliff, A. Roodman, A. A. Salnikov, R. H. Schindler, A. Snyder, D. Su, M. K. Sullivan, J. Va'vra, A. P. Wagner, W. J. Wisniewski, M. Wittgen, D. H. Wright, H. W. Wulsin, C. C. Young, V. Ziegler, W. Park, M. V. Purohit, R. M. White, J. R. Wilson, A. Randle-Conde, S. J. Sekula, M. Bellis, P. R. Burchat, T. S. Miyashita, E. M. T. Puccio, M. S. Alam, J. A. Ernst, R. Gorodeisky, N. Guttman, D. R. Peimer, A. Soffer, P. Lund, S. M. Spanier, J. L. Ritchie, A. M. Ruland, R. F. Schwitters, B. C. Wray, J. M. Izen, X. C. Lou, F. Bianchi, D. Gamba, S. Zambito, L. Lanceri, L. Vitale, J. Bernabeu, F. Martinez-Vidal, A. Oyanguren, P. Villanueva-Perez, H. Ahmed, J. Albert, Sw. Banerjee, F. U. Bernlochner, H. H. F. Choi, G. J. King, R. Kowalewski, M. J. Lewczuk, I. M. Nugent, J. M. Roney, R. J. Sobie, N. Tasneem, T. J. Gershon, P. F. Harrison, T. E. Latham, H. R. Band, S. Dasu, Y. Pan, R. Prepost, and S. L. Wu. Observation of time-reversal violation in the b0 meson system. *Phys. Rev. Lett.*, 109:211801, Nov 2012.

[11] Makoto Kobayashi and Toshihide Maskawa. CP-violation in the renormalizable theory of weak interaction. *Progress of Theoretical Physics*, 49(2):652–657, 1973.

[12] Mark Trodden. Electroweak baryogenesis. *Rev. Mod. Phys.*, 71:1463–1500, Oct 1999.

[13] G. Steigman. Observational tests of antimatter cosmology. *Annual review of astronomy and astrophysics*, 14, 1976.

[14] A. D. Sakharov. Violation of CP in variance, C asymmetry, and baryon asymmetry of the universe. *JETP Letters*, 5(5):392, 1967.

[15] J. et al. Beringer. Review of particle physics (PDG). *Phys. Rev. D*, 86:010001, Jul 2012.

[16] M.E. Shaposhnikov. Possible appearance of the baryon asymmetry of the universe in an electroweak theory. *Pis'ma Zh. Eksp. Teor. Fiz.*, 44:364, 1986.

[17] Glennys R. Farrar and M. E. Shaposhnikov. Baryon asymmetry of the universe in the minimal standard model. *Phys. Rev. Lett.*, 70:2833–2836, May 1993.

[18] David E Morrissey and Michael J Ramsey-Musolf. Electroweak baryogenesis. *New Journal of Physics*, 14(12):125003, 2012.

[19] Vincenzo Cirigliano, Stefano Profumo, and Michael J. Ramsey-Musolf. Baryogenesis, electric dipole moments and dark matter in the MSSM. *Journal of High Energy Physics*, 2006(07):002, 2006.

[20] Maxim Pospelov and Adam Ritz. Electric dipole moments as probes of new physics. *Annals of Physics*, 318(1):119 – 169, 2005. Special Issue.

[21] Yingchuan Li, Stefano Profumo, and Michael Ramsey-Musolf. A comprehensive analysis of electric dipole moment constraints on CP-violating phases in the MSSM. *Journal of High Energy Physics*, 2010(8):1–25, 2010.

[22] P. G. H. Sandars and E. Lipworth. Electric dipole moment of the cesium atom. A new upper limit to the electric dipole moment of the free electron. *Phys. Rev. Lett.*, 13(24):718–720, Dec 1964.

[23] Eugene D. Commins, Stephen B. Ross, David DeMille, and B. C. Regan. Improved experimental limit on the electric dipole moment of the electron. *Phys. Rev. A*, 50:2960–2977, Oct 1994.

[24] B. C. Regan, Eugene D. Commins, Christian J. Schmidt, and David DeMille. New limit on the electron electric dipole moment. *Phys. Rev. Lett.*, 88:071805, Feb 2002.

[25] J. J. Hudson, B. E. Sauer, M. R. Tarbutt, and E. A. Hinds. Measurement of the electron electric dipole moment using YbF molecules. *Phys. Rev. Lett.*, 89:023003, Jun 2002.

[26] J.J. Hudson, D.M Kara, I.J. Smallman, B.E. Sauer, M.R. Tarbutt, and E.A. Hinds. Improved measurement of the shape of the electron. *Nature*, 473:493–496, 2011.

[27] L. I. Schiff. Measurability of nuclear electric dipole moments. *Phys. Rev.*, 132:2194–2200, Dec 1963.

[28] W. C. Griffith, M. D. Swallows, T. H. Loftus, M. V. Romalis, B. R. Heckel, and E. N. Fortson. Improved limit on the permanent electric dipole moment of ^{199}Hg. *Phys. Rev. Lett.*, 102:101601, Mar 2009.

[29] Y.B. Zel'dovich. *Soviet Phyis. JETP*, 9:1389, 1959.

[30] R. Golub, D. Richardson, and S. K. Lamoreaux. *Ultra-Cold Neutrons*. Taylor & Francis, 1991.

[31] J. M. Pendlebury, W. Heil, Yu. Sobolev, P. G. Harris, J. D. Richardson, R. J. Baskin, D. D. Doyle, P. Geltenbort, K. Green, M. G. D. van der Grinten, P. S. Iaydjiev, S. N. Ivanov, D. J. R. May, and K. F. Smith. Geometric-phase-induced false electric dipole moment signals for particles in traps. *Physical Review A (Atomic, Molecular, and Optical Physics)*, 70(3):032102, 2004.

[32] P. G. Harris, C. A. Baker, K. Green, P. Iaydjiev, S. Ivanov, D. J. R. May, J. M. Pendlebury, D. Shiers, K. F. Smith, M. van der Grinten, and P. Geltenbort. New experimental limit on the electric dipole moment of the neutron. *Phys. Rev. Lett.*, 82(5):904–907, Feb 1999.

[33] C. A. Baker, D. D. Doyle, P. Geltenbort, K. Green, M. G. D. van der Grinten, P. G. Harris, P. Iaydjiev, S. N. Ivanov, D. J. R. May, J. M. Pendlebury, J. D. Richardson, D. Shiers, and K. F. Smith. Improved experimental limit on the electric dipole moment of the neutron. *Phys. Rev. Lett.*, 97:131801, Sep 2006.

[34] R. Golub and Steve K. Lamoreaux. Neutron electric-dipole moment, ultracold neutrons and polarized ^{3}He. *Physics Reports*, 237(1):1 – 62, 1994.

[35] EDM Collaboration. A new search for the neutron electric dipole moment (funding pre-proposal submitted to the department of energy). LA-UR 02-2331, March 2002.

[36] E. Fermi and W.H. Zinn. *Phys. Rev.*, 70:103, 1946.

[37] B. Plaster. Measurement of the neutron β-asymmetry parameter A_0 with ultracold neutrons.

[38] A. Steyerl. A neutron turbine as an efficient source of ultracold neutrons. *Nuclear Instruments and Methods*, 125(3):461 – 469, 1975.

[39] R. Golub and J.M. Pendlebury. The interaction of ultra-cold neutrons (UCN) with liquid helium and a superthermal UCN source. *Physics Letters A*, 62(5):337 – 339, 1977.

[40] R. Golub and J. M. Pendlebury. The electric dipole moment of the neutron. *Contemporary Physics*, 13(6):519–558, 1972.

[41] V. A. Dzuba, V. V. Flambaum, and J. S. M. Ginges. Atomic electric dipole moments of He and Yb induced by nuclear schiff moments. *Phys. Rev. A*, 76:034501, Sep 2007.

[42] E. Muskat, D. Dubbers, and O. Schärpf. Dressed neutrons. *Phys. Rev. Lett.*, 58:2047–2050, May 1987.

[43] Norman F. Ramsey. A molecular beam resonance method with separated oscillating fields. *Phys. Rev.*, 78:695–699, Jun 1950.

[44] Y Chibane, S K Lamoreaux, J M Pendlebury, and K F Smith. Minimum variance of frequency estimations for a sinusoidal signal with low noise. *Measurement Science and Technology*, 6(12):1671, 1995.

[45] David J. Griffiths. *Introduction to Electrodynamics (3rd Edition)*. Benjamin Cummings, 1998.

[46] J. D. Hunter. Matplotlib: A 2d graphics environment. *Computing In Science & Engineering*, 9(3):90–95, 2007.

[47] John D. Jackson. *Classical Electrodynamics Third Edition*. Wiley, third edition, August 1998.

[48] S. Malkowski, R. Adhikari, B. Hona, C. Mattie, D. Woods, H. Yan, and B. Plaster. Technique for high axial shielding factor performance of large-scale, thin, open-ended, cylindrical metglas magnetic shields. *Review of Scientific Instruments*, 82(7):075104, 2011.

[49] Metglas. 2705m magnetic alloy specifications. www.metglas.com.

[50] L. Tracy, R. Schmid, J. Eisenstein, and B.W. Filippone. Measurement of Metglas resistivity in Jim Eisenstein laboratory (private communication), 2006.

[51] P Mansfield and B Chapman. Active magnetic screening of coils for static and time-dependent magnetic field generation in NMR imaging. *Journal of Physics E: Scientific Instruments*, 19(7):540, 1986.

[52] C.P. Bidinosti, I.S. Kravchuk, and M.E. Hayden. Active shielding of cylindrical saddle-shaped coils: Application to wire-wound RF coils for very low field NMR and MRI. *Journal of Magnetic Resonance*, 177(1):31 – 43, 2005.

[53] R Turner and R M Bowley. Passive screening of switched magnetic field gradients. *Journal of Physics E: Scientific Instruments*, 19(10):876, 1986.

[54] B Chapman and P Mansfield. Double active magnetic screening of coils in NMR. *Journal of Physics D: Applied Physics*, 19(7):L129, 1986.

[55] M. at al. Galassi. *GNU Scientific Library Reference Manual (3rd Edition)*. Network Theory, 2009.

[56] A. Perez Galvan, B. Plaster, J. Boissevain, R. Carr, B.W. Filippone, M.P. Mendenhall, R. Schmid, R. Alarcon, and S. Balascuta. High uniformity magnetic coil for search of neutron electric dipole moment. *Nuclear Instruments and Methods in Physics Research Section A: Accelerators, Spectrometers, Detectors and Associated Equipment*, 660(1):147 – 153, 2011.

[57] J. C. Long, P. D. Barnes, J. G. Boissevain, D. J. Clark, M. D. Cooper, J. J. Gomez, S. K. Lamoreaux, R. E. Mischke, and S. I. Penttila. High voltage test apparatus for a neutron edm experiment and lower limit on the dielectric strength of liquid helium at large volumes. *ArXiv Physics e-prints*, March 2006.

[58] R. J. Donnelly and C.F. Barenghi. The observed properties of liquid helium at the saturated vapor pressure `http://pages.uoregon.edu/rjd/vapor1.htm`. 2004.

[59] D. C. Meeker. Finite element method magnetics. www.femm.info. Version 4.0.1.

[60] V A Lisovskiy, S D Yakovin, and V D Yegorenkov. Low-pressure gas breakdown in uniform dc electric field. *Journal of Physics D: Applied Physics*, 33(21):2722, 2000.

[61] J Dutton and D B Rees. Ionization processes in helium at pressures near to atmospheric. *British Journal of Applied Physics*, 18(3):309, 1967.

[62] R.J. Meats. Pressurised-helium breakdown at very low temperatures. *Proceedings of the Institution of Electrical Engineers*, 119(6):760–765, 1972.

[63] J. Gerhold. Properties of cryogenic insulants. *Cryogenics*, 38(11):1063 – 1081, 1998.

[64] Z. Krasucki. Breakdown of liquid dielectrics. *Proceedings of the Royal Society of London. Series A. Mathematical and Physical Sciences*, 294(1438):393–404, 1966.

[65] W.F. Schmidt, E. Illenberger, A.G. Khrapak, Y. Sakai, and Katsumi Yoshino. Electronic conduction and breakdown in liquid helium and liquid neon. *Dielectrics and Electrical Insulation, IEEE Transactions on*, 10(6):1012–1021, 2003.

[66] J Dutton, F Llewellyn Jones, and D B Rees. Ionization in helium at high pressures. *Proceedings of the Physical Society*, 85(5):909, 1965.

[67] T. M. Ito. Private communication. 2011.

[68] T. M. Ito and nEDM collaboration. Medium scale high voltage test progress (internal communication).

[69] C.P. Slichter. *Principles of Magnetic Resonance*. Springer-Verlag, 1963.

[70] Norman F. Ramsey. Resonance transitions induced by perturbations at two or more different frequencies. *Phys. Rev.*, 100:1191–1194, Nov 1955.

[71] A. Steyerl. Effect of surface roughness on the total reflexion and transmission of slow neutrons. *Zeitschrift fr Physik*, 254(2):169–188, 1972.

[72] A. Steyerl, S. S. Malik, A. M. Desai, and C. Kaufman. Surface roughness effect on ultracold neutron interaction with a wall and implications for computer simulations. *Phys. Rev. C*, 81:055505, May 2010.

[73] E. Krotscheck, M. Saarela, K. Schörkhuber, and R. Zillich. Concentration dependence of the effective mass of ^{3}He atoms in ^{3}He-^{4}He mixtures. *Phys. Rev. Lett.*, 80(21):4709–4712, May 1998.

[74] S. K. Lamoreaux, G. Archibald, P. D. Barnes, W. T. Buttler, D. J. Clark, M. D. Cooper, M. Espy, G. L. Greene, R. Golub, M. E. Hayden, C. Lei, L. J. Marek, J.-C. Peng, and S. Penttila. Measurement of the ^{3}He mass diffusion coefficient in superfluid ^{4}He over the 0.45-0.95 K temperature range. *EPL (Europhysics Letters)*, 58(5):718–724, 2002.

[75] A. L. Barabanov, R. Golub, and S. K. Lamoreaux. Electric dipole moment searches: Effect of linear electric field frequency shifts induced in confined gases. *Physical Review A (Atomic, Molecular, and Optical Physics)*, 74(5):052115, 2006.

[76] G. D. Cates, S. R. Schaefer, and W. Happer. Relaxation of spins due to field inhomogeneities in gaseous samples at low magnetic fields and low pressures. *Phys. Rev. A*, 37(8):2877–2885, Apr 1988.

[77] *Numerical Recipes: The Art of Scientific Computing, Third Edition.* Cambridge University Press, 2007.

[78] Dries Buytaert. Drupal. Content Management System.

[79] Mysql. Relational Database.

[80] Rene Brun and Fons Rademakers. ROOT - an object oriented data analysis framework. *Nucl. Inst. & Meth. in Physics*, A389, Sep. 1996.

[81] J. Varia and S. Mathew. Overview of Amazon Web Services. *AWS whitepapers*, 2013.

[82] Douglas D. McGregor. Transverse relaxation of spin-polarized ^{3}He gas due to a magnetic field gradient. *Phys. Rev. A*, 41(5):2631–2635, Mar 1990.

[83] M G Richards, B P Cowan, M F Secca, and K Machin. The ^{3}He nuclear Zeeman maser. *Journal of Physics B: Atomic, Molecular and Optical Physics*, 21(4):665, 1988.

[84] Riccardo Schmid, B. Plaster, and B. W. Filippone. Motional spin relaxation in large electric fields. *Physical Review A (Atomic, Molecular, and Optical Physics)*, 78(2):023401, 2008.

[85] A. Papoulis. *Probability, Random Variables, and Stochastic Processes*. McGrawHill, 165.

[86] M. V. Berry. Quantal phase factors accompanying adiabatic changes. *Proceedings of the Royal Society of London. A. Mathematical and Physical Sciences*, 392(1802):45–57, 1984.

[87] Eugene D. Commins. Berry's geometric phase and motional fields. *American Journal of Physics*, 59(12):1077–1080, 1991.

[88] J.M. Pendlebury and D.J. Richardson. Effects of gravity on the storage of ultracold neutrons. *Nuclear Instruments and Methods in Physics Research Section A: Accelerators, Spectrometers, Detectors and Associated Equipment*, 337(23):504 – 511, 1994.

[89] S. K. Lamoreaux. Additional motional-magnetic-field considerations for electric-dipole-moment experiments. *Phys. Rev. A*, 53(6):R3705–R3708, Jun 1996.

[90] S. K. Lamoreaux and R. Golub. Detailed discussion of a linear electric field frequency shift induced in confined gases by a magnetic field gradient: Implications for neutron electric-dipole-moment experiments. *Phys. Rev. A*, 71(3):032104, Mar 2005.

[91] Steven M. Clayton. Spin relaxation and linear-in-electric-field frequency shift in an arbitrary, time-independent magnetic field. *Journal of Magnetic Resonance*, 211(1):89 – 95, 2011.

[92] C.M. Swank, A.K. Petukhov, and R. Golub. Correlation functions for restricted brownian motion from the ballistic through to the diffusive regimes. *Physics Letters A*, 376(34):2319 – 2324, 2012.

[93] R. Golub, C.M. Swank, and S. K. Lamoreaux. Electric dipole moment searches: Effect of linear electric field frequency shifts induced in confined gases, II. *ArXiv (nucl-ex)*, 0810.5378, 2009.

[94] Inc. Wolfram Research. Mathematica, 2010.

[95] R. Schmid and B.W. Filippone. Dressing field uniformity. *nEDM internal note*, 2010.

[96] B. Plaster. Mock data challenge GEANT4 dataset (private communication).

[97] Glen Cowan. *Statistical Data Analysis*. Oxford Science Publications, 1998.

[98] J. Neyman. Outline of a theory of statistical estimation based on the classical theory of probability. *Philosophical Transactions of the Royal Society of London. Series A, Mathematical and Physical Sciences*, 236(767):333–380, 1937.

[99] Louis Lyons. Discovery or fluke: Statistics in particle physics. *Physics Today*, page 45, 2012.